Self-Organized Instabilities of Liquid Crystal Droplets and Ultrathin Films

a

Thesis Submitted

in Partial Fulfillment of the Requirements

for the Degree of

DOCTOR OF PHILOSOPHY

by

BOLLEDDU RAVI

Under the Supervision of

Dr. DIPANKAR BANDYOPADHYAY

Department of Chemical Engineering
Indian Institute of Technology Guwahati

February 2018

Certificate

This is certified that the work contained in this thesis entitled "**Self-Organized Instabilities of Liquid Crystal Droplets and Ultrathin Films**", by Mr. Bolleddu Ravi, has been carried out under my supervision and that this work has not been submitted elsewhere for a degree.

Signature:

Thesis Supervisor
Dr. Dipankar Bandyopadhyay
Associate Professor,
Department of Chemical Engineering,
Indian Institute of Technology Guwahati,
Guwahati, PIN Code:781039, Assam, India.

Date:

Dedicated

to

My Lord & Saviour Jesus Christ and Supervisor...

Acknowledgments

First of all, I express my deep gratitude to my thesis supervisor **Dr. Dipankar Bandyopadhyay** for all his support, encouragement, motivation, and guidance to have been complete the thesis successfully. In this complete thesis work, without his support I may not able to finish. I really wonder about his patience in training and teaching throughout my thesis tenure. Whenever I was stuck up in the experiments, he gave me wonderful solutions to pass through the hardness. He also helped me to interact with the experts to learn experimental techniques. Personally, he was very generous towards me in about everything. I thank, my God and saviour Jesus Christ, who gave me this opportunity to work with him.

I wish to thank my doctoral committee members, **Dr. Baskaran Anand**, Department of Biosciences and Bioengineering, **Prof. Kaustubha Mohanty** and **Dr. Tapas Kumar Mandal**, Department of Chemical Engineering, for their valuable suggestions during my thesis work.

I wish to thank **Dr. Rabibrata Mukherjee** who gave me the wonderful opportunity to work in his lab and learn experiments. I also wish to thank **Dr. Partho Sarathi Gooh Pattader** for his suggestions during the experiments.

I wish to thank all my colleagues **Dr. Karthick Mondal**, **Dr. Ananth Praveen Kumar**, **Dr. Nandini Bhandaru**, **Abhijna Das**, **Snigdha Chakraborty**, **Amit Kumar Singh**, **Mitradip Bhattacharjee** for their support during the experiments, **Shirsendu Mitra**, and **Abir Ghosh** for their support during the theoretical modeling.

I wish to thank all my lab-mates for their help in experiments especially **Seim Timung**, **Siddharth Thakur**,**Saptak Rarotra**, **Sunny Kumar**, and **Nilanjan Mandal**.

I wish to acknowledge Analytical Lab, Department of Chemical Engineering, who gave me opportunity to use Imaging Ellipsometer, Rheometer, and X-Ray diffractiometer. I also acknowledge Centre for Nanotechnology and CIF, IIT Guwahati for the support on AFM, Raman, UV-VIS, and IR measurements.

I wish to thank all staff and faculty members of the Department of Chemical Engineering and Centre for Nanotechnology for all their support during my thesis tenure.

I wish to acknowledge the financial grants by DST, SERB grant no: SR/FTP/ETA-091/2009, DST-FIST grant no: SR/FST/ETII-028/2010, and MeitY grant no: 5(9)/2012-NANO.

I wish to thank to all my labmates for their help and company in the lab especially, **Dr. Nayan Mani Das**, **Satarupa Dutta**, **Joydip Choudhuri**, **Ankur Pandey**, **Bhaskarjyoti Sarma**, **Manash Pratim Borthakur**, **Binita Nath**, **Pritam Roy**, **Surjendu Maity**, **Tamanna Bhuyan**, **V. Prasada Sandireddy**, **Viswanath Pasumarthi**, **Sagnik Middya**, and **Debdatta Ghosh**.

It is a great pleasure give thanks to all my brothers and families who always pray for my health and well-being. First of all, I wish to acknowledge **Dr. Agile Matthew** and family, who as a channel of God, helped in my restoration. Special thanks to **Dr. Simon Peter** and family, **Dr. Rajesh** and family, **Mary Medikonda**, **Dr.**

Swaroopa Dasari and family, **Nishanth** and family, **Dr. Ramesh** and family, **Dr. Suresh**, **Senu**, **Rajashekar** and family, **Dharma** and family, **Prof. Roy Pailly** and family, **Dr. Atul** and family, **Dr. Santil kumar** and family, **Dr. Kamal** and family, **Dr. Anand** and family, **Dr. Santhi raju** and family, **Dr. Nagesh** and family, **Bhagat** anna and family, **Ujwal** and family, **Ravichandra** anna and family, **Raji**, **Pradeep**, and **Ajay** anna and family.

It is my honor to thank my parents for their love, care, and support. I also wish to thank my own brothers and relatives for their encouragement.

With a great joy I wish to thank my wife and my daughters for their love, care, fellowship and everything else.

Finally, It is my honor and privilege to thank my God and Saviour Jesus Christ for thy love, grace, fellowship, headship and everything else.

"Without shedding of blood there is no forgiveness of sins." (Hebrews 9:22)

"For God so loved the world, that He gave His only begotten Son, that whoever believes in Him shall not perish, but have eternal life." (John 3:16)

"But God demonstrates His own love toward us, in that while we were still sinners, Christ died for us." (Romans 5:8)

"Jesus answered, I am the way and the truth and the life. No one comes to the Father except through me." (John 14:6)

Sincerely
Bolleddu Ravi

Synopsis

In the present thesis, we explore a number of simple and cost-effective pathways to develop micro and nanoscale patterns of liquid crystals (LCs) exploiting the self-organized instabilities of the LC droplets and ultrathin films. The content of the thesis is divided into five research objectives alongside an overall introduction in the beginning and important conclusions at the end. The **Chapter 1** of the thesis deals with the overall introduction. The **Chapter 2** aims to uncover the pattern directed dewetting of an ultrathin polymer film to form dense and ordered nanostructures. Following this, in the **Chapter 3**, we show the solvent vapour mediated phase transition and dewetting of LC films followed by the spontaneous healing of defects of the same with the solvent exposure removal. In the **Chapter 4**, we demonstrate the pattern directed phase transition of the LC films while in the **Chapter 5**, we show the details of the spin-dewetting of the LCs to form a large area patterns of LC micro or nanodroplets. Thereafter, in the **Chapter 6**, we show the formation of LC microlenses from the solvent vapour mediated contact line instabilities of LC droplets. In the process, we demonstrate a number of simple applications associated with the micro or nanoscale LC reflectors, locomotives, lenses, sensors, and oscillators, among others. Finally, we summarize the thesis in the **Chapter 7** with the important conclusions drawn from the research objectives and the future scopes associated with the extension of these works.

Chapter 1: Introduction

The scientific understanding of the stability and dynamics of thin liquid films have attracted attention for ages owing to their presence in various important products and processes such as the soap films, emulsions, foams, adhesives, and coatings. Further, the thin film dynamics is found to play crucial roles in the performance of the various technologically important processes such as, (a) phase change – condensation, evaporation, or boiling of fluids, (b) wettability of diverse materials, (c) recovery of petroleum products from the oil wells, (d) reflective or antireflective coatings on the lenses or solar cells or mirrors or filters, (e) corrosion resistance protective layers, (f) coatings inside the optical waveguides, and (g) modern day display units. Thin films have also been found to be ubiquitous in nature as the pre-corneal films on eyes, thin mucus layers on the organs, protective layer on the eggs, waxing on the plant leaves, and epidermal skin,

to mention a few. While a stable thin film composed of an inert material can act as protective coating, the breakup of the same can form micro to nanoscale patterns such as droplets, labyrinths, pillars, channels, or holes having exceptionally high surface to volume ratios. Of late, a number of research works have shown that these miniaturized patterns can be employed to improve the efficiency of a number of cutting-edge applications which include solar and fuel cells, super-hydrophobic surfaces, pressure sensitive adhesives, digital micro/nanofluidics, and optoelectronic devices. Thus, in the past few decades, extensive research activities have been observed in studying the various facts of the stability and dynamics of the thin films.

The thin films can be coated on the substrates employing different types of methodologies such as spin-casting, dip coating, chemical or physical vapour deposition, electrochemical deposition, monolayer deposition, pulsed laser deposition, atomic layer deposition, and molecular beam epitaxy. In general, the methodologies for film deposition is chosen based on the thickness and uniformity requirement. For example, the spin or dip-coating processes are perhaps the most widely employed low-cost techniques for deposition of organic or polymer films having micro to nanoscale thickness while the molecular beam epitaxy or atomic layer deposition has been employed for the layer by layer deposition of atoms. Importantly, most of these techniques deposit the films of the desired materials on a solid substrate before any further processing. Thus, it is not very surprising that a thin film resting on a solid substrate is perhaps among the most widely explored theoretical or experimental prototypes. In particular, the uniformity of the film thickness, surface roughness, and the stability or instability of the films of the coating materials under varied conditions is found to have long lasting impact on the performance of different products and processes.

In this direction, one of the very important scientific breakthrough in the past century has been the discovery of the self-organized instabilities of the ultrathin liquid films. An extensive exploration on this topic has uncovered that the ultrathin liquid films of thickness less than 100 nm are inherently unstable under the destabilizing influence of the long range van der Waals forces. The self-organized instabilities of the ultrathin films having thickness less than 20 nm are termed as spinodal dewetting in which the thermal or mechanical fluctuations at the film surface grow to form randomly placed holes on a homogeneous flat surface with the average spacing decided by the imbalance of the destabilizing van der Waals force to the stabilizing surface tension force. In comparison,

the films having thickness larger than 20 nm follow the heterogeneous nucleation pathway in which the lateral wettability gradient present on the surface due to the physical or chemical defects decides the locations of the hole formation. In both the processes, with the progress in time, the holes expand to achieve equilibrium contact angle before they coalesce to form Voronoi tessellation of ribbons like structures. Finally, these 'liquid ribbons' break due to Rayleigh-Plateau instability to form randomly placed droplets on the substrate. Interestingly, when these self-organized instabilities of the thin films are guided by the physical or chemical patterns decorated on the underlying substrate, they can show large area ordering of the patterns useful for fabrication or micro or nanoscale channels, formation of micro or nanolenses, droplet or digital electronic applications, hierarchical structure formation suitable for superhydrophobic surfaces, and 3D printing.

It may be noted here that the studies associated with the self-organized instabilities largely employ polymers rather than the commonly available simpler inorganic or organic liquids due to the following reasons: (i) polymer has less volatility than the commonly available liquids, which helps in studying the dynamics in absence of evaporation; (ii) the polymers are in general solid at room temperature and can easily be made to flow beyond their glass transition temperature (T_G); (iii) the viscosity of the polymers beyond their T_G is high, which helps in slowing down the kinetics of the process; and (iv) the evolution of the self-organization can easily be followed by freezing the dynamics at any instant simply by reducing the operating temperature below T_G. However, apart from the polymers, in the recent past it is also realized that the self-organized instabilities of the smart or functional materials can be another exciting area of research. In this direction, the self-organized instabilities of various smart materials such as conducting polymers, block-copolymers, polymer blends, and LCs, have started gaining a lot of attention. In this thesis, we take up a number of unexplored areas associated with the self-organized instabilities of the LC droplets and ultrathin films.

It is now well established that the LCs are one of the states of matter having solid like orientational order and liquid like fluidity. The LCs show anisotropic physical properties owing to the presence of the orientational order in the molecular arrangements. They show tuneable optical, electric, magnetic, thermal, and mechanical properties under various external stimulus, which is perhaps the backbone of the modern day display units of televisions, computers, digital watches, and temperature sensors. All these technologies employ the capacity of the LC materials to precisely adjust the director field orientation

with the variation in the externally applied electric or magnetic and temperature fields. LCs are also employed extensively used in the optical imaging of in-situ diagnosis, switchable windows for light transmitters and reflectors, bullet proof vest, heavy duty ropes, and puncture resistant tubes. The previous studies associated with the various aspects of the LCs suggest that the fabrication of nanoscale LC patterns such as droplets, holes, pillars, stripes, or columns, with large area ordering is one of the most challenging tasks. This is because, while in one direction, the conventional micro or nanofabrication techniques such as the lithography struggle to size down the macroscopic structures of LCs owing to the presence of the liquid like fluidity. On the other hand, the self-organization of the LC materials often leads to microstructures rather than the nanoscopic ones owing to the presence of the restoring elastic orientational order of the molecules. Thus, at this stage, the invention of low-cost self-organized methodologies, which can produce high-density nanoscale LC patterns with can facilitate the design and development of next generation nanoelectronic displays, nanopolarizer arrays, optical nanoresonators, photon quibits, high-performance photovoltaics, electro-optical switches, optical wave guides, and beam scanners for high frequency imaging. In view of the above, the five major research objectives are laid down in the following manner:

- In the beginning, we study the pattern directed dewetting of ultrathin polymer films to fabricate ordered nanostructures.
- The second objective is aimed to study the solvent vapour mediated spontaneous healing of self-organized defects of liquid crystal films.
- In the third objective, we explore the pattern directed phase transition of the nematic, smectic, and crystal state ultrathin films.
- As the fourth objective, we study the pattern directed ordering of spin-dewetted liquid crystal micro or nanodroplets.
- The final objective is to study the solvent vapour mediated contact line instabilities of liquid crystal droplets.

Chapter 2: Pattern Directed Dewetting of Ultrathin Polymer Films to Fabricate Ordered Nanostructures

In this chapter, the pathways to fabricate self-organized nanostructures have been identified exploiting the instabilities of ultrathin (< 100 nm) polystyrene (PS) films on the polydimethylsiloxane (PDMS) substrates loaded with discrete and closely packed gold nanoparticles (AuNPs). The AuNPs were deposited on the PDMS substrates by chemical treatment and the size and periodicity of the AuNPs were varied before coating the PS films. The study unveils that the physicochemical heterogeneity created by the AuNPs on the PDMS surface could guide the hole-formation stage of dewetting, the average spacing between the holes formed during the dewetting process, and the droplets formed at the later stage of dewetting. The size and spacing of the holes and the droplets

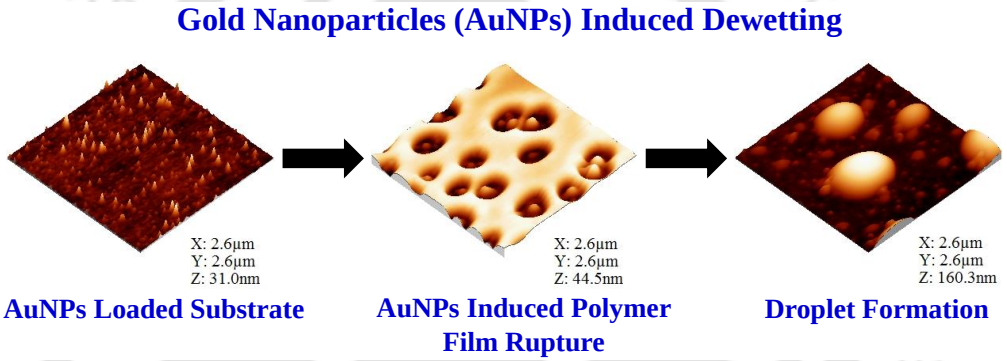

Figure 1: The images show the dewetting of PS films on the PDMS substrates loaded with AuNPs.

could be tuned by varying the nanoparticle loading on the PDMS substrate. Interestingly, as compared to the dewetting of PS films on the homogeneous PDMS surfaces, the AuNP guided patterns show a tenfold miniaturization, leading to the formation of the nanodroplets of diameter ∼550 nm. The spacing between the droplets could also see a tenfold reduction resulting in high-density random patterns on the PDMS substrate. Moreover, on a single substrate two different sizes of polymer drops were generated by placing the mask on PDMS substrate and exposing to UVO for lyophobic and lyophilic patterns preparation. The reported results can be of significance in the fabrication of high-density nanostructures and selective ordered in drop diameter exploiting the self-organized instabilities of thin polymers films.

Chapter 3: Solvent Vapour Mediated Spontaneous Healing of Self-Organized Defects of Liquid Crystal Films

In this chapter, we show that the ultrathin LC films can undergo a nematic to isotropic

transition when exposed to solvent vapour for a short duration while a reverse isotropic to nematic transition was observed when the film was isolated from the solvent exposure. The phase transitions were associated with the appearance and fading of surface patterns as the solvent molecules diffused into and out of the film matrix, resulting in destruction or restoration of the orientational order. A long-time solvent vapour exposure caused the dewetting of the film on the surface, which was indicated by the formation of holes and their growth in size with progress in time. Even at this stage, withdrawal of

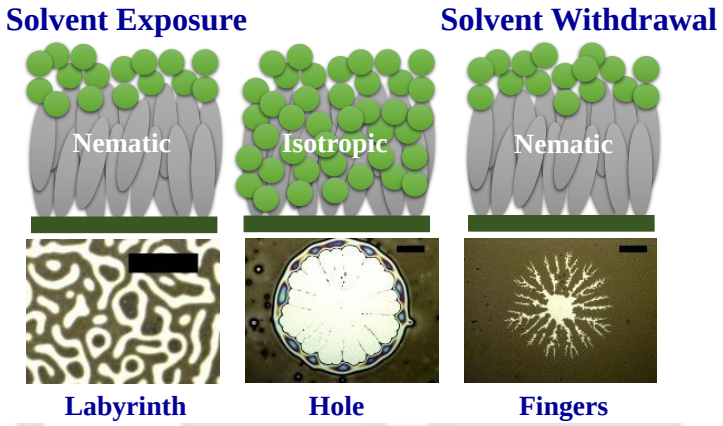

Figure 2: The images schematically show the solvent vapour annealed phase transition, hole-formation, and hole-healing of a LC film.

the solvent exposure produced an array of nematic fingers, which nearly self-healed the dewetted holes. The change in the contact angle due to phase transition coupled with the imbalance of osmotic pressure across the contact line due to the differential rate of solvent evaporation from the film and the hole helped the fingers to grow towards the centre of the hole. The appearance of the fingers upon withdrawal of the solvent exposure and their disappearance upon exposure to solvent were also found to be nearly reversible process. The findings could significantly contribute in the development of vapour sensors and self-healing surfaces using LC thin films.

Chapter 4: Pattern Directed Phase Transition of the Nematic, Smectic, and Crystal State Ultrathin Films

In this chapter, we show that a host of solvent vapour annealed phase transitions of LC films have been explored targeting various applications. While the solvent exposure led to the crystalline or semctic phases to transform into the nematic and isotropic phases, the reverse phase transitions from isotropic to nematic phase and from nematic to smectic or crystalline phases have been observed upon the withdrawal of the solvent vapour source. The phase transitions were found to be repeatable in nature with the periodic

exposure and withdrawal of the solvent exposure and were found to be very similar to the thermally annealed phase transitions. The only exception was that for the solvent vapour annealing the entire process could be carried out under the ambient conditions. Exploiting this phenomenon, emulating the principles of LC thermometers, the time required for the phase transition of a thin LC film resting on a solid substrate was correlated with the vapour pressure and volatility of different aromatic and non-aromatic solvents. The times for phase transition under different solvent exposures were found to linearly reduce with the increase in the vapour pressure and volatility of the solvents. Further, the solvent annealed phase transitions of a gold nanoparticle-5CB composite

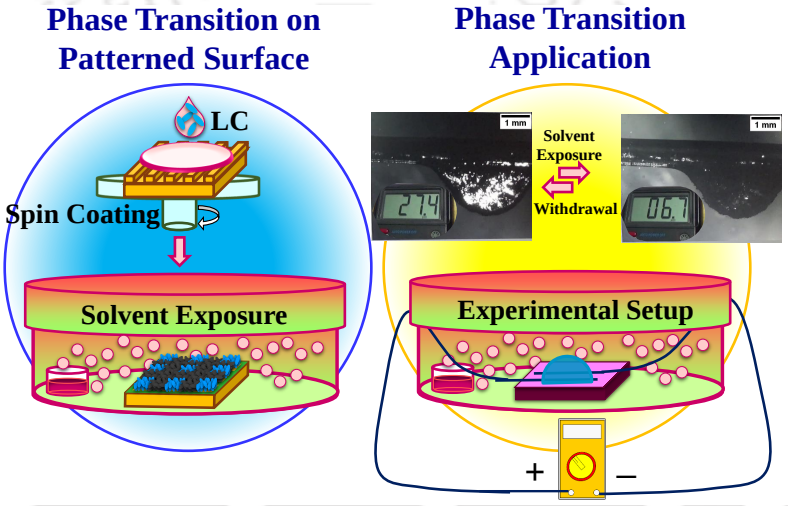

Figure 3: The images show the solvent vapour annealed phase transition of LC films on the patterned surface. And images also show application of phase transitions by change in electrical resistance.

LC droplet were converted into an electrical signal with the help of a simple external circuit. The experiments showed that the electrical resistance reduced (increased) upon the destruction (restoration) of the orientational order of the droplet. The electrical responses could be employed to sense the presence and absence of different volatile organic vapours, phase transition of LC materials, evaluation of the order parameter of an LC material during phase transition, rate of diffusion and absorption of a solvent into an LC matrix, and the rate of desorption and evaporation of a solvent from an LC matrix. Finally, the solvent annealed phase transition of the LC materials on the physically and chemically heterogeneous surfaces shows a pattern directed phase transition. While in the physically heterogeneous surface, the variations in the thicknesses ensured that the nematic to isotropic phase transition was faster (slower) at the thinner (thicker) regimes and in the chemically heterogeneous surfaces the weaker (stronger) anchoring of the

LC molecules on the lyophobic (lyophilic) patches ensured a faster (slower) due to less (more) solvent was required in both to destroy molecular orientation during the solvent vapour exposure. The reported phenomena could easily be exploited to develop LC based devices to identify the physical or chemical defects on the surfaces alongside the measurement of the extent of lyophobicity or lyophilicity of the surfaces.

Chapter 5: Pattern Directed Ordering of Spin-Dewetted Liquid Crystal Micro or Nanodroplets

In this chapter, we discuss that the chemical pattern directed spin-dewetting of a macroscopic droplet composed of a dilute organic solution of LC formed an ordered array of micro and nanoscale LC droplets. Controlled evaporation of the spin-dewetted droplets through vacuum drying could further miniaturize the size to the level of 90 nm. The size, periodicity, and spacing of these mesoscale droplets could be tuned with the variations in the initial loading of LC in the organic solution, the strength of the centripetal force on the droplet, and the duration of the evaporation. The patterned LC droplets showed a reversible phase transition from nematic to isotropic and vice versa, with the periodic exposure of a solvent vapour and its removal. A similar phase transition behaviour was also observed with the periodic increase or reduction of temperature suggesting their usefulness as vapour or temperature sensors. Interestingly, when the spin-dewetted droplets were confined between a pair of electrodes and an external electric field was applied, the droplets situated at the lyophobic patches showed light-reflecting properties under the polarization microscopy highlighting their importance in the development of micro or nanoscale LC displays. The digitized LC droplets, which were stationary otherwise, showed dielectrophoretic locomotion under the guidance of the external electric field beyond a threshold intensity of the field. Remarkably, the motion of these droplets could be restricted to the lyophilic zones, which were confined between the lyophobic patches of the chemically patterned surface. The findings could significantly contribute in the development of futuristic vapour or temperature sensors, light-reflectors, and self-propellers using the micro or nanoscale digitized LC droplets.

Chapter 6: Solvent Vapour Mediated Contact Line Instabilities of Liquid Crystal Droplets

A LC microdroplet could rapidly spread upon solvent vapour annealing to form a non-uniform film of solvent-LC solution on a PDMS substrate, which disintegrated into a

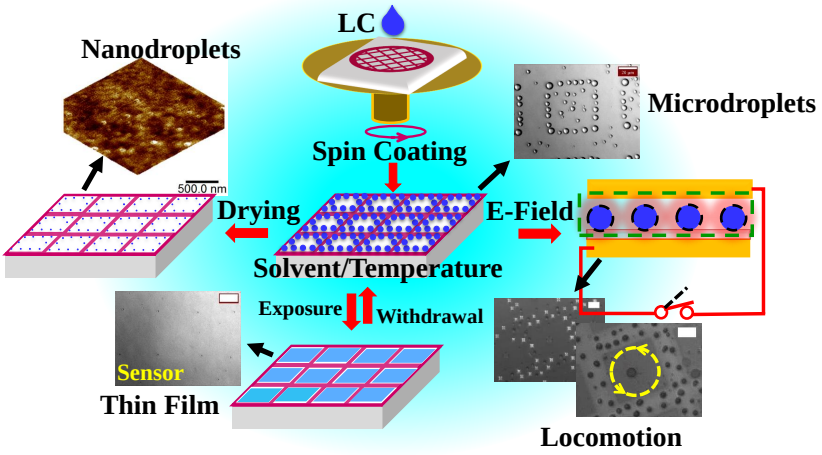

Figure 4: The images show the fabrication of the ordered spin-dewetted LC nanodroplets on the patterned surfaces. The images also show the pathways to self-propel the LC microdroplets under electric field.

collection of nanodroplets of LC upon the withdrawal of the solvent exposure. Initially, upon solvent vapour annealing the LC droplet underwent a phase transition from nematic to isotropic state at room temperature before spreading into a non-uniform film upon absorption of solvent. In this situation, withdrawal of the solvent exposure caused an instability near the contact line to facilitate the formation of the droplets having size and periodicity as low as ∼100 nm and ∼200 nm, respectively. While the

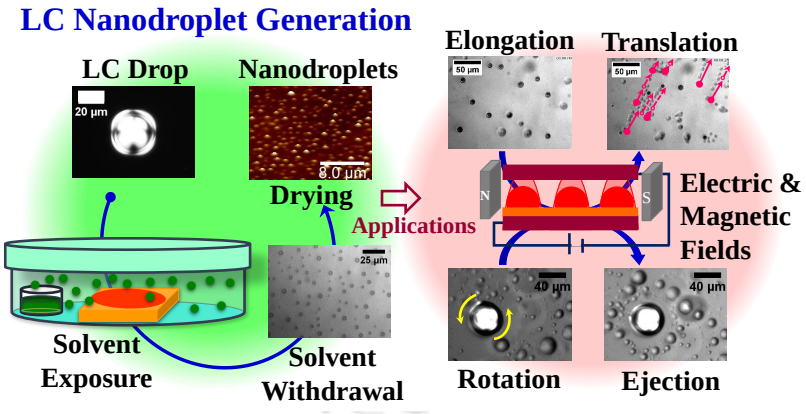

Figure 5: The images show the fabrication of the ordered LC nanodroplets through the contact line instabilities upon solvent vapour annealing. The images also show the pathways to self-propel the LC microdroplets under the action of Lorentz force.

lyophobic surfaces restricted the spreading of the droplet to form thicker films upon solvent the vapour exposure, the lyophilic substrates allowed the formation of thinner films under similar condition. Thus, upon the withdrawal of the solvent exposure, the lyophilic surfaces allowed the formation of the droplets having smaller size and periodicity. Use of a chemically patterned substrate with periodic lyophobic and lyophilic

patches could direct these instabilities in such a manner that a large area ordering of the nanodroplets were observed. A simple theoretical model of an evaporating droplet composed of a solution of an LC solute and a volatile solvent uncovered that the spacing of the droplets was decided by the interplay between the stabilizing and destabilizing components of the capillary forces for relatively thicker films while the van der Waals interaction played a supportive role when the thickness of the LC-solvent film was less than 100 nm. Interestingly, when these microdroplets were brought under the exposure of an electric field employing an experimental setup similar to electrowetting process, they showed an anomalous oscillatory rotational motion originating from the difference in the Laplace pressure around the contact line. Further, at higher field strengths application of Lorentz force to these rotating droplets showed exciting translational motion and ejection of miniaturized droplets. Concisely, the study demonstrates a single-step room temperature process to fabricate an array of nanoscale lenses of LC, which can be of significance in the developments of nanoscale locomotives, oscillators, rotors, optical, electronic, and energy harvesting devices.

Chapter 7: Conclusions and Scope for the Future work

In conclusion, the thesis deals with a number of unexplored problems associated with the self-organized instabilities of the LC droplets and ultrathin films. The study on the pattern directed dewetting of the ultrathin polymer film uncovered a unique way of substrate patterning using gold nanoparticles, which helped in developing polymer nanodroplets. It may be noted here that most of the previous works employed thermal annealing of the LC films to study the various self-organization processes. In the Chapter 3, arguably, for the first time we show the solvent vapour mediated phase transition and dewetting of the LC films at room temperature. We also showed the dewetting of the film through hole formation due to solvent exposure followed by the spontaneous healing of holes with the withdrawal of the solvent annealing. The study uncovered the potential of the LC materials for self-healing under solvent vapour annealing. In the Chapter 4, we demonstrate the underlying physical or chemical patterns decorated on the substrate can cause a pattern directed phase transition of the LC films upon solvent vapour annealing at room temperature. Further, we have shown the diverse phase transition behaviours of semctic, and crystalline states of the LC films under solvent vapour annealing. Importantly, various solvents with different solubility and vapour pressure could show different times for phase transition, which can be employed to develop LC

based devices to estimate solubility and vapour pressure of materials. In the Chapter 5, we showed that the spin-dewetting of the macroscopic LC droplets could form high-density ordered LC nanodroplets, which can be employed as reflectors or self-propellers under the influence of an external electric field. In the Chapter 6, we described the formation of LC nanolenses from the solvent vapour mediated contact line instabilities of LC droplets. A simple theoretical model of an evaporating droplet composed of a solution of an LC solute and a volatile solvent could predict the experimental spacing between the LC nanodroplets formed. We also show that the application of electric field and magnetic fields could lead to interesting self-spinning, self-propulsion, and droplet ejection behaviours. Concisely, the study demonstrates a number of interesting self-organized behaviours of LC droplets and films, which can be of significance not only in the fabrication of high-density nanoscale LC patterns but also will contribute to the developments of the futuristic nanoscale locomotives, oscillators, rotors suitable for various optical, electronic, and energy harvesting devices. The research problems reported here can be extended in future for,

1. The studies on the spin-dewetting can be extended to different other LC materials such as the discotic or smectic or polymeric LCs.

2. The studies on the breakup of the droplets under solvent vapour annealing can be extended to different other LC materials such as the discotic or smectic or polymeric LCs.

3. The studies on the self-healing of the LC materials under solvent vapour annealing can be extended to different other LC materials such as the discotic or smectic or polymeric LCs.

4. The response of the nematic LC materials under various solvent exposure can be extended to develop vapour sensors.

5. The micro and nanaoscale lenses fabricated employing the spin-dewetting and the LC droplet breakup can be extended for the commercial production of micro or nanolenses compose of LCs.

Contents

List of Figures

Nomenclature

Acronyms

5CB	4-*n*-Pentyl-4′-Cyanobiphenyl
7CB	4-*n*-Heptyl-4′-Cyanobiphenyl
8CB	4-*n*-Octyl-4′-Cyanobiphenyl
B	Magnetic Field
F	Lorentz Force
J	Current Density
AFM	Atomic Force Microscopy
Au	Gold
AuNPs	Gold Nanoparticles
CNI	Crystal to Nematic to Isotropic Transition
CS	Crystal to Smectic Transition
Cu	Copper
DAuNPs	Dodecanethiol Functionalized Gold Nanoparticles
DC	Direct Current
IN	Isotropic to Nematic Transition
LC	Liquid Crystal
Mw	Molecular Weight
NI	Nematic to Isotropic Transition
OTS	Octadecyltrichlorosilane
PDMS	Polydimethylsiloxane
PS	Polystyrene
rpm	Rotations per Minute
Si	Silicon
SN	Smectic to Nematic Transition

SNI Smectic to Nematic to Isotropic Transition

TOAB Tetraoctylammonium Bromide

UVO UV/Ozone

v/v Volume/Volume

w/v Weight/Volume

XRD X-ray Diffraction

Greek Letters

Δm_s Mass Evaporated

$\Delta m_s/\Delta t$ Rate of Evaporation of Solvents

Δt Time

γ Surface Tension

γ_{ps} Surface Tension of Pure Solvent

κ Curvature of the free Deforming Surface

λ Periodicity of the Surface Features

λ_m Minimum Value of Surface Features

μ Fluid Viscosity

ω Growth Coefficient

ω_m Dominant Growth Coefficient

ρ Fluid Density

Symbols

I Identity Vector

$\tilde{h}$ Perturbed Film Thickness

$\tilde{P}$ Perturbed Pressure

A_e Hamaker Constant

C Concentration

C_i Initial Concentration

D_d Diameter of the Dewetted Droplets

$D_{Au,avg}$ Average Diameter of the Particles

D_{Au} Diameter of AuNP

E Rate of Evaporation of Solvent

e_0 Rate of Evaporation of Pure Solvent

f	Frequency
F_s	Spacing of the Fingers
h	Film Thinkness
h_0	Mean Film Thickness
k	Wave Number
L_f	Length of the Fingers
m	Slope of the Variation in Surface Tension
m_s	Mass of the Solvent
N_d	Number of Droplets
P	Total Pressure
p	Fluid Pressure
p_0	Ambient Pressure
P_v	Vapour Pressure of the Solvents
R	Surface Roughness
r	Radial Coordinate
R_0	Maximum Electrical Resistance
r_A	Rate of Absorption
r_D	Rate of Desorption
R_H	Radius of Hole
R_m	Minimum Electrical Resistance
R_N	Normalized Electrical Resistance
S	Orientational Order
S_d	Spacing between the Dewetted Droplets
S_H	Spacing between the Holes
T	Ambient Temperature
t	Time
t_0	Time at Maxium Resistance
T_G	Glass Transition Temperature
T_L	Lower Temperature
t_m	Time Required to Reach Minimum Resistance
t_n	Time Required to Reach Initial Resistacne

T_P	Phase Transition Temperature
T_U	Upper Temperature
t_{IN}	Time Required for IN transition
t_{NI}	Time Required for NI Phase Transition
t_{UVO}	UVO exposure time
V	Volume of the Solvent
v_r, v_z	Velocity Components
z	Axial Coordinate

Chapter 1

Introduction

1.1 Ultrathin Film

Ultrathin films are defined as the coatings of very small thicknesses ranging from a few microns to even a few nanometres [1]. These films are ubiquitous in a number of naturally occurring phenomenon such as the formations of frost, soot, bubble or foam, the pre-corneal film on the eyes or the mucus layer on the organs, extra cellular matrix or cell membrane, epidermal skin, protective layers on egg, and waxing on the plant leaves, to mention a few [2]. In the recent years, ultrathin films of polymeric or functional materials have attracted a lots of attention due to their significance in many cutting-edge applications. For example, these films have been extensively used in the, (i) reflective, antireflective, or refractive optical coatings [3, 4]; (ii) protective coatings on micro or nanoelectronic chips and mechanically moving parts [5]; (iii) functional coatings on the magnetic recording media [6] and semiconductor devices; (iv) liquid crystal displays (LCDs) [7] and light emitting diodes (LEDs) [8]; (v) active and hole transport layers in the solar cells [9]; (vi) electrochemical or fuel cells and batteries [10]; (vi) sensors and actuators [11]; and (vii) biomedical applications [12]. Later, the scientific understanding on the dynamics of the ultrathin films has evolved a lot over the years. Presently, a number of fundamental phenomena have been studied in the laboratories following the dynamics of ultrathin films such as, phase change- phase separation [2], wetting-dewetting [13], flotation-sedimentation [14], emulsification-coalescence [15], foaming-defoaming [16], adsorption-desorption [17, 18], and adhesion-debonding [19].

1.2 Film Deposition

Ultrathin films can be deposited following many different pathways. The methodology for deposition is chosen based on the requirements of the thickness and uniformity of the film. Typically, the deposition techniques are classified into two main sub-categories such as physical and chemical. In physical deposition method, the thin film is deposited on a solid substrate with the help of a mechanical or thermal process while in the chemical method, the deposition takes place on a solid substrate by chemical conversion of a precursor on the target substrate.

1.2.1 Physical Deposition

Evaporation, sputtering, electrohydrodynamic (EHD), and epitaxial pathways of depositions are some common examples of physical deposition methods [1]. In evaporation, the source to be deposited is heated electrically to convert the same into gas under vacuum, which travels to a target due to a small pressure gradient maintained near the same [20]. In comparison, sputtering is the most desirable deposition technique for compounds or mixtures wherein the deposited material is converted into plasma with the help of an inert gas (e.g. argon) and laser or electrical arc before deposited on a target substrate [21]. The EHD deposition is a relatively more advanced technique wherein the source material is fed as a solution to a capillary nozzle. One end of the nozzle and the substrate are connected with two opposite electrodes, later a high field intensity is generated [22]. As a result, Taylor cone is formed at end of the drop of the pumping liquid, which emanates electrically charged droplets to be deposited as the film on the target substrate. Molecular beam epitaxy is a more advanced deposition technique where an overlayer is epitaxially grown on a crystalline plane to cause a layer after layer deposition of target molecules as thin films [23].

1.2.2 Chemical Deposition

Plating or chemical bath deposition, Langmuir-Blodgett deposition, spin or dip-coating, chemical vapour deposition, plasma enhanced chemical vapour deposition, and atomic

layer deposition are some of the well-known chemical deposition methods. Plating or chemical bath deposition is known for depositing accurate crystalline phases of thin film [24]. On the other hand, Langmuir-Blodgett method deposits mono or multilayer of polymers, nanoparticles and lipids [25]. In this method, initially a liquid precursor is dispensed on an aqueous sub-phase. Following this, the scattered floated molecules are compressed mechanically before depositing on a solid substrate by controlled dipping and lifting of a substrate into the sub-phase to deposit mono or multilayer of molecules. In comparison, spin-coating is a relatively simple and inexpensive thin film deposition technique in which a solute-solvent solution is spun at a high velocity to spread the same on a substrate [26]. After casting, the films are obtained by evaporation of the solvent. The film thickness in this method is controlled by varying the solute loading, spin-speed, viscosity, and volatility of the solvent. In dip coating, the target fully submerged into a solution before withdrawn in a controlled manner and dried. The film thickness in this method is controlled by based on speed of withdrawal, viscosity of the solution, and volatility of the solvent [27]. In comparison, the chemical vapour deposition or plasma enhanced chemical vapour deposition are very complex and costly processes, which use gas or plasma precursor for reactive deposition of materials on the target [28]. In the atomic layer deposition, unlike the chemical vapour deposition process, reactants are deposited stage wise before chemical reactions take place to form a film of desired composition on the substrate [29].

Importantly, the efficiency of the deposition of ultrathin films on solid substrates is decided based on, the minimum amount of material deposited, uniformity of the film thickness, roughness of the film surface, area of film deposition, portability of the process, cost-effectiveness, eco-friendliness, and repeatability.

1.3 Dynamics of Ultrathin Liquid Films

Ultrathin liquid films (< 100 nm) show interesting self-organized instabilities to rupture spontaneously into various interesting morphologies such as holes, droplets, rods, pillars, channels, and labyrinths [30]. From the perspective of a coating technology the breaking of the ultrathin films has been a serious disadvantage, which led to an extensive research

spanning over past few decades. These efforts are mainly aimed for better understanding of the stability and dynamics of the thin films. In particular, the number of fundamental works on these systems have increased very fast since early 90's owing to the use of polymers rather than the commonly available simple inorganic or organic liquids [31]. The polymers provided many important advantages in studying these systems such as, (i) they have less volatility than the commonly available liquids, which helps in studying the dynamics in absence of evaporation; (ii) they are solid at room temperature and can easily be made to flow beyond their T_G; (iii) the viscosity of the polymers beyond their T_G is high, which helps in slowing down the kinetics of the process; and (iv) the evolution can easily be followed by freezing the dynamics at any instant simply by reducing the operating temperature below T_G [31].

It is now well understood that a liquid film of thickness less than 20 nm is unconditionally unstable due to the dominance of the destabilizing van der Waals forces on the stabilizing component of the surface tension force [31–34]. This phenomenon is also popularly known as the spinodal dewetting in which the mechanical or thermal fluctuations present in the surroundings grow to form surface undulations in the beginning of the process. At this stage, the time and length scales of these undulations are in general decided by the interplay of the intermolecular and surface tension forces [30, 35–38]. Following this, these surface undulations grow to form random holes on the film [13, 15, 39–44]. Later, the holes grow to achieve equilibrium contact angle and coalesce to form network of liquid ribbons, which eventually undergoes Rayleigh-Plateau instability to finally form a collection of the droplets [31, 35, 45, 46].

In comparison, relatively thicker films dewet following the heterogeneous nucleation route [47–53]. In this mechanism, the physical [54–58] or chemical [59–63] defects present on the substrate or on the film surface generates an additional destabilizing force due to the lateral wettability gradient near the defect, which can dictates the hole formation stage of the dewetting process [64–69]. After the holes are formed, the hole-growth, hole-coalescence, and drop formation stages remain similar to the spinodal mechanism. A few studies have shown that, if the substrate is a low surface energy, during the hole growth stage the hole-rim can also undergo a secondary instability to generate micro or nanodroplets [70–74]. A number of recent works have highlighted that there can be

another pathway of the dewetting, namely, the spin-dewetting, in which the centripetal force due to the rotation during the spin-casting of a polymeric solution may for large-area micro or nanodroplets [75].

The different stages of dewetting of thin liquid films have been extensively investigated with the help of a number of theoretical [76–84] and experimental [54, 64, 85–92] analyses over the past few decades. These studies unveil that for the studies related to the dewetting the polymeric thin films are deposited on the silicon wafers of the glass or quartz substrates by the spin-coating process [93]. The film thicknesses are in general controlled by varying the polymer loading in the solvent and the spin-speed during the spin-casting. A solution of lower (higher) concentration and high (small) spin-speed leads to a film of smaller thickness [94]. After coating the films are annealed following the thermal [45] or solvent vapour [95] route, which eventually converts the film into a liquid one before any of the aforementioned dewetting mechanisms set in the dewetting processes.

Interestingly, the self-organized micro or nanopatterns generated by the dewetting of ultrathin liquid films are found have significant potential in improving the efficiency of a number of modern appliances which include memory devices [96], solar [97] or fuel cells [98], super-hydrophobic/hydrophilic surfaces or self-cleaning surfaces [99], digital micro or nanofluidics [100], optoelectronics [101], MEMS/NEMS [102], and biomedical applications [103]. The large-area micro or nanopatterns obtained from this methodology is found to be far more economical than the other conventional top-down patterning techniques such as focused ion beam etching [104], contact printing [105], ink-jet printing [106], photolithography [107], AFM lithography [108], electron beam lithography [109], and nano-imprint lithography [110]. Presently, one of the major challenges in the area of dewetting is the use of smart or functional materials such as LCs [111], carbon allotropes [112], biomolecules [113], conductive polymers [114], blended or block co-polymers [91], hydrogels [115], instead of simple polymers to improve the commercial viability of the process. In this thesis, we take up a number of unexplored areas associated with the self-organized instabilities of the LC droplets and ultrathin films.

1.4 Liquid Crystal

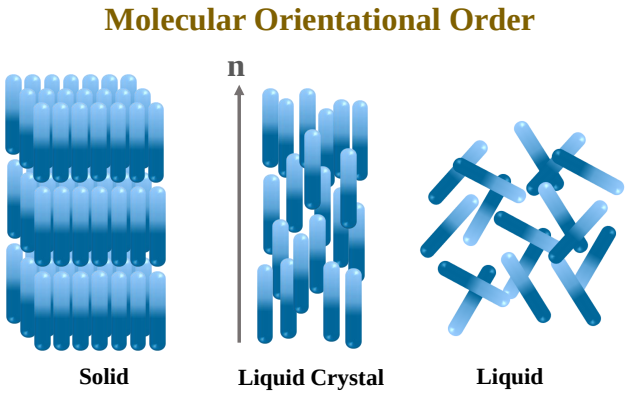

Figure 1.1: Molecular orientation of various states of matter.

LCs are one of the anisotropic states of matter between isotropic solid and liquid as shown in Fig 1.1. The state is also termed as the mesomorphic (intermediate form) or LC [116, 117]. Typically as shown in Fig. 1.1, in an isotropic solid state the molecules have a long-range positional and orientational order while these orders are absent in the isotropic liquid. The LC phase possesses only the solid like oreintational order while the positional order goes missing in this state owing to the inherent fluidity [116, 117]. This is the reason the LCs show solid like optical, thermal, electrical, magnetic, and mechanical properties while they also show liquid like fluidity and coalescence [118, 119].

The presence of the orientational order of the LC phase emanates an order to the LC molecules, which is quantified by, $S = f(\theta)$, where θ is the angle between the long axis and the director orientation of the LC molecules. An order parameter of S of unity signifies a perfectly aligned LC sample while the value of zero signifies an isotropic liquid state [120]. The orientation order of the LC molecules are found to vary under the exposure of various external stimuli such as temperature [121], light [7], and electric[122] or magnetic fields [123]. The variations in the optical, thermal, electrical, magnetic, and mechanical properties of the LC materials under the influence of external stimulus have been exploited extensively to develop the modern display devices such as televisions, laptops, digital watches, computers, and advertising boards [124], flexible thermometers [125], UV screening glasses or switchable windows for light reflectors and transmitters [126], heavy duty ropes, bullet proof vests, puncture resistance tubes, optical imaging of in-situ diagnosis [127], mechanical stress measurement [128], RF wave-guides [129],

solar panels [130], biomedical devices [131], and organic electronics [132], among many others.

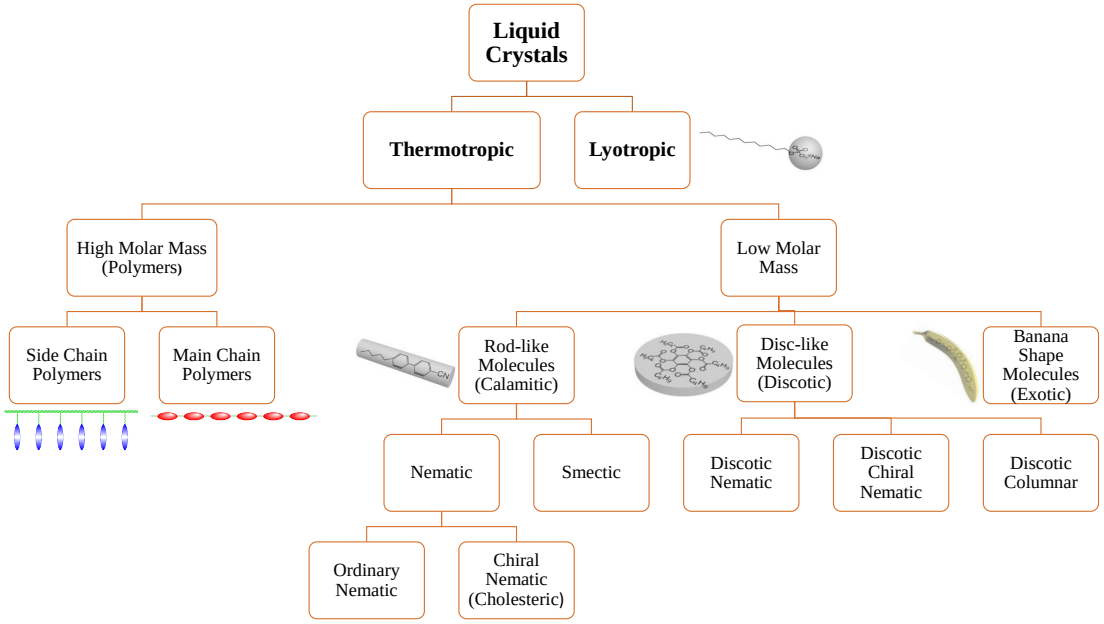

Figure 1.2: Classification of liquid crystal.

1.4.1 Classification of Liquid Crystal

Fig. 1.2 concisely shows that initially LCs are broadly classified into thermotropic and lyotropic based on their response to the external stimuli [133]. The thermotropic LCs show the phase change behaviour with the supply and withdrawal of thermal energy whereas while the lytropic LCs show the phase change with the chemical potential in a solution. The thermotropic LCs can be sub-classified into high (long chain polymer) and low molar mass LCs. Finally, they can be sub-classified based on their rod (calamatic), disc (discotic), or banana (exotic) shapes and also by the order parameter as nematic, chiral nematic (cholesteric), and smectic phases [116, 117].

1.4.1.1 Nematic Liquid Crystals

Nematic phase is perhaps the simplest phase among all the LC phases. The Greek word nematic has the meaning of thread, which resembles the thread like disclinations observed on the surface of a nematic LC surface. Fig. 1.3 shows that in the nematic

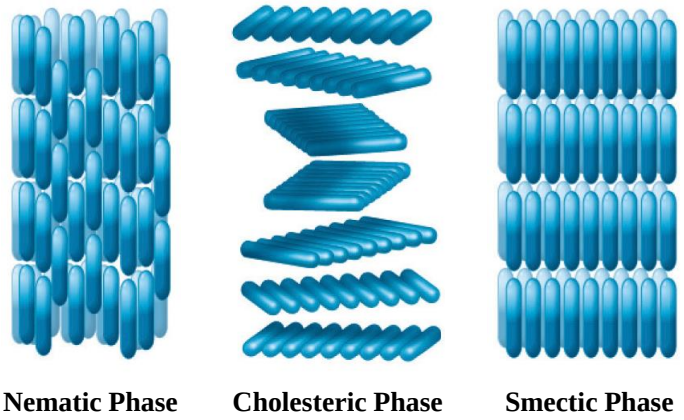

Figure 1.3: Phases of liquid crystal.

phase the building blocks are a collection of rod-like molecules with a rigid aromatic core and with flexible aliphatic tail. Typically, the orientation of the nematic LCs in the bulk are uniaxial, however, some are also available with biaxial orientations wherein the orientation of the molecules changes along with the director. Examples of nematic LCs are 5CB and 4′-(hexyloxy)-4-biphenylcarbonitrile, etc.

1.4.1.2 Cholesteric Liquid Crystals

The cholesteric LCs are also known as chiral nematic in which the one plane have a twist to its adjacent plane components due to the asymmetric orientation, as shown in the Fig. 1.3. The twist is in general of small degree of angle to ensure that the components have a long range chiral order. The full twist (360°) is called pitch, which is sometimes equal to the wavelength of the visible spectra leading to excellent Bragg reflection properties. Examples of cholesteric LCs are cholesteryl acetate, cholesteryl benzoate, and cholesteryl hemisuccinate, etc.

1.4.1.3 Smectic Liquid Crystals

Smectic liquid crystals have more ordered than other liquid crystals because of the presence of the positional order along with the orientational order. Unlike nematic or cholesteric liquid crystal phases the density of the smectic liquid crystals is not uniform

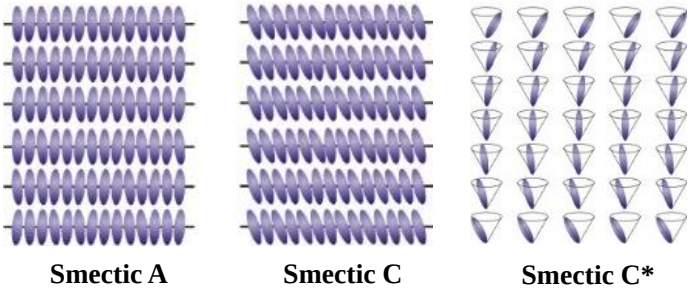

Figure 1.4: Sub-phases of smectic liquid crystal

across the space because there is correlation between the centre of mass of the molecules´.Moreover, the operative intermolecular forces are weaker than the intramolecular forces, which facilitates, the layers to move leading to a higly viscous soapy nature. Smectic liquid crystals are classified further based on packing formation and tilt of molecules with the layer normal. The sub-phases names are given from A to K in alphabetical order. For example, Smectic A, Smectic C, Smectic C*, and Smectic G, etc. are well known and widely used smectic liquid crystals for many applications.

Smecit A is a least ordered smectic phase. As shown in Fig. 1.4 it possesses a layered structure. Whereas, within this layer molecules are oriented in a nematic order and having one dimensional positional order. In Smectic C as shown the molecules are tilted in a single direction and having two dimensional positional order, as shown in Fig. 1.4. In Smectic C∗ as shown in Fig. 1.4 the molecular orientation is same as a cholesteric except that the molecules are tilted at an angle to a layer normal. Because of this molecular orientation in smectic C∗, they can show ferroelectric, ferrielectric, and antiferroelectric properties. Finally, in Smectic G liquid crystal the molecules are arranged in a three-dimensional tilt [134].

Unlike the nematic LCs, the smectic LCs have one dimensional positional order along with orientational order resembling the arrangement of books in a shelf, as shown in the Fig. 1.3. They are further classified into smectic A, smectic C, smectic C*, and smectic G phases based on their nature of the orientational orders. Examples of this phase are 4′-(octyloxy)-4-biphenylcarbonitrile (8CB), 4-(s,s)-2,3-epoxyhexyloxyphenyl 4-(decyloxy)benzoate (WP 46), 4-(decyloxy)benzoic acid, 4-(undecyloxy)benzoic acid, and 4-(heptyloxy)benzoic acid, etc.

Whenever LC molecules are brought near to the solid or liquid boundary the orientations of them change. The LC molecules weakly or strongly ‘anchor’ themselves in

either of homeotropic, planer, or angular orientations depending upon the properties of the confining surface. Largely, the properties of the confining surfaces are tuned either by mechanical or chemical treatment to impose a specific anchoring. For example, the LC molecules near the boundaries show, (a) planar anchoring when the confining surface is rubbed with a fabric in a particular direction [135], (b) homeotropic orientation when the substrates are treated with surfactants or by rotational oblique evaporation of silicon-oxide [136], and (c) angular anchoring when double deposition or simple oblique evaporation of the silicon-oxide is employed [137]. The anchoring conditions of the LC molecules near the boundaries are also found alter with the adhesive properties, polarity and cleanliness of the confining surface [138–140]. Importantly, the anchoring condition near the boundaries have significant influence on the direction orientation in the bulk [141–144]. While in a cell the LC molecules can be weakly or strongly anchored to the confining substrates, near a freely deformable surface the LC molecules are always weakly anchored. For example, when a LC droplet is placed on a silicon substrate it always wets the substrate [145, 146]. In such a scenario, the LC molecules show planar anchoring near the substrate and homeotropic anchoring near the free boundary [119, 121, 145, 147–150].

In the past few decades a lot of theoretical [151–156] and experimental [7, 121, 122, 147, 157–162] research works have been performed to study the instability and dynamics of the thin LC films. When the nematic LC films are heated above the NI phase transition temperature (T_P) the orientational nematic order of the LC molecules are destroyed and an isotropic liquid film is obtained [121, 145, 159, 160]. In this situation, the phase transition is indicated by the appearance and disappearance of the undulatory surface patterns. At this stage, if the isotropic material is cooled steadily below T_P, a reverse IN phase transition is observed where the orientational order of the LC molecules is restored. The NI and IN transitions with periodic heating and cooling around T_P are nearly a reversible process [121, 145, 155, 159, 160, 162].

Interestingly, when an LC film is converted into an isotropic liquid by heating above its phase transition point, the films may undergo spinodal dewetting when the thickness is less than 20 nm [147, 159, 160]. Previous studies argued that the long-range Lifschitz–van der Waals interaction [116, 117, 147, 159, 163], pseudo-Casimir force based

director fluctuations [154, 164], and the textures of the LC film surface [160] could be the different reasons for these instabilities. For the relatively thicker films the lateral wettability gradients near the physical or chemical defects stimulate the hole-formation following the heterogeneous nucleation pathway when the LC films are heated to the isotropic stage [147, 160]. After the hole formation, if the temperature is kept above T_P, the dewetting pathway remain similar to the isotropic films. In such a situation, the holes grow and coalesce to form a network of ribbon like structures before undergoing capillary instability to form micro or nanoscale isotropic droplets. These isotropic droplets can be converted into LC drops upon reduction in the T_P. Thus, the dewetting of ultrathin LC films above its T_P provide a simple self-organized recipe to form large-area LC micro or nanodroplets. It is important to note here that if the temperature brought below T_P at any stage of dewetting various anomalous self-organized behaviours are observed owing to the IN phase transition [165].

The prior-art suggests that the formation of large-area micro or nanopatterns composed of LC materials can be of significance in the design and development of the next-generation pixelated micropolarizer arrays [111], optical microresonators [166], photon qubits [167], high-performance photovoltaics [130], electro-optical switches [168], and beam scanners for high frequency imaging [169]. The possibilities are owing to the capacity of the LC materials to precisely modulate the director field reorientation under the influence of thermal, solutal, and electric or magnetic fields.

1.5 Objectives of the Thesis

In the view of above, at this stage, exploring the new pathways to generate high density micro or nanopatterns are very important. In this direction, a lot of research has been explored for generation of micro or nanoscale polymer structures, by solely under the influence of physical or chemical effects. However, the combined physicochemical effect on miniaturization and pattering of polymers has not been explored fully. Moreover, fabrication of nanoscale LC structures such as droplets, holes, pillar, stripes, or columns with large area ordering is again one of the challenging tasks. This is because the fluidity of the LC materials promotes deformation and coalescence of the mesoscale structures

developed by any conventional process such as the lithography. On the other hand, restoring orientational order of the film restricts the downsizing of the structures to the level of micro or nanoscale. Thus, there is an immediate need to explore the pathways to develop micro or nanostructures composed of LC materials with large-area ordering. In the present thesis, we show some of the very exciting and economical way to break down polymeric and LC films into large area micro or nanostructures following the self-organization routes. In this direction, the major five research objectives are:

1.5.1 Chapter 2: Pattern Directed Dewetting of Ultrathin Polymer Films to Fabricate Ordered Nanostructures

In this chapter, we study the possibilities of miniaturization and ordering via intensifying the self-organized instabilities of ultrathin polymer films by the combined influence of physicochemical defects, which are created by chemically deposited gold nanoparticles on a PDMS substrate. Due to the physicochemical patterns, which are deposited underneath the polymer films, a high-density micro or nanoscale polymer droplets are generated. In addition, the randomly distributed micro or nanostructures are aligned due to the controlled wettability gradient provided by the underneath patterned gold nanoparticles.

1.5.2 Chapter 3: Solvent Vapour Mediated Spontaneous Healing of Self-Organized Defects of Liquid Crystal Films

In this chapter, solvent vapour induced phase transitions of nematic LC thin films coated on silicon substrates has been studied at room temperature. The effects of different types of solvents have been studied on phase transition of LC films alongside comparing the results with the thermal temperature induced LC phase transitions. The study is extended further to study the dewetting of LC thin films due to solvent vapour exposure followed by the self-healing of the holes formed due to solvent vapour withdrawal.

1.5.3 Chapter 4: Pattern Directed Phase Transition of the Nematic, Smectic, and Crystal State Ultrathin Films

In this chapter, various solvent vapour induced phase transitions of other phases such as nematic, smectic, and crystal state LC thin films have been studied. The effects of different topographical and chemical patterns on phase transition of LC films has been also studied. Further, exploiting the response of the LC materials under the solvent vapour exposure, a simple vapour sensor has been developed emulating the LC thermometer. With the help of the sensor we could identify the presence and absence of different volatile organic vapours, phase transition of LC materials, evaluation of the order parameter of an LC material during phase transition, rate of diffusion and absorption of a solvent into an LC matrix, and the rate of desorption and evaporation of a solvent from an LC matrix.

1.5.4 Chapter 5: Pattern Directed Ordering of Spin-Dewetted Liquid Crystal Micro or Nanodroplets

In this chapter, an array of ordered micro or nanoscale LC droplets are generated by the controlled evaporation of the spin-dewetted LC microdroplets on the chemically patterned substrates. The miniaturization of the size and number density of the LC droplets have been explored by varying the initial loading of LC in the solution, spin-speed, and the duration of evaporation. In addition, we could show some simple applications by using these miniaturized LC micro or nanodroplets such as the solvent vapour sensor, temperature sensor, light reflectors, and self-propellers.

1.5.5 Chapter 6: Solvent Vapour Mediated Contact Line Instabilities of Liquid Crystal Droplets

In this chapter, a high-density micro or nanoscale LC droplets are generated by contact line instabilities of LC micro droplets. The contact instabilities are generated by simple exposure and withdrawal of the solvent vapour exposure to the droplet. The diameter and the number density of the droplets are further tuned by exploiting this contact line

instabilities of LC droplets on lyophilic substrates. The randomly distributed nanoscale structures are decorated into array of ordered LC droplets by the use of chemically patterned substrate. The miniaturized droplets thus generated could be show rotational or translational motions and satellite droplet ejection under the influence of the electric and magnetic fields.

Briefly, the thesis shows some very novel self-organized pathways to decorate large-area LC patterns on the surfaces. The results reported in thesis can be employed for a number of futuristic applications such as miniaturization of the LC cells or LC light reflectors, development of the self-propelling LC objects, development of the self-healing LC coatings, and LC based vapour sensors.

Chapter 2

Pattern Directed Dewetting of Ultrathin Polymer Films to Fabricate Ordered Nanostructures

2.1 Abstract

Pathways to fabricate self-organized nanostructures have been identified exploiting the instabilities of ultrathin (< 100 nm) PS film on the PDMS substrates loaded with both discrete and closely packed AuNPs. The AuNPs were deposited on the PDMS substrates by chemical treatment and the size and periodicity of the AuNPs were varied before coating the PS films. The study unveils that the physicochemical heterogeneity created by the AuNPs on the PDMS surface could guide the hole-formation stage of dewetting, the average spacing between the holes formed during the dewetting process, and the droplets formed at the later stage of dewetting. The size and spacing of the holes and the droplets could be tuned by varying the nanoparticle loading on the PDMS substrate. Interestingly, as compared to the dewetting of PS films on the homogeneous PDMS surfaces, the AuNP guided patterns show a tenfold miniaturization, leading to the formation of the nanodroplets of diameter ∼550 nm. The spacing between the droplets could also see a tenfold reduction resulting in high-density random patterns on the PDMS substrate. The reported results can be of significance in the fabrication of high-density nanostructures exploiting the self-organized instabilities of thin polymers films.

2.2 Introduction

In this chapter, we show that indeed dewetting a PS film on a PDMS surface decorated with periodic physicochemical patterns can indeed lead to droplets and holes of size and spacing in the nanoscale regime. The physicochemical substrates in this study were created by loading the activated surface of a PDMS film with AuNPs of size ranging from 25 – 250 nm. The placement of AuNPs of finite size on the PDMS surface ensured that the surface was physically heterogeneous. In addition, placement of discrete AuNPs on the PDMS surface ensured a sharp lateral wettability gradient near the junctions where the AuNPs attached to the PDMS surface, as schematically shown in the Fig. 2.1. The AuNPs of different size were loaded in different proportions on the PDMS surface to create the surfaces with different lateral wettability gradients. Remarkably, with the help of atomic force microscopy (AFM, Innova Iris, Bruker-Icon Analytical Equipment), we could experimentally locate physicochemical sites where the holes nucleated at the initial stages of dewetting. Further, we identified the pathways to control the size and the spacing of the nanoscopic holes nucleated in the beginning of the dewetting and the nanodroplets formed at the later stages of dewetting with the variation in the AuNP loading on the physicochemically patterned PDMS surface. The study also shows a simple way to fabricate these high-density nanostructures across the space. In addition, the methodologies to prepare the gradient surfaces with periodic high-density smaller and larger nanostructures of PS on a surface with physicochemical patterns were also shown. The results reported can be of significance in developing nanoscale patterns following the self-organized instabilities of polymer films.

2.3 Experimental Section

2.3.1 Materials

The PDMS was obtained from Dow Corning, India (SYLGARD® 184 kit). Among the other materials PS, sodium hydroxide (NaOH) pellets, 3-aminopropyltriethoxysilane (3-APTES, $C_6H_{17}NO_3Si$), gold (III) chloride solution (30%wt $HAuCl_4$: HCl), sodium

borohydride ($NaBH_4$), toluene (C_7H_8), hexane (C_6H_{14}), and ethanol (C_2H_5OH) were procured from Sigma-Aldrich. The copper TEM grids with 300 mesh (lines/inch) were procured from SPI supplies, USA, which had hole width, pitch, and bar width of 58 μm, 83 μm, and 25 μm, respectively. Among the other materials, 98% sulfuric acid (H_2SO_4), 50% hydrogen peroxide (H_2O_2), nitric acid (HNO_3), hydrochloric acid (HCl), and ammonium hydroxide (NH_4OH) were obtained from Merck (India). The AR grade chemicals were directly used for experiments without any further treatment. Si (<100> Orientation, Boron doped P type, resistivity 0.01 – 0.02 Ω cm) and quartz substrates were purchased from N. J. Int. Cop. and Macwin, India. Solutions were prepared by Milli-Q grade water and the glassware was thoroughly cleaned using aquaregia solution and Milli-Q grade water.

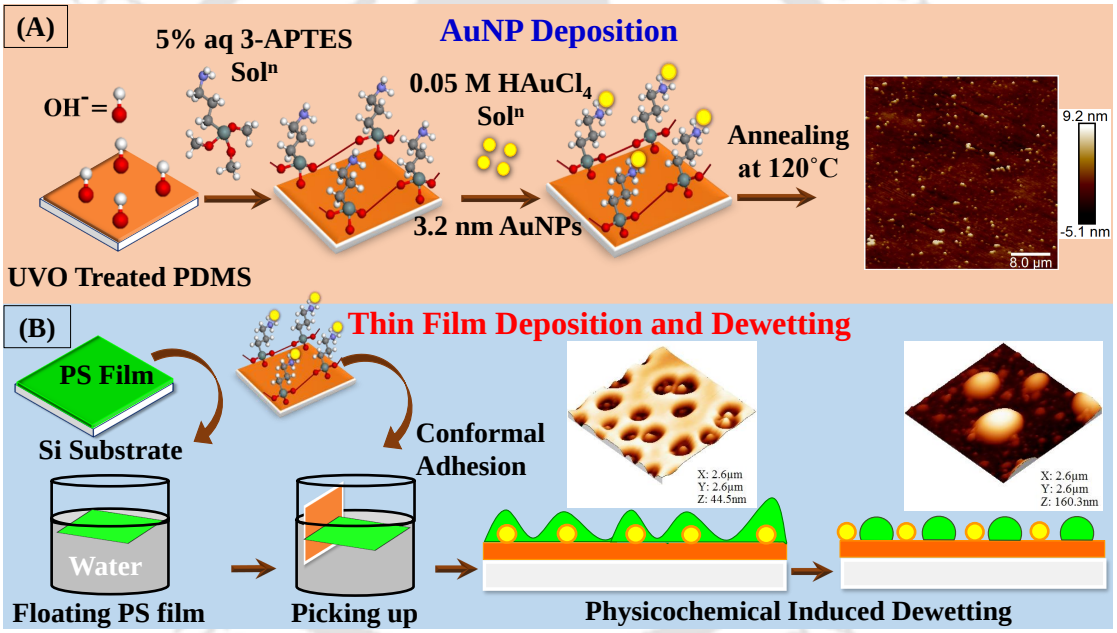

Figure 2.1: Schematic representation of experimental procedures. Image (A) shows the steps of the deposition of AuNPs on the flat PDMS substrate. Image (B) shows the procedure of transferring of the PS film on to the AuNP loaded PDMS substrate and subsequent dewetting of the film to form holes and droplets.

2.3.2 Methods

2.3.2.1 Deposition of AuNPs on PDMS Surface

The experimental procedure is schematically shown in the Fig. 2.1(A). The PDMS composed of an oligomer and a cross linking agent were mixed with hexane solvent

(10:1:110 - v/v/v) and then spin-casted (2500 rpm) on thoroughly cleaned Si substrates. After coating, the film was annealed in air-oven for 24 h at 120°C to simultaneously relax the film, evaporate out the solvent, and curing [170]. Thereafter, the PDMS surface was activated by treating them in UVO plasma treatment chamber (PSDP-UV4, Novascan Tech. Inc., USA) for different time durations varying from 5 – 30 min. The purposes of this treatment was to make the PDMS surface more lyophilic and reactive by replacing the lyophobic methyl groups on the surface with lyophilic hydroxyl groups [171–173]. Following this, the activated PDMS surface was treated with 5% (v/v) 3-APTES in ethanol solution for 40 min followed by a thorough cleaning with pure ethanol [172, 173]. The 3-APTES activated PDMS was then baked at 120°C for 1 h to complete the process of Si-O bond formation on the PDMS surface. Subsequently, AuNPs were immobilized on the silanized PDMS surface by drop casting the AuNP suspension on the film for 1 h and then dried for 1 h at 120°C. The AuNPs were synthesized by reducing gold (III) chloride solution (30% $HAuCl_4$: HCl) with $NaBH_4$ in NaoH solution [174]. The AuNPs stabilized on the PDMS surface was subjected to X-ray diffraction (XRD, Bruker) analysis. The peaks obtained for the Au during XRD analysis ensured that the AuNPs were stabilized on the PDMS surface before the PS films were coated.

2.3.2.2 Patterning AuNP Loaded PDMS Surface

In order to tune the position of the deposition of AuNPs on the PDMS surface, TEM grid was used to pre-pattern the PDMS surface. In this method, the TEM grid was placed on PDMS surface and then the exposed PDMS surface was treated in UVO chamber for different time durations ranging from 5 – 30 min in order to vary the degree of lyophilicity imparted on the PDMS surface. At the end of this process, we obtained PDMS surface with the patches of periodic lyophilic (exposed area) and lyophobic (masked area) zones. After the TEM grid was removed from the PDMS surface and previous protocol was followed to deposit AuNPs. With the help of this pre-patterned surface we could not only order the dewetted patterns but also could create periodic dewetted patterns of different size across the space, which helped in preparing a gradient surface [64].

2.3.2.3 Coating of PS Films on AuNP Deposited PDMS Surface

It may be noted here that direct spin-casting of the PS film on the AuNP coated PDMS surface may not lead to the systems with uniform thickness owing to the presence of the surface physical heterogeneities [49, 175]. In particular, presence of the AuNPs of size ranging from 25 – 150 nm ensured the films were relatively thicker in the domains where the AuNPs were absent. Thus, the chances of getting PS nanoparticles were very limited in such situations. Further, the physicochemical heterogeneities on the PDMS surface led to the rapid spin-dewetting [56] of the films when we intended to coat very thin films (< 15 nm) with very less initial PS loading in the solvent toluene. In order to avoid these limitations, we initially spin-casted the PS films (Mw = 280,000 g/mol) on clean and smooth pieces of Si wafer and then vacuum dried for 1 hour. Typically, the experiments suggested that 0.1%, 0.2%, 0.3%, 0.4%, 0.5%, 0.8%, and 1% (w/v) PS to toluene solution of spin-casted at 2500 rpm for 120 s led to average PS film thicknesses of, 5.83 ($\pm$ 0.13) nm, 12.18 ($\pm$ 0.38) nm, 18.68 ($\pm$ 0.075) nm, 25.78 ($\pm$ 0.175) nm, 29.28 ($\pm$ 0.13) nm, 49.95 ($\pm$ 0.25) nm, and 72.13 ($\pm$ 0.03) nm, respectively. Imaging Ellipsometer (EP3, Nanofilm, Accurion Scientific Instruments Pvt. Ltd.) was employed to measure the thickness of the coated PS films. After drying, the PS film was gently peeled from the Si substrate using a water surface and then vertically picked up on the AuNP coated PDMS surface to ensure conformal adhesion [49], as schematically shown in the Fig. 2.1(B). The film was then vacuum-dried for 1 h and then baked at 60°C for 24 h in order to evaporate the residual water. The PS film coated on the AuNP coated PDMS surface was then subjected to exposure of solvent vapour (toluene) in order to perform the dewetting experiments [64]. The dewetting pathways were followed by Optical Microscopy (Leica DM 2500M) where in situ observations were made with a CCD camera using white light in reflection mode. The different stages were dewetted samples were also characterized through AFM (Bruker, 5500 SPM, Agilent Technologies and Innova Iris, Bruker-Icon Analytical Equipment).

2.4 Results and Discussion

2.4.1 AuNPs Induced Dewetting

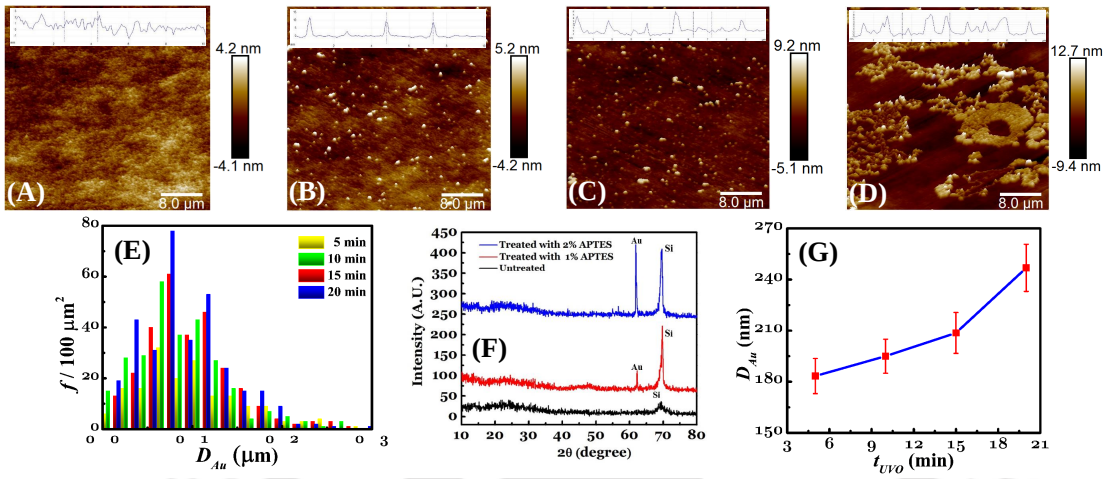

Figure 2.2: The AFM images (A) – (D) show the variation in the distribution of the AuNP morphologies on the PDMS surface with the variation in the UVO exposure time, 0 min, 5 min, 15 min, and 30 min, respectively. Inset images show the typical cross-sectional surface profile of images depicting the typical height and spacing of the AuNPs on the PDMS surface. Image (E) shows the corresponding frequency (f) versus diameter of AuNP (D_{Au}) plot. Image (F) shows the XRD image of PDMS surface coated with AuNPs. Images (G) shows the increase in D_{Au} of AuNPs with increasing UVO exposure time (t_{UVO}).

Figs. 2.2(A – D) show the AFM images of the surface with physicochemical patterns prepared from the aforementioned experiments when the duration of the UVO exposure was varied from 0 – 30 min. Fig. 2.2(E) shows the typical distribution of D_{Au} of the particles across the space at different times of UVO exposure. The curves in the Fig. 2.2(D) shows the XRD plots for the uncoated and the AuNP coated PDMS surfaces. The plots display characteristic diffraction peaks at $2\theta = 62.6°$ and $70°$ corresponding to the (220) and (311) crystallographic planes of Au and Si [176]. Figs. 2.2(A – F) show the AFM and XRD images, which together confirmed the presence of the AuNPs on the PDMS surface. Fig. 2.2(E) shows the variation in the $D_{Au,avg}$ of the particles with the variation in the time for UVO exposure (t_{UVO}). Briefly, the plots suggest that indeed the PDMS surfaces were randomly coated with AuNPs to develop a physicochemically patterned surface.

Fig. 2.3 shows the typical dewetted patterns of a PS film of thickness 13.1 ± 0.1 nm on a physicochemically patterned surface. The film thickness was chosen to be really

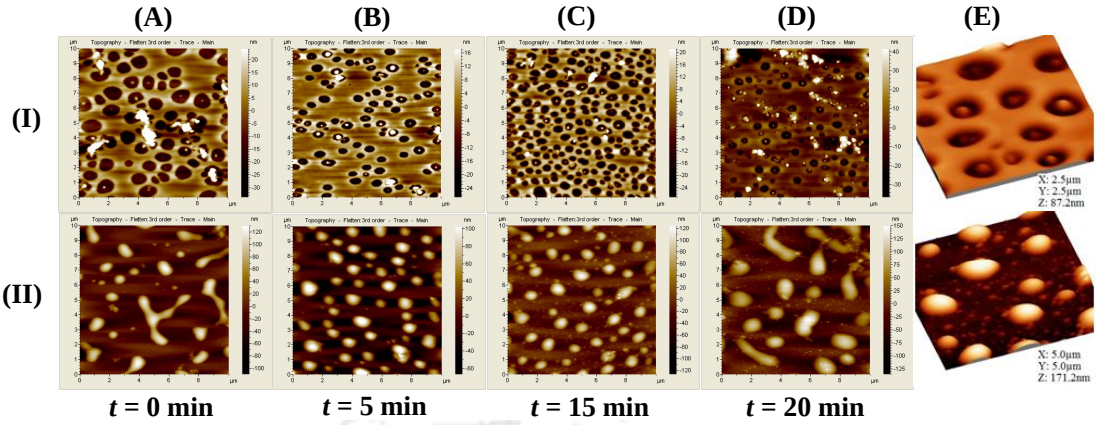

Figure 2.3: Images (A) – (D) in row (I) show the holes at the initial stages of dewetting when the PDMS surface was exposed with UVO for 5 min, 10 min, 15 min and 20 min, respectively, which led to the formation of the AuNPs of $D_{Au,avg}$ = 25 nm, 50 nm, 75 nm, and 150 nm, respectively. Images (A) – (D) in row (II) show the formation of nanodroplets at the final stages of dewetting corresponding to the images (A) – (D) in row (I). Images (IE) and (IIE) show the magnified image of shown the nucleation of the holes near the AuNPs at the initial stages of the dewetting the AuNP loaded PDMS surface at the later stages of dewetting. The PS film thickness is kept constant at 13.1 ± 0.1 nm for all the cases.

thin to ensure that the strength of the force was really strong ($f \propto \frac{1}{h^3}$), which enabled reducing the size and spacing of the dewetted structures. The Figs. 2.3(IA – ID) show the morphologies of the densely populated holes on the PS free surface at the initial stages of dewetting when the PDMS surface was loaded with AuNPs of diameter, 25 nm, 50 nm, 75 nm, and 150 nm, respectively. The magnified Fig. 2.3(IE) suggests that the holes nucleate exactly at the places where the AuNPs are integrated on the PDMS surface. The figures confirmed that in the present case the dewetting was guided by the physicochemical patterns present on the PDMS surface. The Figs. 2.3(IIA – IID) show the images at the late stage of dewetting after the droplets are formed on the PDMS surfaces loaded with AuNPs of diameter, 25 nm, 50 nm, 75 nm, and 150 nm, respectively. The magnified Fig. 2.3(IIE) suggests that at the late stages of dewetting the PS droplets were resting on the AuNP coated PDMS surface. Different information obtained from the Fig. 2.3 such as the spacing between the holes at the initial stages of dewetting (S_H) and the diameter (D_d) and spacing (S_d) of the dewetted droplets at the later stages of dewetting are summarized in the Fig. 2.4. The plots clearly suggest that all the three parameters could really be reduced significantly when the PS films were dewetted on the surfaces with physicochemical patterns. Interestingly, the plots suggest that when the size of the AuNPs were too small (e.g. 25 nm) or too large (e.g.

250 nm) the extent of miniaturization was not that significant. In comparison, when the size of the AuNPs were rather intermediate (e.g. 75 nm) we could observe the extent of miniaturization was largest, S_H = 500 nm, D_d = 500 nm, and S_d = 1.3 μm.

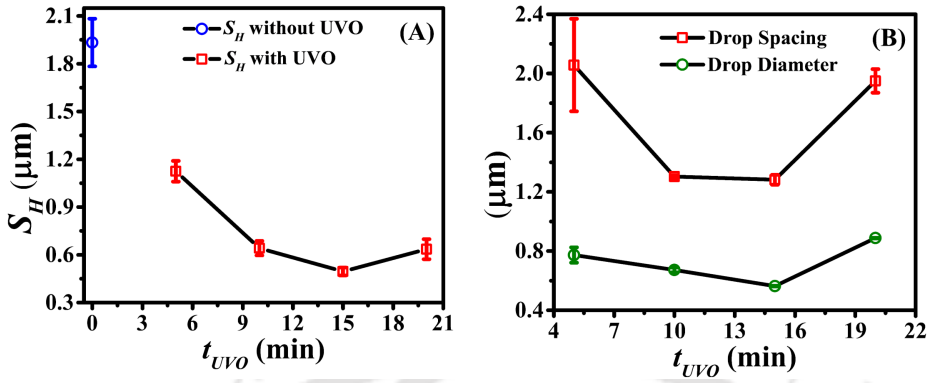

Figure 2.4: Variations in the spacing between the holes at the initial stages of dewetting (S_H) and the diameter (D_d) and spacing (S_d) of the dewetted droplets at the later stages of dewetting when the PDMS surface was exposed with UVO for 5 min, 10 min, 15 min, and 20 min, respectively, which led to the formation of the AuNPs of $D_{Au,avg}$ = 25 nm, 50 nm, 75 nm, and 150 nm, respectively, on the PDMS surface.

The experiments also suggested that the spacing between the AuNPs played a crucial role in miniaturizing the size of the dewetted morphologies as well as reducing the spacing between them. This is because when the AuNPs were small and densely populated on the PDMS surface it essentially led to a lyophilic Au surface with physical heterogeneities. Thus, in such a situation, the dewetting of the PS film was expected to follow the sole influence of the lateral wettability gradients originating from the physical patterns. On the other hand, when AuNPs were bigger in size and sparely populated on the PDMS surface, the PS film was expected to follow the length scale of dewetting associated with the PDMS surface apart from some nucleated dewetting on the zones of AuNP deposition. The experiments suggested that for the physicochemical surfaces an optimal spacing and size of the AuNPs were necessary in order to shift the length scale from a few microns to the level of sub-micron. Fig. 2.4 also highlights the maximum to minimum size of the droplets obtained during experiments, which suggests the frequent formation of 100 nm droplets during the experiments.

2.4.2 Ordering of Dewetted Structures

Fig. 2.5 shows the pathways to order the dewetted nanostructures formed on the physicochemically pattern surfaces. For this purpose, we initially placed one TEM grid on the PDMS surface and exposed it to the UVO for about 15 min. Since the TEM grid possessed holes of the shape of square boxes the UVO could convert the PDMS surface into a more lyophilic one in those locations. In comparison, the UVO exposure could not penetrate in the locations were the grid was placed, which ensured that those locations were relatively less lyophilic. In such a situation, when the AuNPs were loaded on the PDMS surface we observed that the lyophilic boxes were populated with AuNPs of smaller size (∼50 nm) and spacing (∼50 nm).

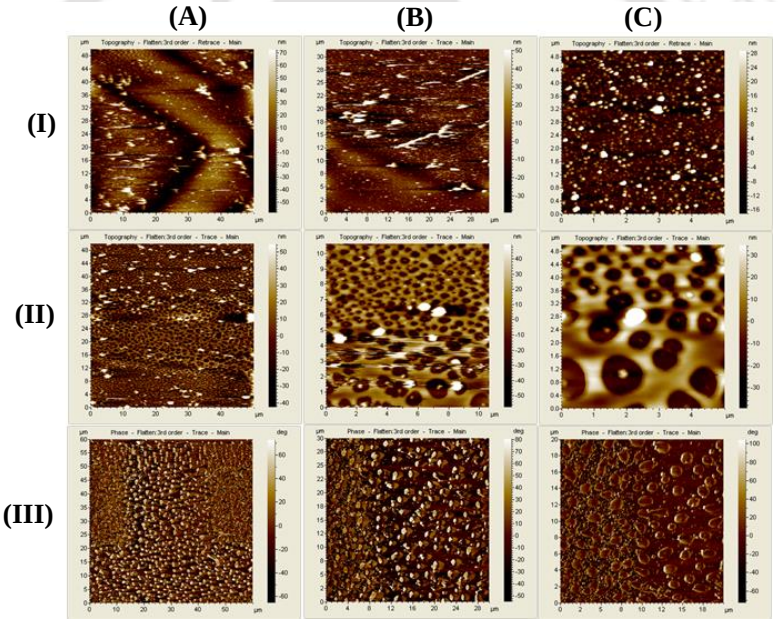

Figure 2.5: AFM images of the dewetting of a PS film (13.1 ± 0.1 nm) on a physicochemically patterned PDMS substrate using a TEM grid. In the row (I), images (A) shows the AuNPs distribution on both the exposed square box area (58 μm × 58 μm) and the unexposed channels at the periphery of the areas surrounding square boxes (25 μm). The magnified images of the AuNPs inside the boxes and in the peripheral area are shown in the images (B) and (C). The images in the rows (II) and (III) show the dewetted morphologies at the initial and final stages on the substrates shown in the row (I).

In comparison, the less lyophilic grid area was populated with AuNPs of relatively larger size (∼100 nm) and spacing (∼100 nm). The AFM images in the row (I) shows the typical AuNP distributions on the boxes and at the periphery of the boxes. Interestingly, when a very thin PS film was dewetted on this substrate with physicochemical patterns we could see holes of different size and spacing at the initial stages of the dewetting on

the boxes with densely populated smaller AuNPs and at the sparsely populated larger AuNPs at the periphery of the boxed areas, as shown by the images in the row (II). The images in the row (III) show the dewetted morphologies at the final stages on the substrates shown in the row (I), which suggests the formation of droplets of two different sizes on the boxes with sparsely populated larger AuNPs and more densely populated smaller AuNPs.

2.5 Summary

In this study, a self-organized instability of ultrathin (< 20 nm) PS films was explored by using underlined physicochemical heterogeneity created by AuNPs deposited on PDMS substrates. The summary of the study is,

(i) Initially, AuNPs were deposited on PDMS surface in the following way. First, PDMS surface was activated by treating them in UVO plasma treatment for different time durations. After that, activated PDMS surface was treated with 5% (v/v) 3-APTES solution for 40 min by immersing the substrates in solution. Following this, the silanized substrates were treated with AuNPs solution.

(ii) AuNPs solution was prepared by adding the 50 mM of gold chloride solution in HCl to the 50 mM of $NaBH_4$ in NaOH solution.

(iii) With increasing the UVO exposure time from 5 – 20 min, AuNPs diameter was also controlled from 25 – 150 nm.

(iv) Later, PS thin ($\sim$13.1 $\pm$ 0.1 nm) films were coated on to this substrates by ensuring that conformal adhesion.

(v) Physicochemical heterogeneity created by AuNPs could guide the hole formation of initial stage dewetting and caused tenfold miniaturization in final stage drop diameter (D_d) and spacing (S_d) when it is compared to dewettting on homogeneous PDMS substrates.

(vi) Interestingly, when the size of the AuNPs were too small (e.g. 25 nm) or too large (e.g. 150 nm) the extent of miniaturization was not that significant. Whereas,

when the size of the AuNPs were rather intermediate (e.g. 75 nm) we could observe the extent of miniaturization was largest, $S_H = 500$ nm, $D_d = 500$ nm and $S_d = 1.3$ μm.

(vii) The experiments suggested that for the physicochemical surfaces an optimal spacing and size of the AuNPs were necessary in order to shift the length scale from a few micrometers to the level of sub-micron.

(viii) Further, randomly placed dewetted structures could be ordered by creating prepatterned physicochemical substrate. For this purpose, TEM grid was placed on PDMS surface and exposed to UVO to create periodic lyophilic "boxs" and lyophobic "grids".

(ix) Interestingly, the dewetted PS structures were not only ordered but also densely populated smaller structures on the "box" patterns and sparsely populated bigger structures on the "grid" structures were formed.

2.6 Acknowledgments

The help during the experiments from Ms. Abhijna Das and Mr. Amit Kumar Singh are gratefully acknowledged.

Chapter 3

Solvent Vapour Mediated Spontaneous Healing of Self-Organized Defects of Liquid Crystal Films

3.1 Abstract

Ultrathin LC films showed a NI transition when exposed to solvent vapour for a short duration while a reverse IN transition was observed when the film was isolated from the solvent exposure. The phase transitions were associated with the appearance and fading of surface patterns as the solvent molecules diffused into and out of the film matrix, resulting in the destruction or restoration of the orientational order. A long-time solvent vapour exposure caused the dewetting of the film on the surface, which was demonstrated by the formation of holes and their growth in size with the progress of time. Even at this stage, withdrawal of the solvent exposure produced an array of nematic fingers, which nearly self-healed the dewetted holes. The change in contact angle due to the phase transition coupled with the imbalance of osmotic pressure across the contact line due to the differential rate of solvent evaporation from the film and the hole helped the fingers to grow towards the centre of the hole. The appearance of the fingers upon withdrawal of the solvent exposure and their disappearance upon exposure to solvent were also found to be a nearly reversible process. These findings could significantly contribute to the development of vapour sensors and self-healing surfaces using liquid crystal thin films.

3.2 Introduction

In the present work, we show room temperature NI and IN phase transitions in thin LC films after periodic solvent vapour exposure and withdrawal. Similar to the thermal annealing route [160], the solvent vapour induced NI and IN transitions were marked by the appearance and fading of surface undulations. The transitions were found to be a quasi-reversible process as the cycles of the NI and IN transitions could be performed repeatedly through periodic solvent exposure and withdrawal. The experiments conformed that in LC films, solvent exposure could act as an analogue to thermal annealing in ambient conditions. Importantly, a long-time solvent exposure beyond the NI transition led to the dewetting of the film with the appearance and growth of holes. Remarkably, at this stage, withdrawal of the solvent exposure produced an array of branched nematic fingers, which nearly self-healed the dewetted zones. Even at this stage, the formation of the nematic fingers upon withdrawal of the solvent contact and disappearance of the nematic fingers through solvent annealing were found to have quasi-reversible characteristics, as these events could be performed periodically for many cycles.

3.3 Experimental Section

In the experiments, 5CB nematic LC (99.99% pure, Sigma Aldrich, $T_P = \sim 33.5 \pm 0.5°C$) was used without any further processing. The films were spin-coated from a solution of 5CB, either in toluene or in hexane (HPLC grade, Merck) on square ($\sim$1 cm $\times$ $\sim$1 cm) and thoroughly cleaned pieces of Si wafer (<100> Orientation, Boron doped P type, resistivity 0.01 – 0.02 Ω cm). The coated samples were kept under vacuum at ambient conditions (24 $\pm$ 1.0°C) for about 15 min to remove any excess residual solvent. The 5CB film is nematic at room temperature, 24 $\pm$ 1.0°C, although it can show the isotropic liquid with an increase in temperature beyond T_P $\sim$33.5 $\pm$ 0.5°C. The dipole moment associated with the –CN group of the 5CB molecules enables them to form dimers in the bulk of the film of length 25 Å with their polar head facing each other while the length of a single 5CB molecule is 18.7 Å [119, 145, 177]. On a thoroughly cleaned Si wafer with a few nanometers of native oxide layer, the 5CB molecules show a planar or quasi-planar

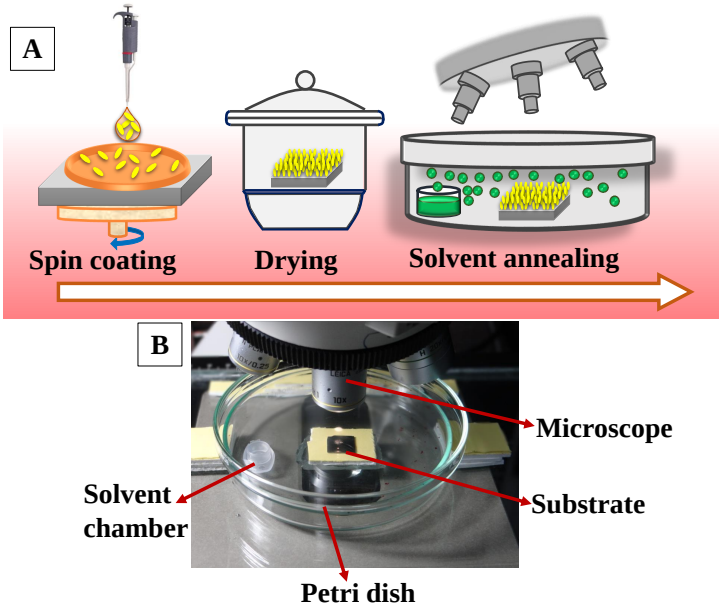

Figure 3.1: Schematic diagram (A) shows the experimental procedure for phase transition and dewetting of 5CB ultrathin films by solvent annealing. (B)In-situ experimental setup.

anchoring molecular arrangement at the Si-nematic interface [119, 121, 145, 147–150]. In comparison, the molecular arrangement is homeotropic at the nematic-air free surface [119, 121, 145, 147–150]. The 5CB completely wets a Si surface to form a film in the nematic phase while the isotropic 5CB film is only partially wettable on the Si wafer [145, 146].

The phase transition and dewetting of the 5CB films were carried out by exposing the films to solvent vapour as shown in Fig. 3.1. For this purpose, the spin-casted 5CB films were initially placed in a closed chamber with a glass cover and subsequently a container containing a fixed quantity (100 μl) of the solvent was introduced inside the chamber showed in Fig. 3.1(B). The solvent molecules diffused into the film and reduced the T_P of the nematic film to the ambient temperature. The experimental chamber was mounted on the stage of an optical microscope (Leica DM 2500M) where in situ observations were made with a CCD camera using white light in reflection mode. The rate of evaporation in the chamber could be controlled by introducing multiple solvent sources, each having a fixed volume of 100 μl. The thicknesses of the films were measured using an Imaging Ellipsometer (EP3, Nanofilm, Accurion Scientific Instruments Pvt. Ltd.). Fig. 3.2(A) shows the variations of film thickness (h) with the concentration of 5CB in the two solvents.The average rate of evaporation of the solvent vapour in

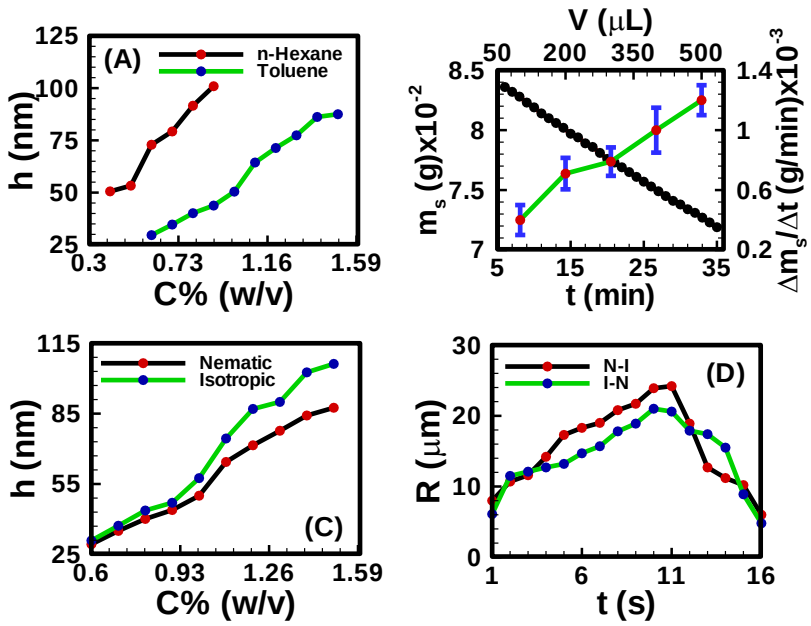

Figure 3.2: (A) Change in film thickness (h) after spin-coating with concentration (C in % w/v) of 5CB in different solvents. (B)The circular symbols denote the rate of change of mass of the solvent (m_s) with time (t-bottom y-coordinate) when the volume of the solvent (V) at the source was kept constant at 100 μl. The hollow square symbols show the rate of evaporation of solvents ($\Delta m_s/\Delta t$) with the change in the volume of the solvent (V-top y-coordinate). The joining of the data points act as a guide only. (C) Change in film thickness (h) with concentration (C in % w/v) of the nematic and isotropic films before and after the NI or IN phase transition. (D) Change in the surface roughness (R) with time during NI and IN transitions for a film of thickness, $h = 53.3 \pm 0.2$ nm.

the chamber was measured by performing a control experiment on a microbalance and calculating the ratio of the mass evaporated (Δm_s) over a specific amount of time (Δt). Fig. 3.2(B) shows the rate of evaporation ($\Delta m_s/\Delta t$) from the sources. Fig. 3.2(C) compares the thickness of the films having a homogeneous surface before and after the NI or IN transitions. The figure suggests that the film swelled during the NI transition due to the diffusive penetration of solvent molecules into the film matrix. Based on the elipsometric measurement of roughness, Fig. 3.2(D) shows that the surface roughness reached a maximum value during the NI phase transition, before dropping to a very low value after the phase transition was complete. The figure also confirms that the film did not dewet during the phase transition because the amplitudes of the undulations were much lower than the initial thickness of the film. The variation in roughness of the films (R) during NI and IN transitions were quantified using the roughness tool from the ellipsometric images.

The wavelength (λ) of the instability features were obtained from the image analysis of

the optical micrographs using the open source software ImageJ. Initially the micrograph was loaded and the image was converted to the 8-bit format. Following this, the pixels were calibrated with a scale bar. In order to obtain the average spacing of the patterns the 'analyze/plot profile' option of the software was used for a selected area or length. The reciprocal of the number of cycles appeared per unit length was reported as the average spacing between the structures.

3.4 Results and Discussion

3.4.1 Solvent Induced Phase Transitions

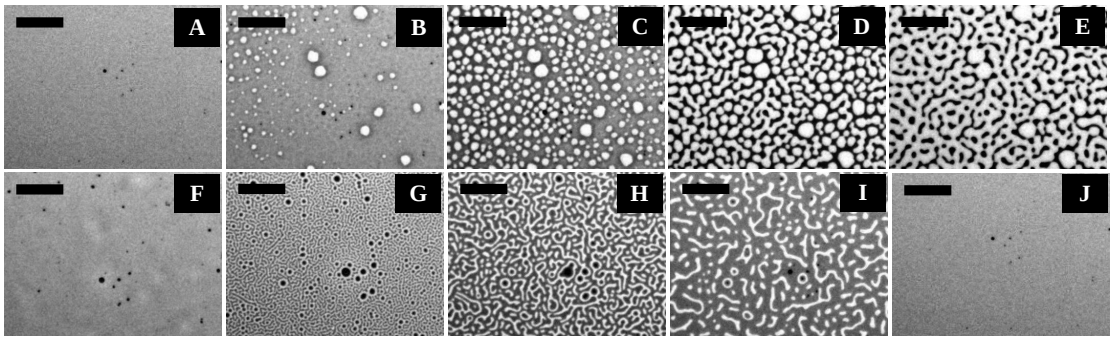

Figure 3.3: Optical micrographs of solvent vapour induced phase transitions observed in a 5CB nematic film with $h = 43.8 \pm 0.9$ nm at ambient temperature ($T = 24 \pm 1.0$°C). Images (A – F) show the evolution during the NI transition in the time intervals $t = 0$ s (time marginally before the lighter spots started appearing), 1 s, 4 s, 10 s, 13 s, and 19 s, respectively. Images (F – J) show the morphology of the film surface during the IN transition in the time intervals $t = 0$ s (time marginally before the darker spots started appearing), 1 s, 8 s, 23 s, and 26 s, respectively. The lighter shades of grey depict the thinner zones and the scale bars are 100 μm.

Fig. 3.3 shows a cycle of the forward NI phase transition upon solvent vapour annealing (images A – F) and the reverse IN phase transition upon removal of the solvent exposure (images F – J). Figs. 3.3(A) and 3.3(B) show that the initially flat surface of the nematic film deformed and that circular spots appeared due to the adsorption of the solvent molecules when the solvent source was introduced into the experimental chamber, respectively. The spots grew with time as more solvent molecules penetrated into the film surface (Fig. 3.3(C)) and subsequently, the circular spots expanded and coalesced to form bi-continuous structures (Fig. 3.3(D)). It may be noted here that, in the experimental chamber, the solvent vapour source was introduced from one of the sides of the sample, which caused the solvent vapour to diffuse across the sample from

the side where the source was placed to the other side. Thus, as time progressed, the solvent diffused from left to right. Further, the time $t = 0$ s reported in the figure caption represents the frame marginally before the first spot of solvent nucleated on the film. The accumulation of the solvent molecules on the surface and their subsequent diffusion into the bulk of the film resulted in the gradual destruction of the nematic orientational order of the LC molecules, leading to the NI transition. The completion of the NI transition was demonstrated by the disappearance of the surface features, resulting in a flat isotropic film (Fig. 3.3(F)). Figs. 3.3(F) and 3.3(G) represent a sequence where the solvent vapour sources were removed from the film chamber following the NI transition. This triggered a reverse IN transition, as shown in the Figs. 3.3(F – J). The removal of the solvent exposure led to an outward diffusion of the solvent molecules from the film matrix to the surroundings. Consequently, the extent of swelling of the film reduced, which in turn restored the nematic ordering within the film, resulting in the IN phase transformation. This backward IN transition was also associated with the appearance and fading of an intermediate surface roughness. Fig. 3.3(J) shows a nearly flat nematic thin film after completion of the IN transition. Interestingly, the NI and IN transitions upon periodic exposure and removal of the solvent were found to be a quasi-reversible process as the cycle could be repeated for several times, which was observed in the case of thermal annealing [160].

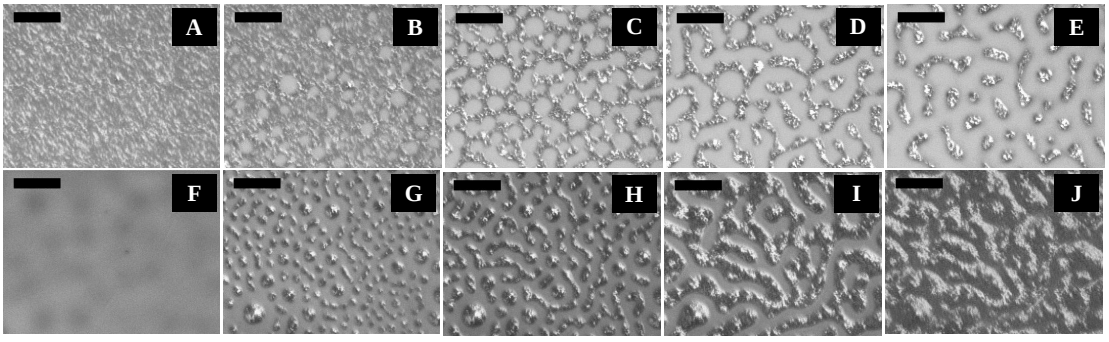

Figure 3.4: Polarization microscopic images (crossed polarizers) of solvent vapour induced phase transitions observed in a 5CB nematic film with $h = 47.4 \pm 1.2$ nm at ambient temperature ($T = 24 \pm 1.0°$C). Images (A – E) show the spatiotemporal evolution during the NI transition in the time intervals $t = 0$ s, 5 s, 11 s, 17 s, and 24 s, respectively. Images (E – J) show the morphology of the film surface during the IN transition in the time intervals $t = 0$ s, 5 s, 6 s, 10 s, 14 s, and 26 s, respectively. The lighter shades of grey depict the thinner zones and the scale bars are 50 μm.

The polarizing microscope Figs. 3.4(A – E) confirm that the surface texture of the

nematic film progressively disappeared during the NI phase transition, as the solvent molecules started aggregating on the film surface. The Figs. 3.4(A – E) confirm that the lighter circular spots in the Figs. 3.4(A – E) were indeed the local nucleation of the solvent molecules. The floating solvent molecules near the nematic-air interface enforced a grey rather than black colouration to the isotropic phase under polarization microscopy. The Figs. 3.4(F – J) show that the surface texture of the nematic film was progressively restored when the solvent vapour source was removed from the chamber and the IN phase transition took place as the solvent molecules evaporated out of the film matrix. The Figs. 3.4(F – J) confirm that the dark spots in the Figs. 3.4(F – J) were the reappearance of the nematic phase as the solvent molecules evaporated out of the film matrix.

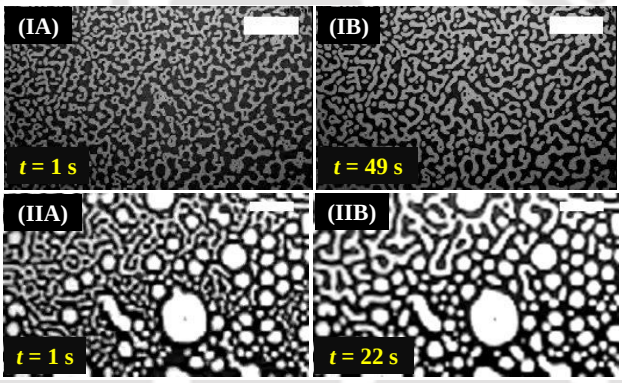

Figure 3.5: Images of row (I and II) show the mechanical and chemical equilibrium of 5CB phase transition patterns for thickness 47.3 ± 1.2 nm and 64.4 ± 0.55 nm, respectively. The scale bars are 50 μm in all the frames.

It may be noted here that, during the NI transition, when the solvent molecules adsorbed on the surface and progressively diffused into the film, the system was always away from equilibrium due to the difference in chemical potential inside the film. However, a long-time exposure of the solvent on the film helped in reaching equilibrium at the isotropic state, after the film surface became homogeneous. Similarly, for the IN transition the film was again out of equilibrium when the solvent molecules started evaporating from the film matrix. A long-time evaporation of the solvent molecules from the film led to a nematic film with a flat surface under equilibrium conditions. Importantly, when a nematic film was annealed through solvent vapour exposure to its phase transition point, the system tried to achieve two different types of equilibrium. While the coexistence of

the solvent molecules with the nematic and isotropic phases created a difference in chemical potential across the film, the molecular rearrangements due to the elastic (viscous) response of the nematic (isotropic) phase tried to establish a mechanical equilibrium inside the film. A few previous works [121, 155] on the thermal annealing of nematic films have shown that thermal and mechanical equilibriums could be attained during phase transitions when the temperature was kept constantly near T_P. These studies showed that if the temperature (T) was kept constant ($T_U > T > T_L$) amid the upper (T_U) and lower (T_L) bound of temperatures between which the patterns appeared and disappeared on the surface of the film, a thermal as well as a mechanical equilibrium could be attained. In such a situation, the patterns that appeared during the phase transition could be retained for a longer duration. In order to understand the typical experimental time scales for the chemical and mechanical equilibriums for the system under consideration, we performed similar experiments keeping the partial pressure of the solvent vapour nearly constant. The partial pressure on the film was maintained at a constant value by manually adjusting the loss of vapour through the experimental chamber with respect to the amount of solvent evaporated from the source. Fig. 3.5 show the morphological evolution of nematic films with two different film thicknesses ($h = 47.3 \pm 1.2$ nm and $h = 64.4 \pm 0.55$ nm) when the partial pressure of the solvent vapour surrounding it was kept nearly constant. The images suggest that the patterns that appeared during phase transition could be retained for a longer duration when the partial pressure was nearly constant. Further, the characteristic time for the molecular rearrangement to attain the mechanical equilibrium was observed to be rather larger for the thinner film. In comparison, for the thicker film, the evolution to attain the mechanical equilibrium was observed to be much faster. Remarkably again, thermal and solvent vapour annealing showed very similar behaviours in this regard.

Fig. 3.6(A) shows the variation of the average periodicity of the surface features (λ) with time (t) during the NI and IN transitions for the film shown in Fig. 3.3 (film thickness $h = 43.8 \pm 0.9$ nm). It may be noted here that the time $t = 0$ s represents the frame when the initial lighter spots of the solvent molecules nucleated on the film. During the initial stages of the NI transition λ decreased with the progressive increase in the number of solvent molecules adsorbed on the film-surface. The trend continued until the surface

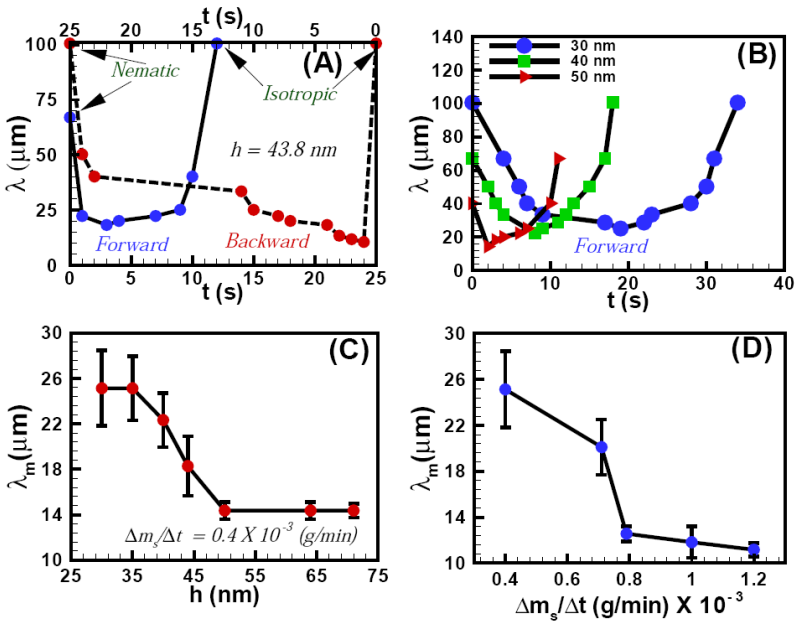

Figure 3.6: (A) Variations of average λ with t for a forward NI (time marked in the bottom x-axis) and a backward IN (time marked in the top x-axis) cycle when $h = 43.8 \pm 0.9$ nm. (B) Variations of λ with t for different h. (C) Variation of λ_m with h at a fixed evaporation rate ($\Delta m_s/\Delta t$). (D) Variation of λ_m with changes of $\Delta m_s/\Delta t$ when $h = 29.6 \pm 0.6$ nm. The results shown in the frames (B – D) are for the forward NI transition.

was nearly saturated with the solvent molecules and λ attained a minimum value (λ_m). Beyond this point the features progressively disappeared (increase in λ) as the solvent molecules gradually diffused into the film matrix and the film became isotropic. The IN transition upon removing solvent vapour exposure was also initiated with a reduction in λ until a minimum was attained, which demonstrated the outward diffusion of the solvent molecules from the film matrix. As the solvent molecules completely diffused out of the film, λ increased until a nearly flat nematic film surface emerged. The plot also highlights the existence of some hysteresis in terms of λ and t between the forward (NI) and the backward (IN) transitions, due to the differential rates of solvent intake on the film surface and diffusion of the solvent molecules within the film surface. Fig. 3.6(B) shows the variation of λ with t during the forward NI transition at different values of h. The figure suggests that the transition took less time with increasing h. The observation was somewhat counter intuitive because the solvent molecules would require longer time to diffuse deeper into a thicker film to cause the NI transition. The possible reason could be that the order of the LC molecules at the free-surface is less (more) constrained in a thicker (thinner) film because of their larger (smaller) distance from the strongly anchored LC molecules on the substrate [177]. Previous studies demonstrated

that the 5CB molecules form dimers in the bulk of the film [119, 145, 147], while at the nematic-substrate (nematic-air) interface the 5CB molecules show a planar (homeotropic) orientation [119, 121, 145, 147–150]. Thus, a less (more) constrained nematic-air interface allowed faster (slower) kinetics of the NI phase transition or vice versa for the thicker (thinner) films. Fig. 3.5 also demonstrate that the molecular rearrangements could be much faster for the thicker films, which could also speed up the kinetics of the process. We further investigated the variation of λ_m with h, which is shown in Fig. 3.6(C). The plots suggest that for $h < 50$ nm, λ_m progressively decreased with increasing h. However, λ_m became nearly independent of h for thicker films ($h > 50$ nm). These observations suggest that beyond $h_c \sim 50$ nm the number density of the nucleation sites for the solvent molecules on the film surface become independent of h. The rate of solvent vapour evaporation ($\Delta m_s/\Delta t$) into the experimental chamber also influenced λ_m. Fig. 3.6(D) shows that λ_m progressively decreased with an increasing rate of solvent evaporation from the source, which led to a faster penetration of the solvent molecules inside the film. This particular aspect of the solvent vapour annealing of LC films was also similar to the thermal annealing of LC films where λ_m is known to change with the rate of heating [160].

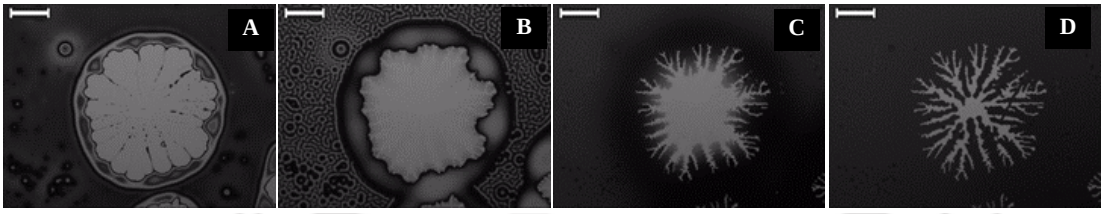

Figure 3.7: (A) Formation of a nucleated hole upon solvent vapour exposure for 697 s for a nematic film of $h = 72.9 \pm 0.2$ nm. (B – D) hole-healing sequence after withdrawing the film from the solvent vapour. (B) Shows the appearance of fingers along the contact line and IN transition on the bulk of the film; (C) growth of the fingers towards the hole centre, and (D) near-complete healing of the hole with branching of the primary fingers. The scale bars are 100 μm in all the frames.

Fig. 3.7 shows the dewetting and subsequent hole-healing of a nematic film upon prolonged solvent exposure beyond the stage of the NI transition and thereafter the removal of the solvent exposure. Previous studies showed that a 5CB film is completely wettable on a Si surface in the nematic phase while the isotropic 5CB film is only partially wettable on a Si wafer [145]. Fig. 3.7(A) shows that long-time (697 s) solvent exposure led to the dewetting of a 5CB film with the formation of a hole surrounded by a thick rim. The

pathway appeared identical to the thermal dewetting of a polymeric film when annealed beyond the glass transition temperature. It may be noted here that while the thermal annealing destroyed the orientational order of the LC from the bottom substrate, the solvent annealing did the same through the LC-air interface. Further, solvent vapour induced dewetting of a polymer thin film leads to permanent holes and features, which remain unaltered even after withdrawing the sample from solvent vapour exposure. In comparison, for the nematic films, the morphology of the holes was found to change when the solvent sources were withdrawn from the chamber.

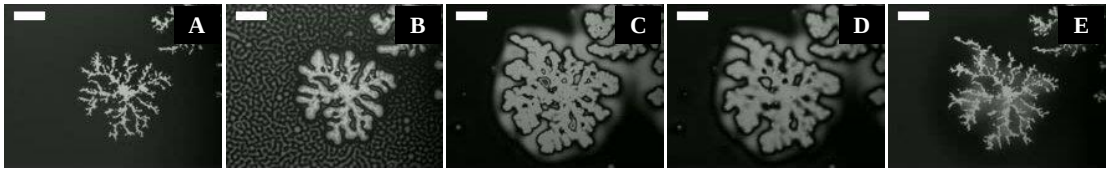

Figure 3.8: Images show the repeated cycles of self-healing of 5CB film with thickness $h = 72.9 \pm 0.2$ nm. Images (A – C) show the dewetting of self-healed hole upon the solvent exposure, images (C – D) show the reself-healing upon the withdrawal of solvent exposure. The scale bars are 100 μm in all the frames.

3.4.2 Self-Healing of Dewetted Film

Fig. 3.7(B) shows the morphology of the hole after 61 s of the solvent source withdrawal. The key features observed were: (i) contact line around the hole becomes unstable with the appearance of periodic wavy patterns; (ii) surface pattern on the film surface demonstrating an IN transition in the other part of the film, as observed previously in Fig. 3.3(G) and 3.3(H); and (iii) the drop or thread like residuals of the films start spreading on the hole. The appearance and disappearance of surface patterns implied that progressively the nematic order was restored inside the film as solvent molecules started diffusing out of the film matrix. Since the 5CB film is completely wettable on a Si surface in the nematic state [145], spreading with a change in contact angle was observed in Fig. 3.7(B) in place of the droplets or threads on the hole in Fig. 3.7(A). The evaporation across the contact line changed the contact angle as the isotropic film was progressively converted into a nematic film with time and the contact line motion towards the centre of the hole was set in. In regular circumstances, the nematic film was expected to uniformly spread on the entire hole to fully cover it. However, the differential

rate of solvent evaporation from the film, hole-rim, contact line, and dewetted zone was very closely coupled with the change in contact angle, as the isotropic film was gradually converted into a nematic film. Thus, during the IN transition, Fig. 3.7(B) and 3.7(C) show the appearance of a contact-line instability in the form of nematic fingers around the hole once the contact line motion set in. With the progress of time, the differential rate of solvent evaporation from the film, hole-rim, contact line, and hole created an imbalance of the osmotic pressure across the contact line which in conjugation with the change in contact angle stimulated the contact line motion.

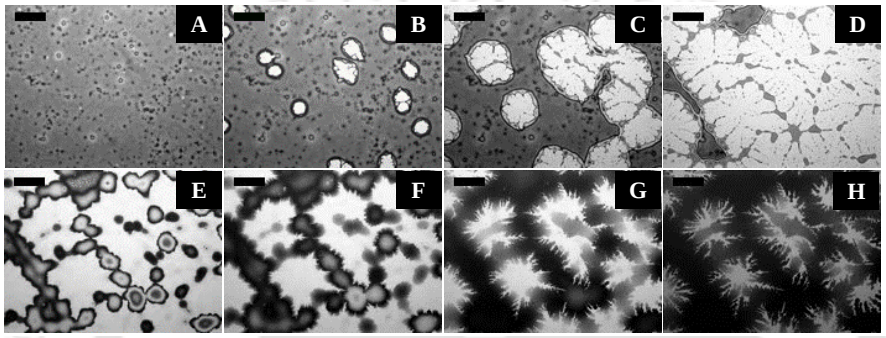

Figure 3.9: Images (A – D) show the dewetting of 5CB thin film ($h = 72.9 \pm 0.2$ nm) with multiple holes upon the solvent vapour exposure, images (E – H) show the self-healing of dewetted film upon withdrawal of solvent exposure. The scale bars are 50 μm in all the frames.

Fig. 3.7(C) (808 s after withdrawal of solvent source) and 3.7(D) (2071 s after withdrawal of solvent source) suggest that the change in contact angle and the osmotic pressure imbalance across the contact line helped the nematic fingers to grow towards the centre of the hole. Fig. 3.7(D) shows that the fingers stretched along the contact line almost all the way until the ruptured hole is nearly healed up. It may be noted here that if the solvent exposure was reintroduced at any stage of the hole-healing process, the fingers disappeared following an NI transition and the film again started dewetting the surface, which clearly emphasized the quasi-reversible nature of the solvent vapour induced dewetting of the LC thin film. The hole-healing through the nematic fingers upon removal of the solvent exposure and dewetting of the film through hole-growth upon solvent exposure could also be repeated for many cycles, which are shown in the Fig. 3.8. The Fig. 3.9 shows that when there are multiple holes on a dewetted film the fingering instability could again self-heal almost the entire dewetted zone upon removal of the solvent exposure.

Fig. 3.10 shows the kinetics of hole and finger growth during solvent vapour annealing

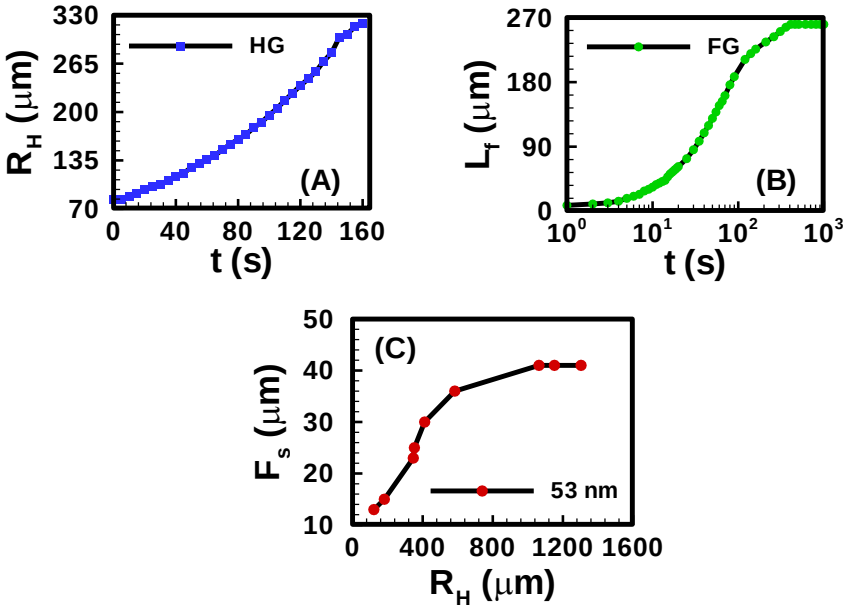

Figure 3.10: (A) The variation of the radius of a hole (R_H) with time (t) for a nematic film of $h = 72.9 \pm 0.2$ nm. (B) The variation of the length of the fingers (L_f) with time (t) for a nematic film of $h = 72.9 \pm 0.2$ nm. (C) Change in finger-spacing (F_s) when the initial hole-radius (R_H) was varied for a nematic film of $h = 53.3 \pm 0.2$ nm.

and removal of solvent vapour exposure. Fig. 3.10(A) and 3.10(B) show the variations of the hole diameter (R_H) during hole-growth and average length of the fingers (L_f) during hole-healing with time (t). The kinetics of hole-growth were observed to be much faster than the hole-healing process. The plots also suggest that the isotropic holes grew almost linearly with time during dewetting, whereas the hole-healing took place in three distinct phases. The initial slower regime corresponds to the development of the instability along the contact line while the film underwent the IN transition. The subsequent faster regime corresponds to the growth of the nematic fingers towards the hole-centre because of the change in contact angle and osmotic pressure imbalance across the contact line. Towards the end, the healing process became exceedingly sluggish because of the reduction in the driving force owing to the lack of solvent inside the film matrix and hole. Fig. 3.10(C) shows that the periodicity of the fingers (F_s) was much smaller when the hole-radius (R_H) was smaller. However, F_s initially increased and then saturated to a constant value with increasing R_H.

3.5 Summary

In this study, solvent vapour mediated phase transitions and self-healing of self-organized defects in ultrathin (< 100 nm) 5CB films were studied. The summary of the study is,

(i) Initially, spin-coated ultrathin 5CB films were annealed by solvent vapour. As a result, NI and IN phase transitions were observed with solvent exposure and withdrawal, respectively, at room temperature only. During the NI (IN) phase transition, randomly placed surface patterns were appeared on the nematic (isotropic) film surface which originated by destruction (construction) of nematic orientational order by adsorption of the solvent molecules. Following this, surface patterns grew continuously and coalesced to form bi-continuous phase by continuous penetration of solvent molecules into the film matrix. Finally, they disappeared and form a flat isotropic (nematic) film.

(ii) This NI and IN phase transitions could be repeatable as many times same as thermal annealed phase transitions.

(iii) The experiments under the cross polarized microscope conformed that the appeared pattens during NI (IN) transition were indeed isotropic (nematic) patterns by the losing (gaining) the nematic (isotropic) texture on the film surface.

(iv) While, the phase transition patterns were retained long duration by keeping the constant vapour pressure by attaining the chemical and mechanical equilibrium. For thinner films longer retention time of surface pattens were observed whereas for thicker films shorter retention time was observed.

(v) The variation of the average periodicity of the surface patterns (λ) with t was calculated during the NI and IN phase transitions. During initial stages λ decreased until a minimum value attained, later it started to increase again.

(vi) For $h < 50$ nm, λ_m progressively decreased with increasing h, however, λ_m nearly independent of h for thicker films ($h > 50$ nm).

(vii) The rate of solvent evaporation ($\Delta m_s/\Delta t$) into the experimental chamber also influenced the λ_m.

(viii) After the NI phase transition the prolonged solvent exposure led to the dewetting of a 5CB film with the formation of a random placed holes.

(ix) The hole size increased with time, however at this stage removal of solvent exposure led to self-heal the dewetted hole.

(x) During this stage, removing the solvent exposure led to an exciting fingering instability at the contact line, surrounding the dewetted zones. The change in contact angle due to phase transition coupled with the imbalance of osmotic pressure due to the differential rate of solvent evaporation across the contact line helped the fingers to grow towards the centre of the hole. The fingers grew with time to attain structures with significantly high aspect-ratio and branching patterns, which nearly self-healed the dewetted zones.

(xi) Interestingly, even at this stage, the growth of the fingers could be arrested and dewetting could be resumed by introducing solvent vapour exposure. The formation of the nematic fingers upon withdrawal of the solvent exposure and the removal of the fingers through the dewetting of the films upon solvent vapour annealing were found to be a quasi-reversible process.

3.6 Acknowledgments

The help during the experiments from Dr. Karthik Mondal is gratefully acknowledged.

Chapter 4

Pattern Directed Phase Transition of the Nematic, Smectic, and Crystal State Ultrathin Films

4.1 Abstract

A host of solvent vapour annealed phase transitions of LC films have been explored targeting various applications. While the solvent exposure led to the crystalline or semctic phases to transform into the nematic and isotropic phases, the reverse phase transitions from IN and from NS or NC phases have been observed upon the withdrawal of the solvent vapour source. The phase transitions were found to be repeatable in nature with the periodic exposure and withdrawal of the solvent exposure and were found to be very similar to the thermally annealed phase transitions. The only exception was that for the solvent vapour annealing the entire process could be carried out under the ambient conditions. Exploiting this phenomenon, emulating the principles of LC thermometers, the time required for the phase transition of a thin LC film resting on a solid substrate was correlated with the vapour pressure and volatility of different aromatic and non-aromatic solvents. The times for phase transition under different solvent exposures were found to linearly reduce with the increase in the vapour pressure and volatility of the solvents. Further, the solvent annealed phase transitions of a gold nanoparticle-5CB composite LC droplet were converted into an electrical signal with the help of a simple external circuit. The experiments showed that the electrical resistance reduced (increased) upon the destruction (restoration) of the orientational order of the

droplet. The electrical responses could be employed to sense the presence and absence of different volatile organic vapours, phase transition of LC materials, evaluation of the order parameter of an LC material during phase transition, rate of diffusion and absorption of a solvent into an LC matrix, and the rate of desorption and evaporation of a solvent from an LC matrix. Finally, the solvent annealed phase transition of the LC materials on the physically and chemically heterogeneous surfaces shows a pattern directed phase transition. While in the physically heterogeneous surface, the variations in the thicknesses ensured that the NI phase transition was faster (slower) at the thinner (thicker) regimes and in the chemically heterogeneous surfaces the weaker (stronger) anchoring of the LC molecules on the lyophobic (lyophilic) patches ensured a faster (slower) due to less (more) solvent was required in both to destroy molecular orientation during the solvent vapour exposure. The reported phenomena could easily be exploited to develop LC based devices to identify the physical or chemical defects on the surfaces alongside the measurement of the extent of lyophobicity or lyophilicity of the surfaces.

4.2 Introduction

In the present study, initially, solvent vapour mediated phase transitions of a number of different smectic and nematic LC materials have been explored. Following this, the roles of different aromatic and non-aromatic solvents having different vapour pressure and volatility on the phase transition of a nematic film have been studied. Based on these findings, we show that the solvent vapour mediated phase transitions of LC films can easily be exploited to develop electrical sensors, which can differentiate different volatile organic vapours and measure their vapour pressure and volatility. Further, we show that indeed the presence of a physical or chemical defects can lead to a pattern directed phase transition when an LC film with a free surface underwent solvent vapour annealing. We found that the zones with thinner (thicker) films and lyophobic (lyophilic) patches are expected to show a faster (slower) NI transition. Interestingly, although the thinner (thicker) films show faster (slower) IN transition, the chemically lyophobic (lyophilic) patch on the contrary exhibits slower (faster) IN transition. Remarkably, these experiments uncover that the random small amplitude free surface undulation, observed during

the NI and IN transitions, become pattern directed following the underlying periodic topographical or chemical patterns. DSC analysis confirms the presence of hysteresis in phase transition during heating (NI transition) and cooling (IN transition) of liquid crystal [178]. In the present study we will show that due to dissimilar rate of absorption and desorption of the solvent molecule in the liquid crystal matrix, similar hysteresis in phase transition may exists in solvent mediated annealing of the LC film. The findings of this study can be of significance in the development of futuristic physical or chemical defect detectors, organic vapour sensors, chemically or physically patterned mesoscale cross polarizers for various display applications.

4.3 Experimental Section

4.3.1 Materials

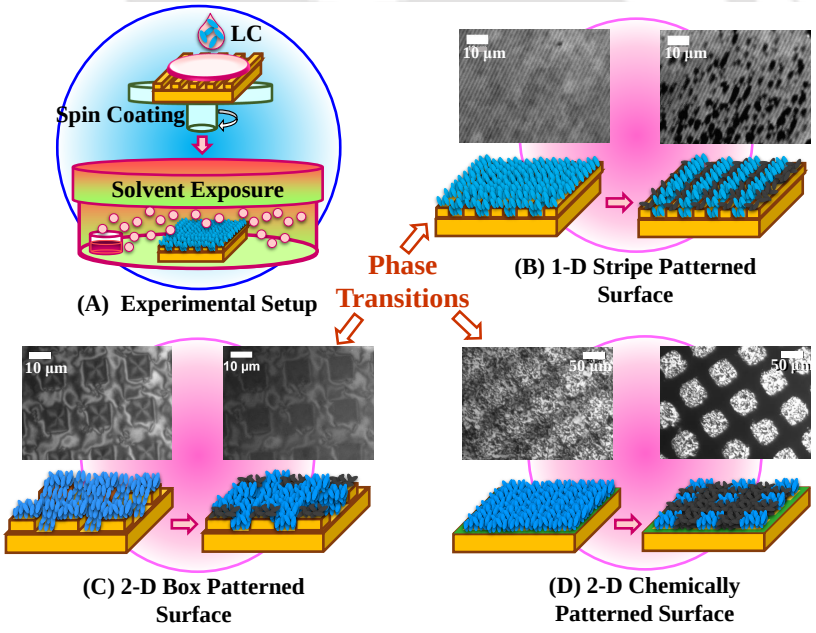

Figure 4.1: Image (A) schematically shows the experimental setup for the solvent vapour mediated phase transition of 5CB film on a patterned surface. Image (B) shows the directed phase transition on a topographic stripe patterned PS substrate with 800 nm width, 120 nm height, and 1600 nm periodicity. Image (C) shows the directed phase transition on a topographic box patterned PS substrate with 10 μm width, 300 nm height, and 20 μm periodicity. Image (D) shows the directed phase transition on a chemical box patterned silicon substrates with OTS patches of hole width, pitch, and bar width, 58 μm, 83 μm, and 25 μm, respectively. The cross-polarized optical micrographs show the typical phase transitions of the film on the substrates shown in the image (B), (C), and (D). In these images, the darker (gray) shades show the isotropic phase and lighter (blue) shades show the LC phase.

Si (<100> Orientation, Boron doped P type, resistivity 0.01 – 0.02 Ω cm) and quartz substrates were purchased from N. J. Int. Cop. and Macwin, India. Various LC materials (99.999% purity) such as 5CB, 7CB, and 8CB were purchased from Sigma-Aldrich, India. The NI phase transition temperature for 5CB is ∼33.5 ± 0.5°C, for 7CB the phase transition temperatures for CN and NI are 29°C and 42.4°C, and for the 8CB the phase transition temperatures for CS, SN, and NI are 22.5°C, 32°C – 34°C, and 41°C, respectively [179]. The phase transitions of the LC films were studied with various non-aromatic and aromatic solvents such as acetophenone, benzyl chloride, styrene, 1,2-xylene, toluene, benzene, hexane, acetone, and chloroform which were purchased from Sigma-Aldrich and Merck, India.

In order to prepare the master stamp for the physical patterns, PDMS was procured from Dow Corning, Mumbai, India (SYLGARD® 184 kit) while the substrate material PS (Mw = 280,000 g/mol) was procured from Sigma-Aldrich and Merck, India. The OTS was obtained from Sigma-Aldrich, India while the TEM grids with 300 mesh (lines/inch) were procured from SPI supplies, USA, which had hole width, pitch, and bar width of 58 μm, 83 μm, and 25 μm, respectively. For sensor experiments the LC was dispersed with dodecanethiol functionalized gold nanoparticles (DAuNPs) in toluene at a 2% (w/v) to improve the conductivity. The chemicals required for nanoparticle synthesis and functionalization such as hydrogen tetrachloroaurate ($HAuCl_4 \cdot 4\,H_2O$), tetraoctylammonium bromide (TOAB), dodecanethiol, and sodium borohydride ($NaBH_4$) were procured from Sigma-Aldrich, India.

4.3.2 Methods

4.3.2.1 Phase Transition Experiments

All the solvent annealed phase transition experiments were done under ambient conditions near 24 ± 1°C and 1 atm pressure. Image (A) in the Fig. 4.1 schematically show the experimental setup employed for the study. For this purpose, initially 0.4 – 1% (w/v) concentrations of 5CB, 7CB, and 8CB were prepared in hexane solvent. They were spin-coated on Si substrate followed by vacuum drying 15 min to remove excess solvent. Under the ambient condition (24 ± 1°C and 1 atm pressure) the 7CB and 8CB

were in crystalline and smectic state respectively. The LC film coated substrates were kept in petri dish along with solvent chamber with 200 μl of hexane solvent, as shown in Fig. 4.1. When the petri dish lid was closed volatile solvent diffused into the film matrix to cause the NI phase transition for 5CB, CNI phase transitions for 7CB, and SNI phase transitions for 8CB. As soon as these phase transitions were completed the lid was opened to isolate the substrates from solvent exposure. Subsequently, the volatile solvent vapour diffused out of the film matrix to cause IN phase transition for 5CB, INC for 7CB, and INS for 8CB. The experiments were followed under optical microscope (Leica DM 2500M) and phase transitions were recorded by CCD camera using white light in reflection mode.

For the experiments with different solvent vapours, initially, a 5CB solution was prepared in hexane solvent with different concentrations from 0.4 – 1% (w/v). Following this, a 5CB nematic film was spin-coated on Si substrates and dried in under vacuum at 24 ± 1°C for 15 min. Thereafter, separate 5CB films were exposed to various non-aromatic (e.g. hexane, chloroform, acetone) and aromatic (e.g. acetophenone, benzyl chloride, styrene, 1,2-xylene, toluene, benzene) solvents and the time for the phase transition after the solvent exposure noted.

4.3.2.2 Preparation of Patterned Surfaces

After the cutting and cleaning of Si substrates following standard protocol, 5% (w/v) concentration of PS in toluene spin-coated at 2500 rpm and 120 s duration. The films were dried in vacuum oven at 60°C for 24 h to remove the excess solvent. The stripe patterned PDMS master stamp was prepared previously by pouring PDMS on compact disk [180]. A small size of the stamp was cut and immersed in toluene for 30 s before placing on the PS film for 2 min. Thereafter, in order to transfer the PDMS patterns, the PS film was annealed through the solvent vapour exposure. For this reason, the PS film with the PDMS stamp on the top was kept in a petri dish for 2 – 3 min along with 8 – 10 solvent chambers filled with solvent toluene. Under this condition, the PS film developed negative replica of PDMS master due to capillary force lithography (CFL) [181]. Following this, after 2 – 3 min of solvent exposure the PS film was isolated and

dried in ambient condition. The surface patterns were analysed by atomic force microscopy (AFM, Innova Iris, Bruker-Icon Analytical Equipment). The dimensions of the stripes on the PS surface were 800 nm width, 120 nm deep, and periodicity of 1600 nm, as shown in the Fig. 4.1(B).

The box patterned PS surface with 10 μm width, 20 μm periodicity and 300 nm depth, shown in the Fig. 4.1(C), was fabricated by a modified pressure assisted imprinting technique, the details of which can be found elsewhere [58]. In order to prepare the chemically patterned surface, initially, an OTS monolayer was deposited on the thoroughly cleaned Si wafers by immersing them in OTS solution (5 μl OTS in 5 ml bicyclohexane) for 20 min. Following this, the substrates were sonicated in chloroform for 20 min then dried in the stream of N_2 [182]. Thereafter, the OTS coated Si substrates were masked by a TEM grid before exposed to UVO (PSDP-UV4, Novascan Tech. Inc., USA) for 2 h. The UVO passed through the "box" openings of the TEM grid to etch out the OTS layer while under the Cu the OTS film remained as it was coated. Thus, after UVO treatment led to the formation of Si/SiO_2 "box" patterns and OTS "grid" patterns on the Si wafer, as shown in the Fig. 4.1(D). In order to study the pattern directed phase transition, the 5CB films (2 – 40% w/v in hexane) were initially spin-coated on the surfaces with physical and chemical patterns, as shown Fig. 4.1. The thicker films are coated to avoid the issues associated with the spin-dewetting for the thinner films. Following this, the solvent vapour experiments were conducted as mentioned previously.

4.3.2.3 Vapour Sensor

For this experiment, initially, the electrical conductivity of 5CB was increased by mixing it with the DAuNP. In order to synthesize DAuNP, initially 30 ml, 0.03 M of an aqueous solution of $HAuCl_4$ was mixed with 80 ml, 0.05 M of TOAB in toluene. The two-phase mixture was stirred vigorously until all the $HAucl_4$ was transferred into the organic layer before 170 mg dodecanethiol was added to the organic phase. Thereafter, 25 ml, 0.4 M of a freshly prepared aqueous solution of $NaBH_4$ was added slowly into the previous system with vigorous stirring for 3 h and evaporate the organic phase in a rotary evaporator. Then the solution was mixed with 400 ml ethanol to remove excess thiol. The mixture was kept at -18°C for 4 h before a dark brown precipitate was obtained, which was

filtered and washed with ethanol. A 2% (w/v) of DAuNP composite was prepared by dissolving adequate amount of the precipitate in 10 ml of toluene. After this, 2%DAuNP and LC were mixed (100:15) to prepare a 5CB-DAuNP composite solution [183]. The amount of DAuNP was kept deliberately high to decrease the 5CB electrical resistance within the multimeter range from > 200 to 30 MΩ. A 10 μl droplet of this mixture was placed at the junction of a pair of electrodes, which was a part of the circuit designed to measure the electrical response of the droplet. The circuit was a pair of Cu electrodes on a PDMS substrate in which the ends of electrodes were connected with a digital multimeter (MASTECH-M92A) to measure change in electrical resistance. Thereafter, with the help of 20 solvent chambers of size 200 μl, various non-aromatic and aromatic solvents were introduced into the petri dish to study change in electrical resistance during the NI phase transition of the 5CB-DAuNP composite microdroplet. The NI transition with the exposure of solvent vapour led to the reduction in the electrical resistance while the removal of the solvent exposure led to an increase in the electrical resistance across the microdroplet due to the IN transition.

4.4 Results and Discussion

4.4.1 Solvent Mediated Phase Transitions of LC

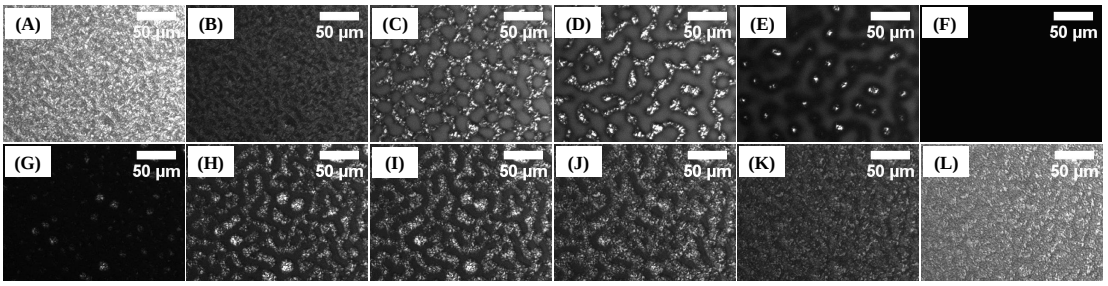

Figure 4.2: Cross-polarized optical micrographs of the solvent vapour induced phase transition of 51 ± 1.0 nm thick 7CB film at ambient temperature ($T = 24 \pm 1$°C). Images (A) and (L) show the initial and final crystal states of the film. Images (A – F) show the CNI phase transitions at time intervals $t = 0$ s, 93 s, 99 s, 102 s, 105 s, and 116 s, respectively, after the solvent exposure was introduced. Images (F – L) show the reverse INC phase transitions at the time intervals $t = 0$ s, 43 s, 45 s, 49 s, 56 s, and 63 s, respectively, after the solvent exposure was withdrawn.

In this section, we show diverse phase transition behaviours of a set of LC films due to solvent annealing. Although this subject has been explored in detail for thermal annealing [143, 151, 155, 156, 158, 184–192], there is hardly any study, which shows the effects of various types of solvent vapour exposures in this regard. The cross-polarized optical micrographs in the Fig. 4.2 shows that the solvent annealing could indeed engender CNI phase transitions of a 7CB film under ambient condition. The Figs. 4.2(A) and 4.2(B) show that the transition from CN state with the solvent exposure while the Figs. 4.2(B – F) show that the NI phase transition. The progressive destruction of the textured director orientation having brighter zones at the film surface could easily be followed under the cross-polarizer. Figs. 4.2(F – L) show that the process was nearly reversible as the nematic and crystal textures with brighter patches at the surface was recovered with the withdrawal of the solvent exposure.

Fig. 4.2 show a simple way to progressively destroy the crystalline and nematic orientational orders of the 7CB films with solvent vapour annealing. The Figs. 4.2(C – E) show the appearance and progressive expansion of the darker grey spots, which indicated the formation of the isotropic zones with the gradual adsorption and penetration of the solvent molecules into the film matrix. Consequently, with time, the orientational order of the LC film was lost to reach the isotropic state with a non-textures surface, as shown in the Fig. 4.2(F). However, the withdrawal of the solvent vapour source led to the progressive desorption and evaporation of the solvent molecules from the film matrix, as shown in the Figs. 4.2(G – J). The CNI and INC cycles shown in the figure could be repeated for as many times with the solvent vapour exposure and its withdrawal, as it is in general observed for the thermally annealed cases where the temperature has to be modulated near T_P for this behaviour.

Fig. 4.3 shows another example where smectic and nematic orientational orders of the 8CB film was progressively destroyed with the help of solvent vapour annealing. The Figs. 4.3(A) and 4.3(B) show that the transition from SN state while the Figs. 4.3(B – E) show that the NI phase transition. Again, the Figs. 4.3(E – H) show that the process was nearly reversible as the nematic and smectic textures at the surface was recovered with the withdrawal of the solvent exposure. The Figs. 4.3(B – E) show the appearance and progressive expansion of the grey spots, which indicated the gradual adsorption and

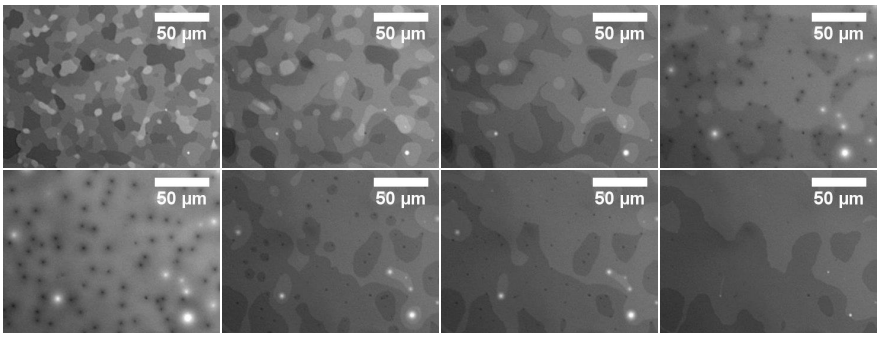

Figure 4.3: Cross-polarized optical micrographs of the solvent vapour induced phase transition of 54 ± 1.0 nm thick 8CB film at ambient temperature ($T = 24 \pm 1°C$). Initially the film was at smectic G state having a mosaic surface texture, as shown in the image (A). Images (A – E) show the SNI phase transitions at the time intervals $t = 0$ s, 36 s, 41 s, 59 s, and 75 s, respectively, after the solvent vapour exposure was introduced. Images (E – H) show the reverse INS phase transition at the time intervals $t = 0$ s, 14 s, 17 s, and 38 s, respectively, after the solvent vapour exposure was withdrawn.

penetration of the solvent molecules into the film matrix. The LC film attained the isotropic state in the Fig. 4.3(E).

Again, in this situation, withdrawal of the solvent vapour source led to the progressive desorption and evaporation of the solvent molecules from the film matrix to restore the semctic order in the Fig. 4.3(H). Like in the previous example, the SNI and INS cycles in the present care could be repeated for as many times with the solvent vapour exposure and its removal, as observed for the thermally annealed cases where the temperature is modulated near T_P for this behaviour.

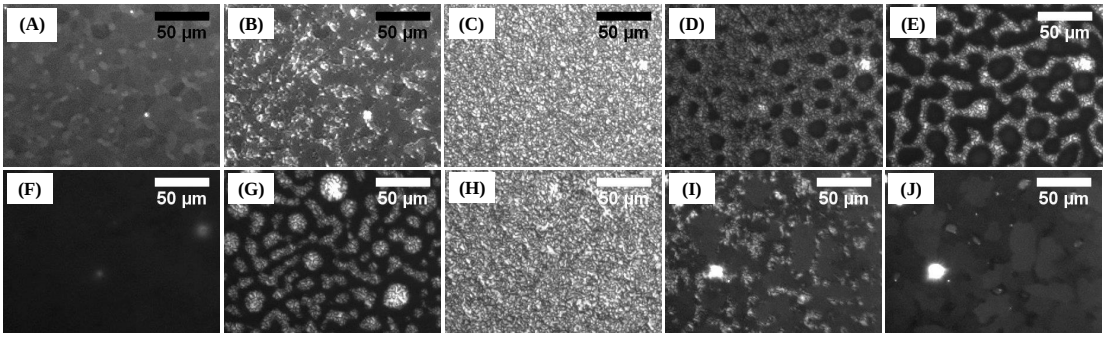

Figure 4.4: Cross-polarized optical micrographs of the thermally annealed phase transition of 54 ± 1.0 nm 8CB film. Image (A) shows the mosaic texture at the surface of the film indicating the smectic G phase. Images (A – F) show the SNI phase transitions with the increase in temperature, $T = 24 \pm 1°C$, 30.1 ± 0.5°C, 31 ± 0.5°C, 38.3 ± 0.5°C, 38.7 ± 0.5°C, and 39 ± 0.5°C, respectively. Images (F – J) show the reverse INS phase transition with the reduction in temperature, $T = 39 \pm 0.5°C$, 38.3 ± 0.5°C, 37 ± 0.5°C, 30.1 ± 0.5°C, and 29 ± 0.5°C, respectively.

For the sake of comparison, the thermally annealed SNI and INS transitions are shown

in the Fig. 4.4. The figure shows that similar to the solvent vapour annealing the SNI and INS phase transitions took place when the temperature is modulated near T_P. The Figs. 4.4(A – C) show that the transition from SN state while the Figs. 4.4(C – F) show that the NI phase transition. The Figs. 4.4(F – J) show that the process was nearly reversible as the nematic and smectic textures at the surface was recovered with the reduction in temperature. The Figs. 4.4(F – H) show the progressive restoration of the nematic order with the reduction in the temperature while the Figs. 4.4(H – J) show the restoration of the mosaic smectic texture at the surface with further reduction in the temperature. The thermally annealed SNI and INS cycles could be repeated for as many times with the periodic increase and reduction in temperature around the T_P. It may be noted here that the temperature induced transition (4.4) of the surface texture is much clearer than the solvent vapour induced transition (Figs. 4.3). This is because of the solvent annealing images always possessed some solvent molecules between the sample and the objective of the microscope, which interfered during the cross-polarized optical imaging.

4.4.2 Sensor Arrangements

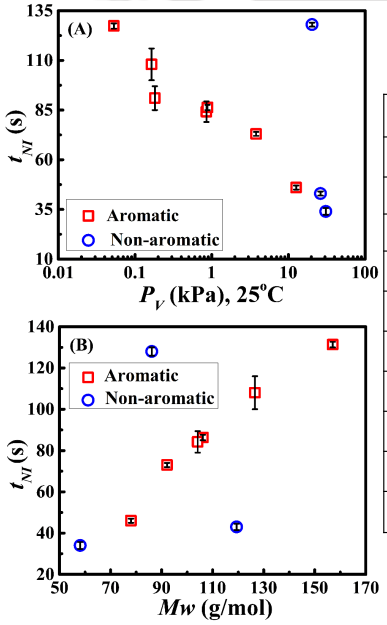

Compound	P_v (kPa) at 25°C	Mw (g/mol)	t_{NI} (s)
Acetophenone	0.0529	120.16	127
Benzyl chloride	0.1639	126.58	108
Bromobenzene	0.55729	157.02	135
Styrene	0.8533	104.15	84
1,2-Xylene	0.8813	106.17	86
Toluene	3.7864	92.14	73
Benzene	12.64	78.11	46
Hexane	20.3983	86.18	128
Chloroform	26.2645	119.38	43
Acetone	30.7975	58.08	34

Figure 4.5: Variation in the time required for NI phase transition (t_{NI}) of a 74 ± 1.0 nm thick 5CB film with (A) the vapour pressure of the solvents (P_v) (B) molecular weight (Mw) when different aromatic and non-aromatic solvents are used. The table shows the typical values of the t_{NI} and P_v at 25°C for different solvents and Mw.

It is well known that the variation in the orientational order of an LC film with temperature has been employed to develop high-precision temperature sensors. Likewise, the solvent vapour induced phase transitions of LC films could also be employed to measure the vapour pressure and volatility of a solvent. Fig. 4.5 shows the results from a set of experiments where the time required for the phase transition of a 5CB film (t_{NI}) under the exposure of various solvers were tabulated and plotted against the vapour pressures of various types of solvents of 5CB (P_v) [193]. The plot suggests that with the increase in the P_v as the solvents became more volatile the t_{NI} reduced. The plot shows the utility of a solvent annealed phase transitions of a nematic film for the development of devices that can measure vapour pressure and volatility of organic solvents. The devices are expected to perform very high-precision measurement of these properties, as it is observed for the LC temperature sensors.

In fact, the solvent vapour induced phase transition behaviour of 5CB materials could also be exploited for identifying different volatile solvents, as shown in the Fig. 4.6. In this situation, instead of a pure LC film, we employed a LC-DAuNP composite droplet as the sensing material. The procedure to synthesize this composite material has already been described in detail in the experimental section. The use of DAuNP improved the electrical response of the LC material. In Fig. 4.6 (A) schematic diagram shows the experimental setup of the vapour sensor, which was very similar to one employed for the previous experiments. The only difference was the use of an electrical circuit, as shown in the Fig. 4.6 (B), which was a pair of Cu electrodes with a spacing of $D_E = 120 \pm 10$ μm decorated on a PDMS surface.

The LC-DAuNP composite drop was placed on the electrodes before the system was solvent annealed and the change in the electrical resistance across the droplet was measured using a multimeter. Figs. 4.6(C – E) show the cross-polarized surface morphology of the droplet, which suggest the progressive destruction of the surface texture leading to an NI transition of the 5CB droplet with the exposure of hexane vapour. The images also show the subsequent decrease in electrical resistance (R) on a multimeter during the phase transition. Importantly, the electrical resistance of the droplet was found to be maximum (R_0) at the purely nematic state in the beginning while at the end the same was found to be minimum (R_m) in the isotropic state. Figs. 4.6(F – H) show the

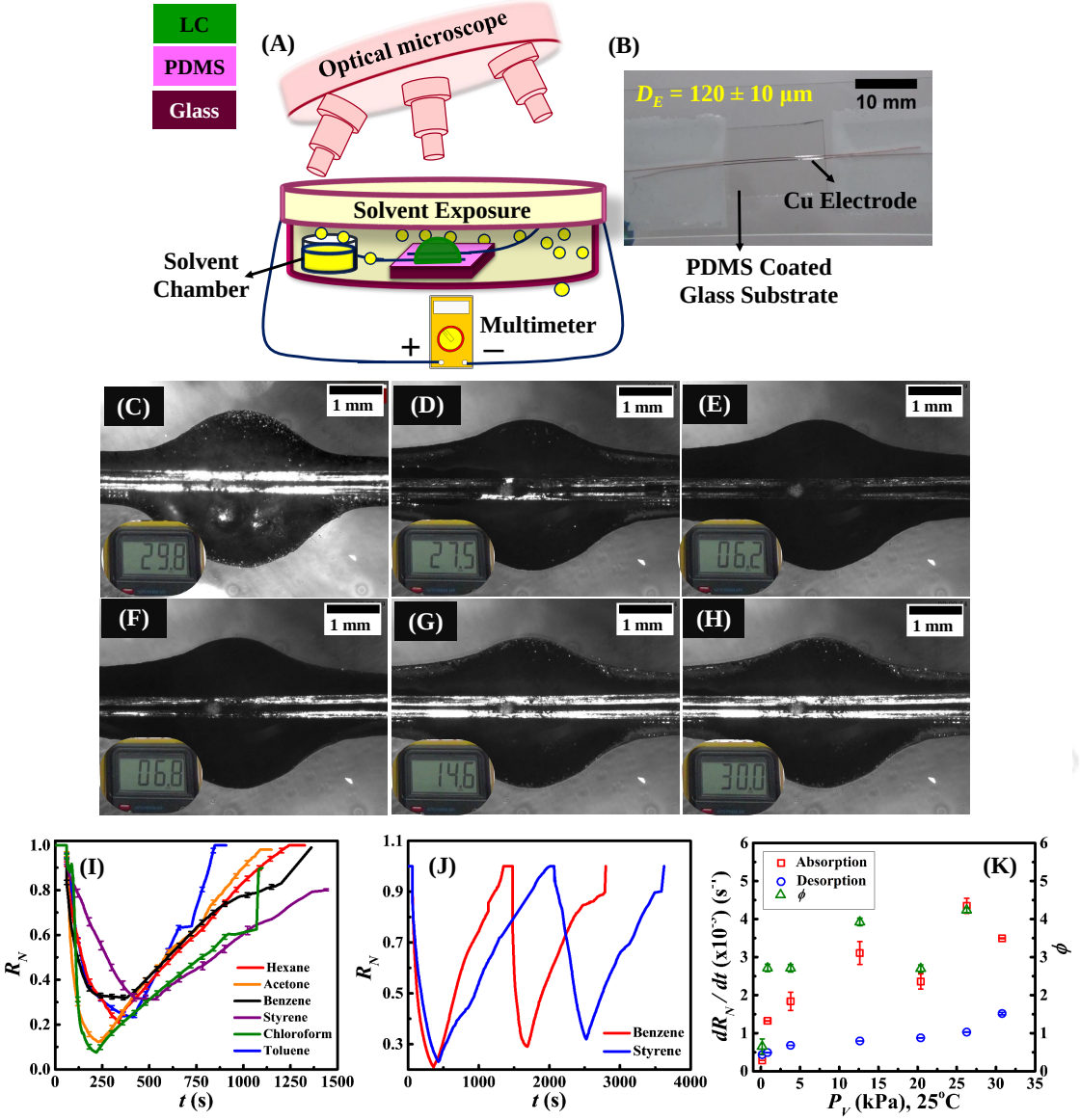

Figure 4.6: The schematic diagram (A) shows the experimental setup of the vapour sensor. Image (B) shows the electrical circuit employed in which a PDMS surface was integrated with a pair of Cu electrodes with a spacing of 120 ± 10 μm. Following this the LC-DAuNP drop was placed on the electrodes before transferring the system into the experimental chamber shown in the image (A) for solvent annealing. Images (C – H) show the cross-polarized surface morphology of the droplet and the subsequent decrease in electrical resistance on a multimeter with hexane solvent exposure during NI phase transition. The plots (I) – (J) show the variation in the normalized electrical resistance ($R_N = R/R_0$) with time (t). Plot (I) shows the variation in R_N with t for different solvent exposure. Plot (J) shows the variation in R_N with t for the two cycles of exposure and withdrawal of the solvent benzene and styrene. Plot (K) shows the variation of dR_N/dt during NI cycle(r_A), dR_N/dt during IN (r_D) cycle with the saturated vapour pressure of the solvent and ratio of the rate of absorption (r_A) and the rate of desorption (r_D), $\phi = r_A/r_D$, for different solvent vapour exposure.

progressive recovery of the nematic texture with the withdrawal of the solvent exposure due to IN phase transition and subsequent increase in the electrical resistance from R_m to R_0.

The plot 4.6 shows the variation in the normalized electrical resistance ($R_N = R/R_0$) with time (t) when the LC-DAuNP droplet was exposed to different solvent vapour. However, we observed a steady reduction of the electrical resistance with the penetration of solvent vapour in the droplet matrix with disappearance of the orientational order of the droplet. The experiments suggested that when the LC droplet retained its orientational order, the molecules resisted the electron flow through the matrix. However, in the isotropic state, as the director orientation was destroyed, the drop matrix facilitated more electron flow through the circuit. Thus, the increase (reduction) in the electrical conductance (resistance) with the solvent penetration during the NI phase transition was solely due to the variation in the orientational order. The reduction (increase) in the electrical conductance (resistance) during IN transition was also attributed to the restoration of the orientational order of the 5CB film due to the solvent desortion from the film matrix. Since the change in resistance took place only during the NI and IN phase transitions, the rate of change of R_N was also a measure of the destruction and recovery of the of the orientational order (S) of the LC droplet with the exposure of the hexane vapour and the withdrawal of the same.

Plot 4.6(J) shows the variation in R_N with t for the two cycles of exposure and withdrawal of the solvents benzene and styrene, which shows that the measurements could be repeated for many times and the sensor arrangement could faithfully track the presence and absence of the solvent vapour. Further, the slope of the R_N vs. t plot could be correlated to the rate of absorption ($r_A \infty dR_N/dt$, plot 4.6(J)) of the solvent molecules in the drop during the NI cycle while the rate of desorption ($r_E \infty dR_N/dt$, plot 4.6(K)) could be obtained from the slope of the R_N vs. t plot during the IN cycle. The plot shows that rate of adsorption and desorption were very different for dissimilar solvent vapour exposures. For example, a volatile solvent such as chloroform showed a much sharper rate of change of R_N during the NI cycle while a much sluggish rate of change of R_N during IN phase transition. Understandably, a volatile solvent like chloroform having high vapour pressure could penetrate more into the LC-DAuNP drop matrix to destroy the nematic order very fast (time for NI transition,t_{NI}) during the solvent vapour exposure state. However, when the solvent vapour exposure was withdrawn, more amount of chloroform needed to evaporate out of the drop matrix leading to a larger

time for recovery (time for IN transition, t_{IN}). In contrast, a relatively lower volatile solvent toluene having a relatively lower vapour pressure could penetrate into the drop matrix at a much slower rate leading to a much smaller rate of change of R_N and a larger t_{NI} during the NI transition. However, absorption of less toluene during the NI cycle helped in smaller t_{IN} and larger rate of change of R_N during desorption. The ratio of absorption to desorption rate, $\phi = \frac{r_A}{r_D}$, was found to be very specific to the different sources of solvent vapour Fig. 4.6(K).

Concisely, the sensor arrangements have shown significant potential to sense the presence and absence of different volatile organic vapours, phase transition of LC materials, evaluation of the order parameter of an LC material during phase transition, rate of diffusion and absorption of a solvent into a LC matrix, and the rate of evaporation of a solvent from a LC matrix.

4.4.3 Pattern Directed Transition

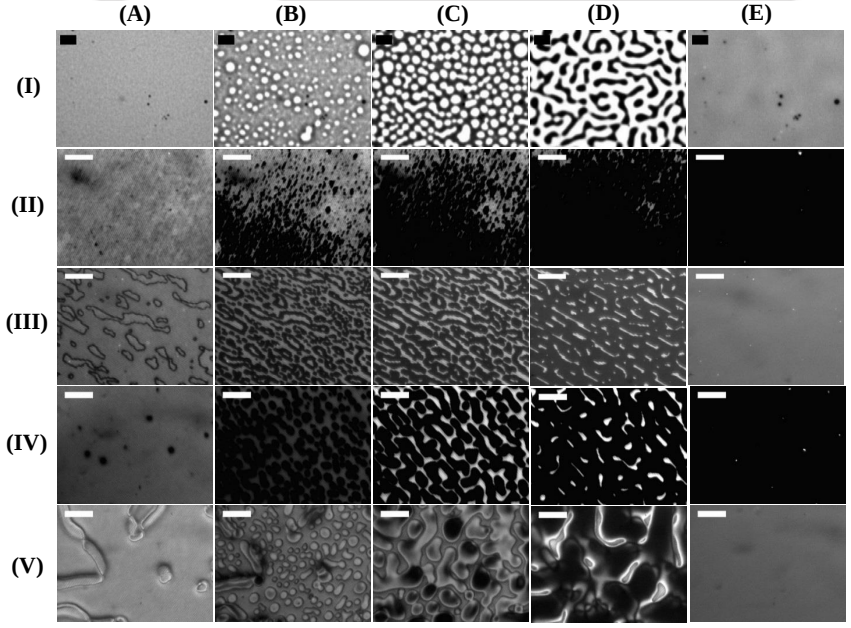

Figure 4.7: The cross-polarized optical micrographs of the solvent vapour mediated NI phase transitions of 5CB films directed by physically heterogeneous "stripe" surfaces. The stripe patterns on the PS substrates were 800 nm wide, 120 nm high, and 1600 nm periodicity. Images in the row (I) show the phase transition on a flat surface whereas images (II) – (V) show that same on the physically patterned surface. The initial concentration of 5CB to cast the films in the rows were, (I) 0.5%, (II) 4.5%, (III) 5%, (IV) 10%, and (V) 40% (w/v), respectively. Images (A) – (E) the rows correspond to (I) 0 s, 50 s, 55 s, 62 s, and 70 s, respectively; (II) 0 s, 140 s, 140.5 s, 141 s, and 142 s, respectively; (III) 0 s, 147 s, 148 s, 149 s, and 153 s, respectively; (IV) 0 s, 150 s, 151 s, 152 s, and 154 s, respectively; (V) 0 s, 156 s, 157 s, 158 s, and 161 s, respectively. The scale bars shown on the images are of 25 μm.

The solvent vapour annealing could also be exploited for pattern directed phase transition, as shown in the Fig. 4.7. The figure suggests that when a thin film of LC material was coated on a stripe patterned substrate the surface undulations appearing during the NI (IN) transition due to the solvent vapour exposure (withdrawal) could show a directionality following the underlying substrate pattern. For example, the row (I) in the Fig. 4.7 show typical appearance and fading of the surface undulations during NI transition on a flat homogeneous surface. However, when a striped substrate was used, the surface undulations became pattern directed as shown in the row (II).

The non-uniformity of the LC film on the strip patterned substrate could engender the NI transition at a much faster rate where the films were thinner while the thicker zones took much larger time for the same. It may be noted here that the percentages mentioned in the figure caption corresponds to the initial concentration of the LC materials in the solvent during the spin-casting. Thus, increase in the concentration meant thicker films on the substrate. The rows (III) – (V) show that with the increase in the thickness of the LC film progressively the influence of the underlying pattern diminished and in the row (V) we observed again the typical phase transition that was observed on a homogeneous flat surface although the underlying substrate had a stripe pattern.

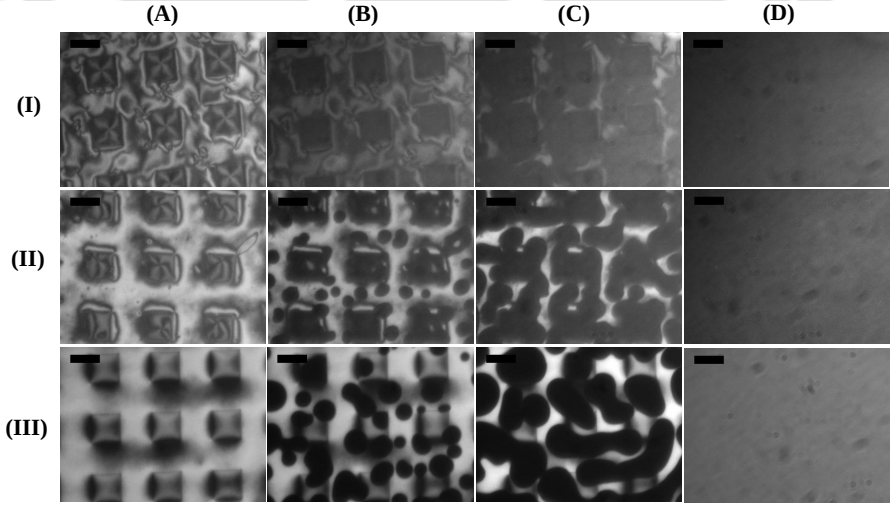

Figure 4.8: The cross-polarized optical micrographs of the solvent vapour mediated NI phase transition of 5CB films directed by physically heterogeneous "box" surfaces. The width, periodicity, and height of the box patterns on the PS substrates were 10 μm, 20 μm, and 300 nm, respectively. The initial concentration of 5CB to cast the films in the rows were, (I) 3%, (II) 6%, and (III) 10%, respectively. Images (A – D) the rows correspond to, (I) 0 s, 90 s, 97 s, and 110 s, respectively; (II) 0 s, 113 s, 115 s, and 117 s, respectively; and (III) 0 s, 145 s, 146 s, and 149 s, respectively. The scale bars shown on the images are of 10 μm.

Fig. 4.8 shows the observations in the Fig. 4.7 was repeatable when the underlying substrate had 'box' like ridges with a very different size and periodicity. The figure suggests that the NI phase transition took place at a much faster rate on the boxes owing to the less thickness of the LC film at that location while in the rest of the portion the phase transition was much slower as the solvent molecules required more time for full penetration and destruction of the director orientation. The Figs. 4.7 and 4.8 together suggest that the solvent vapour mediated phase transition of the LC materials could be exploited to identify the underlying physical patterns or defects below a critical film thickness.

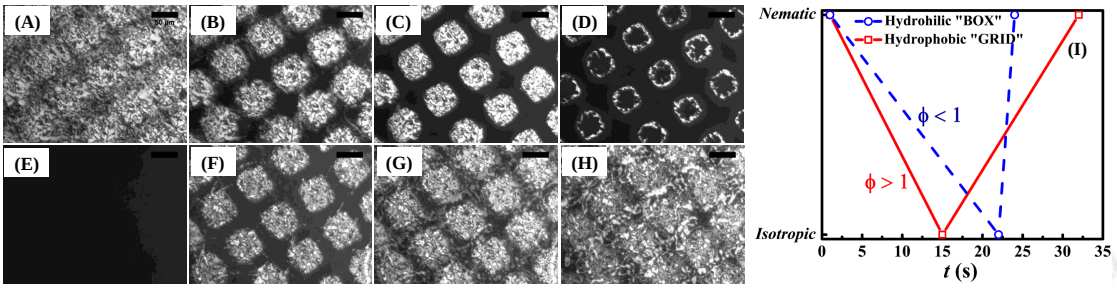

Figure 4.9: The cross-polarized optical micrographs of the solvent vapour mediated phase transition of a 212.4 ± 2.1 nm thick film of 5CB on a chemically heterogeneous substrate with "box" like lyophilic patches of SiO_2/Si and "grid" like lyophobic patches of OTS. Images from (A – E) show NI phase transition with the snapshots at the time intervals, t = 0 s, 146 s, 152 s, 155 s, and 158 s, respectively. The images (E – H) show IN phase transition with the snapshots at the time intervals, t = 0 s, 10 s, 11 s, and 15 s, respectively. Image (I) represents the time required for NI and IN transitions for lyophobic (red, solid line) and lyophilic (blue, dashed line) patch.

In fact, Fig. 4.9 shows that the chemical defects, the extent of lyiphobicity or lyophilicity could also be followed employing a thin coating of the LC film on a surface. For example, in this situation, initially a chemically heterogeneous substrate was fabricated with periodic lyophilic boxes and lyophobic grids, employing the methodology discussed in the experimental section. Following this a thin LC film was coated on the chemically patterned substrate and the films was exposed to solvent vapour. Figs. 4.9 (A – E) show that the solvent annealed NI phase transition was much faster (slower) on the lyophobic (lyophilic) zone because of the weaker (stronger) anchoring of the LC molecules. Figs. 4.9 (E – H) show that for the same reason even the recovery of the orientational order during the IN transition was much faster (slower) on the lyophilic (lyophobic) patches. Understandably, the lyophilic patches allowed easier and faster restoration of the nematic order than the lyophobic patches (Fig. 4.9 (I)). Evidently as the rate of

absorption of solvent molecule is much faster than the rate of desorption in lyophobic patch, the ratio ϕ is greater than 1, whereas for the lyophilic patch the ratio ϕ is smaller than 1. This clearly suggests that the time taken for the solvent vapour induced NI or IN phase transitions of the LC films could easily be correlated to the extent of lyophobicity or lyophilicity of a substrate.

4.5 Summary

In summary, a host of interesting solvent vapour induced phase transitions of crystalline, smectic, and nematic liquid crystal (LC) films have been studied on the plane and patterned surfaces. The major points from the study are,

(i) The solvent vapour induced phase transitions of 7CB and 8CB were studied.

(ii) Crystal state molecular orientation of the 7CB film at room temperature, changed its phase from CNI state with the solvent exposure and reverse phase transition also took place from INC state with removal of solvent exposure.

(iii) Smectic state molecular orientation of the 8CB film at room temperature also changed its phase from SNI state with the solvent exposure and reverse phase transition from INS state with the removal of solvent exposure.

(iv) Solvent induced 5CB thin film NI and IN phase transitions were done with various aromatic and non-aromatic compounds. Interestingly, NI transition time was fast with decrease in vapour pressure (P_v) and increase in molecular weight (Mw).

(v) The solvent annealed phase transition behaviours of a LC-DAuNP composite droplet was converted into an electrical signal with the help of an external circuit. The electrical resistance was found to reduce (increase) upon the destruction (restoration) of the orientational order of the droplet.

(vi) In addition, the solvent annealed phase transition of the LC materials on the physically and chemically heterogeneous surfaces show a pattern directed phase transition. While in the physically heterogeneous surface the variations in the

thicknesses ensured that the NI phase transition was faster at the thinner regimes, in the chemically heterogeneous surfaces the weaker anchoring of the LC molecules on the lyophobic patches ensured a faster NI transition during the solvent vapour exposure.

4.6 Acknowledgments

The help during the experiments from Ms. Snigdha Chakraborty, Ms. Nandini Bhandaru, and Mr. Mitradip Bhattacharjee are gratefully acknowledged.

Chapter 5

Pattern Directed Ordering of Spin-Dewetted Liquid Crystal Micro or Nanodroplets

5.1 Abstract

Chemical pattern directed spin-dewetting of a macroscopic droplet composed of a dilute organic solution of LC formed an ordered array of micro and nanoscale LC droplets. Controlled evaporation of the spin-dewetted droplets through vacuum drying could further miniaturize the size to the level of ∼90 nm. The size, periodicity, and spacing of these mesoscale droplets could be tuned with the variations in the initial loading of LC in the organic solution, the strength of the centripetal force on the droplet, and the duration of the evaporation. The patterned LC droplets showed a reversible phase transition from NI and vice versa with the periodic exposure of a solvent vapour and its removal, respectively. A similar phase transition behaviour was also observed with the periodic increase or reduction of temperature, suggesting their usefulness as vapour or temperature sensors. Interestingly, when the spin-dewetted droplets were confined between a pair of electrodes and an external electric field was applied, the droplets situated at the lyophobic patches showed light-reflecting properties under the polarization microscopy highlighting their importance in the development of micro or nanoscale LC displays. The digitized LC droplets, which were stationary otherwise, showed dielectrophoretic locomotion under the guidance of the external electric field beyond a threshold intensity of the field. Remarkably, the motion of these droplets could be restricted to

the lyophilic zones, which were confined between the lyophobic patches of the chemically patterned surface. The findings could significantly contribute in the development of futuristic vapour or temperature sensors, light reflectors, and self-propellers using the micro or nanoscale digitized LC droplets.

5.2 Introduction

The micro and nanofabrication of LC materials has been one of the very challenging problem because of the presence of the solid like orientation order inside the LC materials alongside possessing the liquid like fluidity. While the inherent elasticity of the LC materials due to the presence of the orientational order of the molecules restricted the disintegration of the macroscopic LC films or droplets into the miniaturized ones, the fluidity of them acted against retaining their shape when disintegrated into smaller parts. In the present study, we show that the combination of a strong centripetal force during spin-casting of a dilute organic solution of a macroscopic LC droplet followed by evaporation of the solvent could indeed create miniaturized droplets having micro or nanoscale size, periodicity, and spacing. The proposed one-step methodology showed the use of chemically patterned surface in imposing long-range order to the micro or nanostructures, which were rather randomly placed when spin-dewetted on a flat and homogeneous surface. Lowering the LC loading in the LC-organic solutions or increasing the spin-speed helped in reduction in size of the spin-dewetted LC droplets. The study also reports a simple protocol where a vacuum evaporation could lead to further miniaturization of the LC droplets in the sub-100-nm regime. Arguably, the proposed methodology shows some unique ways to fabricate high-density micro or nanopatterns of LCs through spin-dewetting, which is rather challenging to fabricate employing any other conventional methods of patterning because of the presence of the restoring solid like orientational order as well as fluidity in the LC materials.

Interestingly, the LC micro or nanodroplets fabricated by the aforementioned methodology could show a reversible NI and IN phase transition behaviours with the periodic exposure and removal of the solvent vapour or with the periodic increase or reduction in temperature, suggesting their usefulness as vapour or temperature sensor. Moreover,

when the LC droplets decorated on the chemically patterned PDMS film were confined between a pair of ITO electrodes and a moderately high external electric field was generated, the LC droplets on the lyophobic zones showed light-reflecting properties. The droplets elongated to touch the upper electrode before undergoing a Fréedericksz transition, which helped in enhancing the light reflection properties under the polarization microscopy. The LC droplets on the lyophilic zones, which were stationary otherwise, showed interesting locomotion under the influence of the electric field at higher field intensities. The findings hold the keys to the development of futuristic nanoscale digitized LC displays with reduced size and weight, nano light-reflectors, self-propelling devices, or miniaturized vapour or temperature sensors.

5.3 Experimental Section

5.3.1 Materials

In the following experiments, 5CB nematic LC (99.99% pure, Sigma-Aldrich, T_P = ~33.5 ± 0.5°C) was used as procured. In order to fabricate the substrates, PDMS was obtained from Dow Corning, Mumbai, India (SYLGARD® 184 kit). The Si substrates (<100> Orientation, Boron doped P type, resistivity 0.01 – 0.02 Ω cm) were purchased from N. J. Int. Cop., India. For "box" patterns, copper (Cu) TEM grids with 300 mesh (lines/inch) were procured from SPI supplies, USA, which had hole width, pitch, and bar width of 58 μm, 83 μm, and 25 μm, respectively. ITO coated glass substrates were procured from Global Nanotech, Mumbai, India. The solvent hexane was employed to make solutions of 5CB and PDMS.

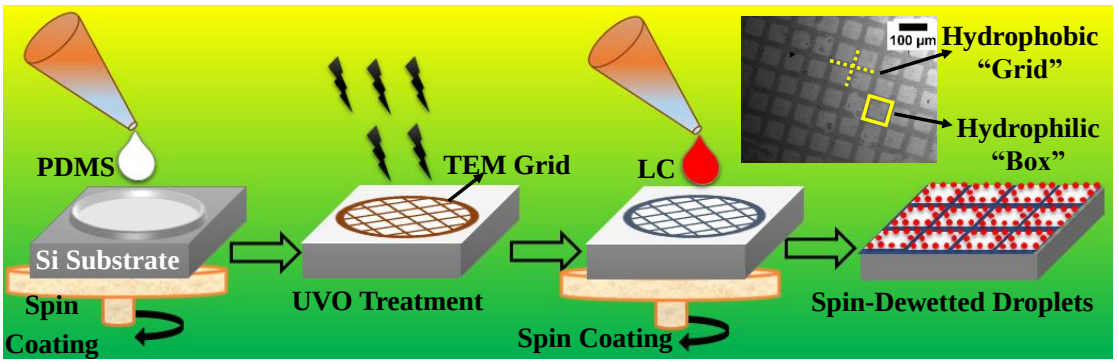

Figure 5.1: Schematic representation of the experimental procedure for the spin-dewetting of 5CB microdroplets on two dimensionally patterned chemically heterogeneous PDMS substrate.

5.3.2 Methods

5.3.2.1 Fabrication of Chemical Patterns

Fig. 5.1 schematically shows the steps to fabricate the chemically patterned substrate and an optical micrograph of a chemically patterned PDMS surface with periodic lyophilic "boxes" and lyophobic "grids". To prepare this substrate, initially, the PDMS oligomer, cross-linker, and hexane solvent (10:1:110 - v/v/v) were mixed and then spin-cast on thoroughly cleaned square (∼1 cm × ∼1 cm) pieces of Si wafers. After spin-coating, the PDMS film was annealed in an air-oven for 24 h at 120°C to simultaneously relax the film, evaporate the solvent, and cure the film. The chemical patterns were decorated on the PDMS substrate by placing a TEM grid and then exposing the masked PDMS substrate with 1 h in a UVO plasma treatment chamber (PSDP-UV4, Novascan Tech. Inc., USA). The exposed area of the PDMS surface, through square openings of the TEM grid, was oxidized by the UVO exposure to form the periodic lyophilic box patterns, whereas the unexposed area under the Cu grid created the lyophobic grid patterns.

5.3.2.2 Spin-Dewetting of Droplets

The spin-dewetting experiments were performed by placing a 100 μl droplet of a known amount of 5CB in hexane (w/v) on a patterned PDMS surface and then spin-casting the same at different spin-speeds ranging from 1000 to 8000 rpm for about 120 s. The samples were dried under vacuum to fully remove the volatile solvent from the matrix

before characterization. The substrates were mounted on the stage of an optical microscope (Leica DM 2500M) to optically characterize the results with the help of a CCD camera using white light in reflection mode. The polarization microscopy was employed to distinguish the isotropic and the nematic phases. The samples were also incubated at ∼1 mm Hg at 24 ± 1°C for different durations (up to 15 days) before performing characterization through atomic force microscopy (AFM, Innova Iris, Bruker-Icon Analytical Equipment). Thicknesses of the PDMS films were experimentally measured by a standard imaging ellipsometer (EP3, Nanofilm, Accurion Scientific Instruments Pvt. Ltd.). Periodicity, spacing, and size statistics were analyzed by the open source ImageJ software.

5.3.2.3 Phase Transition of Liquid Crystals

The phase transition of the 5CB droplets was carried out by initially placing the samples in a closed chamber and then exposing them to solvent vapour by placing 100 μl of the solvent in a separate open container inside the same chamber. The solvent molecules evaporated from the container inside the chamber and then diffused into the droplet matrix to reduce the T_P to the ambient condition [194]. The solvent source was withdrawn from the chamber in order to cause a IN phase transition of the droplets. The thermal phase transitions of the droplets were performed by placing the PDMS substrate decorated with the droplets on a thermal stage (Linkam, THEMS600) and then controlled heating and cooling around the T_P = ∼33.5 ± 0.5°C. The experiments were imaged or video graphed with the help of a camera after placing the chamber on the microscope stage.

5.3.2.4 Electric Field Setup

The electric field experiments were carried out by employing a six-step fabrication methodology: (i) initially a PDMS film of thickness 1.2 ± 0.1 μm was spin-cast on a thoroughly cleaned square (∼1 cm × ∼1 cm) piece of ITO electrode and cured at a temperature of 120°C for 24 h; (ii) then, the surface of the PDMS films were chemically patterned by TEM grid under UVO exposure, as described previously; (iii) thereafter, a

droplet of 5CB-hexane solution was spin-dewetted on the chemically patterned PDMS substrate; (iv) following this the samples were dried under vacuum for 15 min; (v) after that, another ITO substrate was placed from the top to confine the droplet loaded chemically patterned surface; (vi) finally, the ITO electrodes were connected with a direct current (DC) power source (SES Instruments Pvt. Ltd., EHT-II). The experiments were imaged and video recorded by placing the LC cell on the microscope stage.

5.4 Results and Discussion

5.4.1 Spin-Dewetting of Diluted 5CB Solution

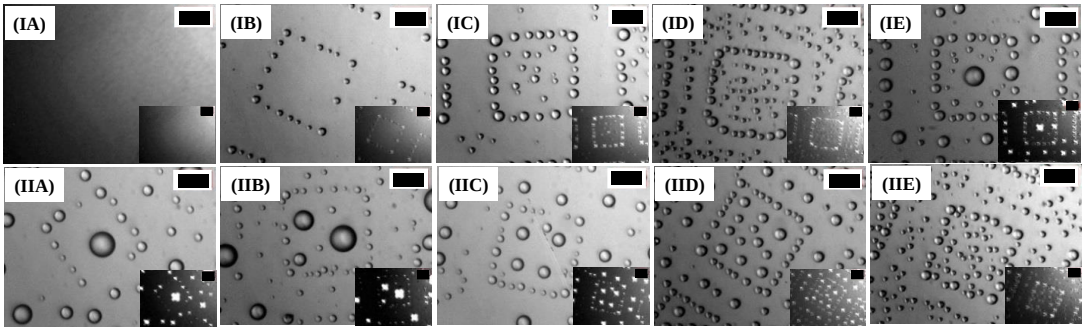

Figure 5.2: (Row I) Optical micrographs showing the spin-dewetted 5CB droplets with the variation in 5CB loading in hexane at 2500 rpm on a chemically heterogeneous substrate. The 5CB loadings in images (IA – IE) were 0.1%, 0.3%, 0.7%, 0.9%, and 1% (w/v), respectively. In the insets, the cross-polarized micrographs of the respective images are shown. (Row II) Optical micrographs showing the spin-dewetted 5CB droplets with increasing spin-speed (1000 – 7000 rpm) for 5CB concentration of 1% (w/v) in hexane on a chemically heterogeneous substrate. The spin-speeds for images (IIA – IIE) were 1000 rpm, 2000 rpm, 3000 rpm, 4000 rpm, and 7000 rpm, respectively. The spin-duration of 120 s was kept constant in all of the experiments. The scale bars shown on the images are of 20 μm.

In the spin-dewetting experiments, initially a macroscopic droplet composed of 0.1 – 1% (w/v) 5CB in hexane was placed on the patterned PDMS surface and spin-cast. Spin-dewetting took place during the spin-coating process because of the combined influence of centripetal, intermolecular, and destabilizing capillary forces. Consequently, the macroscopic droplet disintegrated into the smaller ones, which was then dried under vacuum to evaporate the residual solvent before the optical micrographs were taken. Figs. 5.2(IA – IE) show the spin-dewetted morphologies of LC droplets on the chemically patterned surface after the drying took place. The polarization microscopy images in the insets confirmed that indeed the droplets were composed of nematic LC.

The images show that when the LC loading was on the higher side [Fig. 5.2(IE), 1% (w/v)] the lyophilic box zones and the lyophobic grid zones contained much bigger droplets while an array of droplets of relatively smaller size were 'pinned' near the boundary of the lyophobic and lyophilic zones with an ordering much like the boxes of the TEM grid. Figs. 5.2(IA – ID) show that the size and the number density of the droplets increased in both the lyophilic and lyophobic zones with the 5CB loading. At lower 5CB loadings, the droplets became progressively invisible (e.g., Figs. 5.2(IA) and 5.2(IB)) owing to their significant reduction in size. Later, an AFM analysis showed the presence of further miniaturized nanodroplets in these situations. The size and spacing of the microdroplets decorated on the patterned surface could also be tuned by modulating the spin-speed of the spin-coater as shown in Fig. 5.2(IIA – IIE). The images suggest that at lower spin-speed (∼1000 or 2000 rpm) the lyophilic zones possessed bigger droplets while the lyophobic zones were populated with much smaller ones. Again, a number of droplets were found to be pinned near the junctions of the lyophilic and lyophobic zones to show an ordering of droplets in the pattern of the TEM grid. With increase in the spin-speed, the droplet size reduced and the number density of the droplets increased in both lyophilic and lyophobic zones.

Fig. 5.3 shows the sensitivities of the different parameters obtained from the optical micrographs associated with the experiments shown in the Fig. 5.2. The optical micrograph as an inset within Fig. 5.3(A) shows zones 1 – 3, which correspond to the junction of lyophobic and lyophilic zones, the lyophilic zone, and the lyophobic zone, respectively. The droplet size and the number density of the droplets in each of these zones changed significantly with the variations in the 5CB concentration as well as with the rotational speed of the spin-coater, which are shown in Figs. 5.3(A – D). Figs. 5.3(A) and 5.3(B) show the variations in the average diameter of droplets (D_d) and the number of droplets (N_d) per (100 μm × 100 μm) area with change in 5CB loading (C in % w/v). The plots suggest that D_d and N_d both increase with C especially when the 5CB loading was smaller than 1% (w/v). Reduction in the initial loading of 5CB in the macroscopic droplet reduced the amount of 5CB in the spin-dewetted droplets, which ensured a smaller sized droplet at lower loadings after evaporation of the solvent. The experiments suggested that the size and spacing of the spin-dewetted 5CB droplets

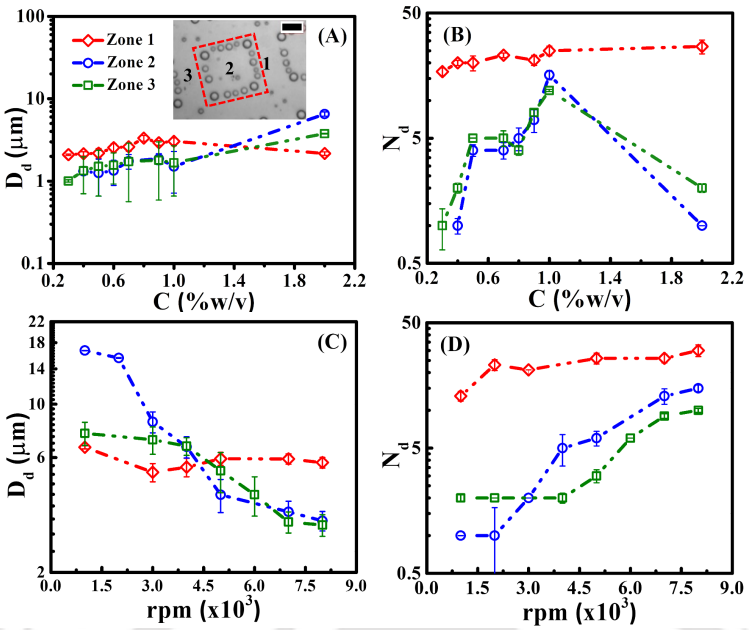

Figure 5.3: (A, B) Variations of the average diameter of droplets (D_d) and the number of droplets (N_d) per unit area (100 μm × 100 μm) in zones 1 – 3 with changes in the initial concentration of LC in the organic solvent (C in % w/v). The optical micrograph shows the edge, central, and peripheral regions of each box pattern classified as zones 1 – 3. (C, D) Variations of D_d and N_d in zones 1 – 3 with change in the spin-speed in the number of rotations per minute (rpm). The scale bar shown on the image is of 20 μm.

could easily be modulated by changing the 5CB loading.

Since the plots in Fig. 5.3 were obtained from the analysis of the optical micrographs, the reduction of D_d and N_d with reduction in C was also an indicator of the increase in the population of nanodroplets on the patterned surface. In particular, the smaller N_d obtained at the lower values of C was an indicator of the increase in the population of the nanodroplets. This was confirmed by AFM images, which are shown later with Fig. 5.5. Figs. 5.3(C) and 5.3(D) show the variations of D_d and N_d in zones 1 – 3 with the spin-speed. The plots suggest that the droplets could be fragmented into the smaller ones and larger in number with the increase in the strength of the centripetal force. The plots also suggest that, in fact, strengthening the centripetal force could increase the number density by about 2 – 3-fold in all of the zones.

Figures 5.2 and 5.3 together suggest a simple but effective way to develop an ordered array of micro or nanoscale LC droplets on a chemically patterned surface in which the droplet size and periodicity could be tuned efficiently by modulating the initial 5CB loading and the strength of the centripetal force.

5.4.2 Vacuum Drying

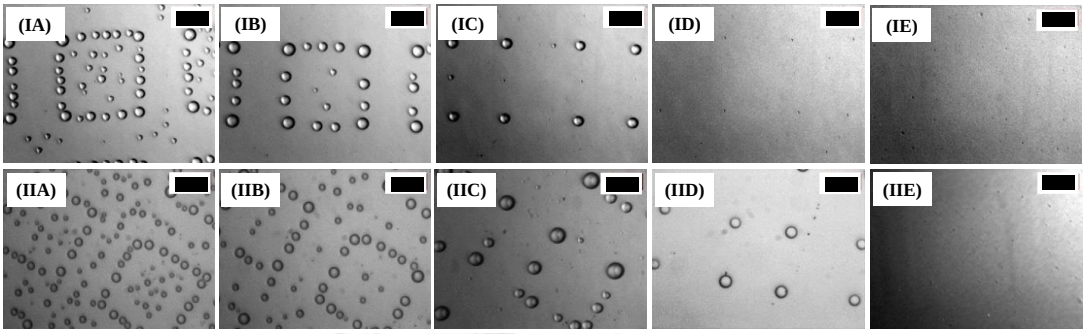

Figure 5.4: (Rows I and II) Optical micrographs of spin-dewetted LC droplets from the solution of 0.7% and 0.9% (w/v) 5CB in hexane, respectively. The spin-speed in both cases was 2500 rpm. Images (A – E) in both rows show that the droplet became invisible when the samples were incubated under ∼1 mm Hg and at 24 ± 1°C for 10 min, 2 h, 24 h, 48 h, and 15 days, respectively. The scale bars shown on the images are of 20 μm.

The optical micrographs in rows I and II in Fig. 5.4 show the spin-dewetted droplets of the systems having 0.7% (w/v) and 0.9% (w/v) loading of 5CB in hexane. Figs. 5.4(A – E) in both rows show that the droplet became almost invisible under optical microscope when the samples were incubated under ∼1 mm Hg and at 24 ± 1°C ranging from 15 min to 15 days. The images in this figure suggest that the LC droplets could further be miniaturized simply by vacuum evaporation of 5CB droplets because the boiling point of 5CB was found to be ∼140 – 150°C when the pressure was 0.5 mm Hg [195]. While the degree of miniaturization was visible for most of the bigger droplets at the centre and the corner of the box patterns, the nanoscale LC droplets were rather invisible under the microscope. In some of the cases (e.g., Figs. 5.4(IIB) and 5.4(IIC)) the microdroplets were also coalesced during the incubation, which occasionally led to a marginal increase in size.

Fig. 5.5 shows the AFM images of the samples shown in Fig. 5.4 after 15 days of incubation under ∼1 mmHg and at 24 ± 1°C. AFM Figs. 5.5(IA) and 5.5(IB) show the PDMS surface in the absence of the 5CB droplets before the spin-dewetting was performed. The images clearly suggest the absence of any droplet on the virgin PDMS surface. Fig. 5.5(IIA) shows the presence of a number of nanodoplets across the lyophilic zone alongside a host of ring shaped 5CB remnants (magnified in Fig. 5.5(IIB)) near the periphery of the box. The ring shaped patterns were the signatures of 5CB evaporation leaving the 'coffee stain effect' type remnants all around the box pattern. The ring structures

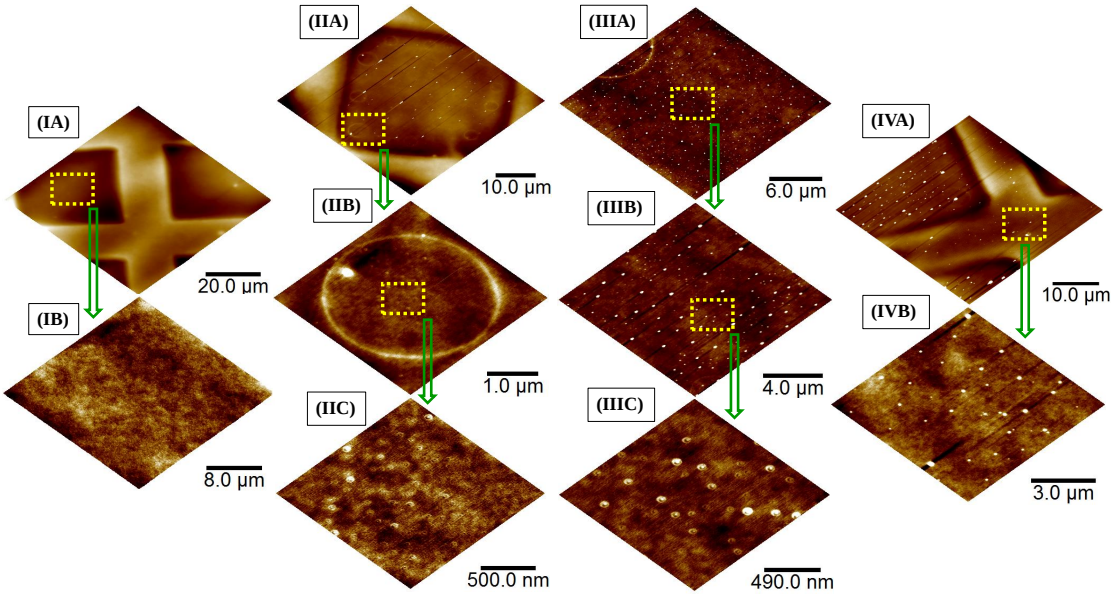

Figure 5.5: (IA, IB) AFM images of chemically patterned PDMS surface after UVO treatment and before spin-dewetting of 5CB. (IIA, IIIA, and IVA) AFM images of nanoscale droplets at the edge (zone 1), box (zone 2), and grid (zone 3) locations when the initial 5CB loading was 0.7%, 0.8%, and 0.9% (w/v) before spin-dewetting at 2500 rpm. All of the AFM images are taken after 15 days of incubation under ∼1 mm Hg and at 24 ± 1°C. Different parts of images (IIA), (IIIA), and (IVA) are magnified in images (IIB – IIC), (IIIB – IIIC), and (IVB), respectively, to show the presence of the relatively 'bigger' and 'smaller' nanodroplets.

were observed especially where the relatively bigger microdroplets were formed during spin-dewetting, which evaporated during the incubation, as shown in Figs. 5.5(IIA) and 5.5(IIB). Importantly, when we magnified further, the AFM images showed a host of nanodroplets of 5CB across the box patterned lyophilic zone, as shown in Fig. 5.5(IIC).

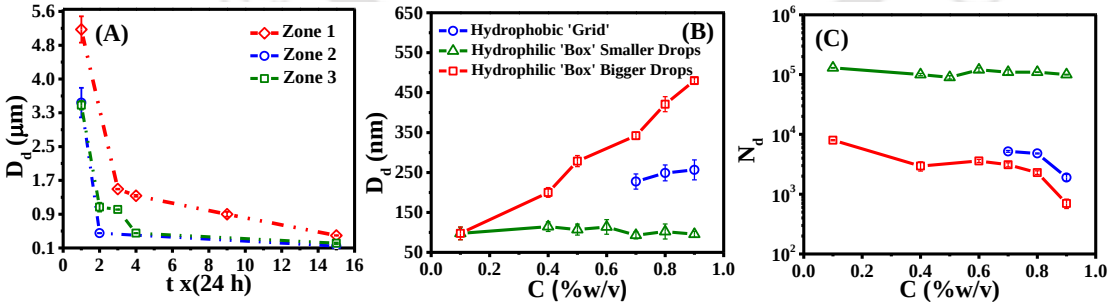

Figure 5.6: (A) Variations in the size of the droplets with the duration of incubation time (t) from AFM analysis in the zones 1 – 3 when the initial 5CB loading was 0.7% (w/v). (B, C) Variations of average diameter of droplets (D_d) and the number of droplets (N_d) per unit area (100 μm) × (100 μm) with concentration (C in % w/v) of 5CB on the lyophilic "box" and lyophobic "grid" after 15 days of incubation under ∼1 mm Hg and at 24 ± 1°C.

These were high-density nanodroplets because the average diameter was ∼91 ± 5 nm

and distance was ∼218 ± 5 nm. Interestingly these droplets were present even inside the previously mentioned rings, as shown in Fig. 5.5(IIC). AFM Figs. 5.5(IIIA – IIIC) show a similar phenomenon for a different 5CB loading, where the magnified view of the sub-100-nm droplets is shown in Fig. 5.5(IIIC). The average drop diameter in Fig. 5.5(IIIC) was ∼102 ± 5 nm, and the average distance was ∼365.4 ± 5 nm. The AFM images at different 5CB loadings (e.g., 5.5(IIA) and 5.5(IIIA)) suggested that, in fact, there were two types of nanodroplets present on the lyophilic zone. The relatively 'bigger' variety was rather sparsely populated and formed either because of controlled evaporation of the relatively larger droplets or because of the coalescence of the relatively smaller ones. The typical size range was found to be about 100 – 600 nm when the initial loading of the 5CB was varied. In comparison, the relatively 'smaller' variety of the nanodroplets was rather densely populated across the lyophilic zone and was of uniform size (∼90 – 100 nm). We pretend that, during the controlled evaporation of the droplets, ultrathin films were formed as intermediates on the lyophilic zones, which eventually broke down to generate the class of smaller nanodroplets. AFM Figs. 5.5(IVA) and 5.5(IVB) show that the nanodroplets were rather sparsely populated on the grid zone when the 5CB loading was higher and were absent at lower 5CB loading.

Fig. 5.6(A) shows the reduction in the size of the droplets with progressive increase in the duration of incubation time (t) from the AFM analysis in zones 1 – 3 when the initial 5CB loading was 0.7% (w/v). Further, panels 5.6(B) and 5.6(C) show the variations of the average diameter of droplets (D_d) and the number of droplets per unit area (N_d) with the 5CB loading (C in % w/v) from the AFM images on the lyophilic box and on the lyophobic grid after 15 days of incubation. The plots suggest that the diameter of the relatively 'bigger' nanodroplets decreased and the number density of nanodroplets increased in both lyophobic and lyophilic zones with reduction in the 5CB loading.

In comparison, as stated previously, D_d and N_d of the relatively smaller nanodroplets were rather uniform across the lyophilic zone with the change in the initial 5CB loading. Importantly, the number density of the smaller droplets was about a few orders of magnitude higher than the bigger ones and the size was in the range of the sub-100-nm regime. Concisely, the Figures 5.4 – 5.6 together show a simple pathway to fabricate an array of ordered 5CB nanodroplets with high periodicity on a chemically patterned

surface with the help of spin-dewetting. The figures also show a methodology to reduce their size further in the nanoscale regime with the help of incubation under moderate vacuum condition and at room temperature.

5.4.3 Applications

5.4.3.1 Vapour and Temperature Sensors

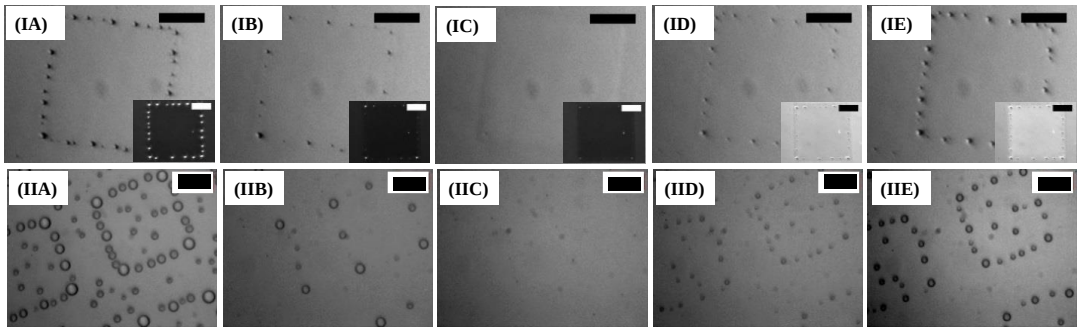

Figure 5.7: Optical micrographs of droplet spreading and retraction experiments after spin-dewetting. Initially a droplet containing 0.3% and 0.7% (w/ v) 5CB in hexane was spin-dewetted at 2500 rpm to form patterns (IA) and (IIA), respectively. (IA – IC) Disappearance of the 5CB droplets with solvent vapour exposure after $t = 0$ s, 115 s, and 215 s, respectively. (IC – IE) Appearance of the 5CB droplets due to the withdrawal of solvent vapour exposure after $t = 0$ s, 23 s, and 141 s, respectively. (IIA – IIC) Surface morphologies of the 5CB droplets with increasing temperature from 23 $\pm$ 0.1°C, 54 $\pm$ 0.2°C, and 72 $\pm$ 1°C, respectively. (IIC – IIE) Surface morphologies of the 5CB droplets with decreasing temperature from 72 $\pm$ 1°C, 68 $\pm$ 0.4°C, and 23 $\pm$ 0.1°C, respectively. In the insets, the cross-polarized micrographs of the respective images are shown. The scale bars shown on the images are of 20 μm.

The optical micrographs in Figures 5.7 and 5.8 show some simple applications possible with the ordered array of spin-dewetted 5CB microdroplets. Figs. 5.7 (IA – IE) show the droplet spreading and retraction with repeated solvent vapour exposure and withdrawal of the 5CB microdroplets. In particular, Figs. 5.7(IA – IC) show the disappearance of the 5CB droplets with contact line expansion due to solvent vapour exposure and Figs. 5.7(IC – IE) show the appearance of the 5CB droplets with contact line retraction due to the withdrawal of solvent vapour. Figs. 5.7(IIA – IIE) show the spreading and retraction of the microdroplets with increase and reduction in temperature. Figs. 5.7(IIA – IIC) show the surface morphologies of the 5CB droplets with increasing temperature, and the Figs. 5.7(IIC – IIE) show surface morphologies of the 5CB droplets with decreasing temperature.

It may be noted here that the exposure of solvent vapour to the 5CB droplets brings

the T_P down to room temperature ($\sim$24 $\pm$ 1°C) causing an NI phase transition while an increase in temperature can cause a NI phase transition beyond 34 $\pm$ 0.1°C. Thus, under the conditions shown in the Fig. 5.7, the droplets underwent NI phase transition because of the solvent vapour exposure either at room temperature or at a temperature beyond the T_P of 5CB, which was also associated with the change in the equilibrium contact angle, as reported by a number of previous works [196]. The cross-polarizer images on the figure confirmed the NI phase transitions of the LC droplets during the process. During the NI transition, the equilibrium contact angle of 5CB decreased on the PDMS surface while getting converted to an isotropic phase, which led to the progressive spreading and disappearance of the microdroplets under an optical microscope. In comparison, when the solvent vapour source was withdrawn (or temperature was reduced below T_P), an IN transition restored the orientational order of the 5CB droplet, which was also associated with an increase in the contact angle of the nematic microdroplet on the PDMS surface. In such a situation, the droplets with higher contact angle were found to resurface under the optical microscope. The reported phenomena under solvent vapour and thermal exposures were found to be reversible and could be repeated for many cycles. It is well-known that the NI and IN phase transitions are widely employed to detect temperature change with high precision. The experiments reported in Fig. 5.7 show the potential of the micro or nanoscale 5CB droplets to act as miniaturized temperature or vapour sensors.

5.4.3.2 Light Reflectors and Locomotives

The ordered array of micro or nanoscale droplets could also show interesting light-reflecting properties under the exposure of electric field, as shown in Fig. 5.8. Schematic Fig. 5.8(IA) shows the setup for the electric field experiment where the 5CB droplets were initially spin-dewetted on a PDMS-coated ITO glass (Fig. 5.8(IB)) and then confined by another ITO coated glass from the top, as shown in Fig. 5.8(IC). The electric field was applied through the confining ITO electrodes. It is well-known that, in a LC cell, a 5CB film can undergo Fréedericksz transition under the influence of an electric field beyond a threshold value of field intensity in which dielectrically anisotropic 5CB molecules change their orientation toward the direction of the applied field. The

cross-polarized optical micrographs 5.8(IIA – IIC) show that when the applied electric potential was ∼102 ± 2 to 106 ± 2 V, initially a number of 5CB microdroplets on the lyophobic "grid" elongated to touch the top electrode, as schematically shown in the Fig. 5.8(IC). Following this, Fréedericksz transition of the 5CB molecules under the electric field led to the formation of microscopic light reflectors on the lyophobic grid zone where the 5CB droplets elongated and touched the top electrode. Importantly, the 5CB microdroplets, which did not elongate and retained their shape, were also shining under the polarization microscopy. However, the brightness of the droplets, which elongated to touch the upper electrode and underwent Fréedericksz transition, was much higher because almost all of the 5CB molecules in these droplets were oriented in the direction of the field. This allowed the entire incident light to reflect back into the detector under the cross-polarizer setup.

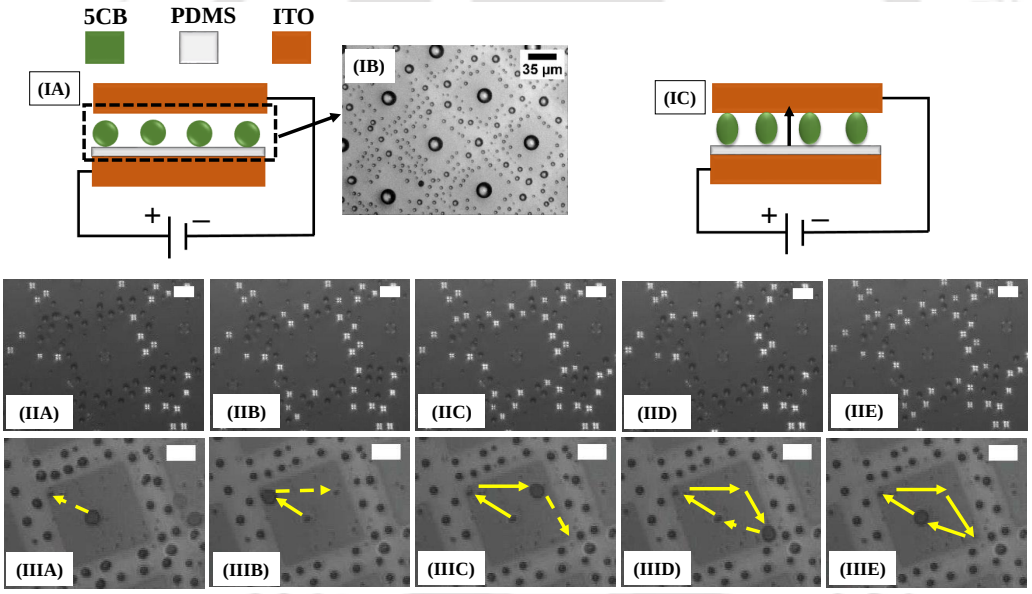

Figure 5.8: (IA) Schematic image of the setup for the electric field experiment where the LC droplets were spin-dewetted on an ITO coated glass, which was precoated with PDMS film of thickness 1.2 ± 0.1 μm. The PDMS-coated ITO substrate was patterned by placing a TEM grid mask and subsequently exposing to UVO. (IB) Patterned PDMS substrate then loaded with 1% (w/v) 5CB spin-dewetted droplets at 2500 rpm and confined by another ITO coated glass from the top. (IC) Schematic representation of the elongation of droplets between the electrodes when the electric field was turned on. (IIA – IIC) Cross-polarized optical micrographs showing the number of droplets having light reflection property that slowly increases as the applied electric field potential was increased from 102 ± 1 V, 104 ± 1 V, and 106 ± 1 V, respectively. (IID, IIE) Cross-polarized optical micrographs showing a transient light reflection phenomenon when the applied voltage was increased to the range 108 ± 2 to 110 ± 2V. (IIIA – IIIE) Dielectrophoretic locomotion of the nematic 5CB droplets within the lyophilic box when the electric field of 115 ± 3 V is applied at times t = 0 s, 3.9 s, 4.3 s, 4.8 s, and 5.3 s, respectively. The scale bars shown on the images are of 20 μm.

The number of droplets having light-reflection property was found to increase as the potential was increased further. When the applied voltage was increased to the range 108 ± 1 to 110 ± 1 V, a transient mode was observed (Figs. 5.8(IID) and 5.8(IIE)) where the reflected light from the droplet started blinking, which indicated periodic elongation and contraction of the 5CB microdroplets under this condition. It may be noted here that since the LC materials are dielectrically anisotropic, they are capable of showing dielectrophoretic motion under the influence of a nonuniform electric field [197]. Figs. 5.8(IIIA – IIIE) show a similar dielectrophoretic locomotion of the nematic 5CB microdroplets when the applied electric field was further increased to ∼115 ± 1 V. Notably, the droplets that retained their shape and did not elongate to touch the upper electrode showed this type of locomotion. Further, the motion of the droplets was restricted to the lyophilic box only. The self-propelling droplets reflected like balls colliding on the walls of a snooker table the moment they reached the junctions of the lyophobic and lyophilic patches.

The movement of the 5CB droplets was restricted to the lyophilic zone because the spreading coefficient of 5CB microdroplets was higher within the box shaped lyophilic regions (surface energy ∼70 mJ/m^2) [171] as compared to the lyophobic grid regions (surface energy ∼20 mJ/m^2) [171]. This enabled the 5CB droplets to partially wet and have lower contact angle inside the lyophilic regions and retain their shape even at higher field intensities. Since they did not elongate to touch the upper electrode, in order to release the electrohydrodynamic stresses near the contact line and the LC-air interface, the droplets showed lateral movement. While in motion, the droplets retracted back sharply to the lyophilic zone when they encountered the boundary of the lyophilic and lyophobic patches because of the abrupt increase in the Laplace pressure, curvature, and contact angle near the lyophobic region. The equilibrium contact angles of 5CB droplets on lyophobic and lyophilic PDMS substrates are about 63° and 50°, respectively. We also observed that the locomotion was not restricted solely to the lyophilic patches. For example, if some of the droplets in the lyophobic patches were not elongated under the influence of electric field, they also exhibited the dielectrophoretic motions at a relatively higher field intensity.

5.5 Summary

In this study we showed a simple and low-cost top-down methodology to fabricate an array of ordered micro or nanodroplets of LC materials. The summary of the study is,

(i) An ordered array of LC micro or nano droplets were generated by spin-dewetting of macroscopic droplet composed of very diluted LC solution on chemically patterned substrates.

(ii) Spin-dewetted droplets size, spacing, and periodicity could be controlled by controlling the initial concentration of 5CB and strength of centripetal force. With increasing the 5CB loading in the initial concentration, the drop diameter and number density both were increased on lyophilic and lyophobic zones. Again, with increasing centripetal force on the macroscopic drop, the spin-dewetted drop diameter decreased whereas number density of the droplets increased in both the lyophilic and lyophobic zones.

(iii) Importantly, when the 5CB loading decreased in the initial concentration the drop diameter decreased alongside number density also decreased. It conveyed that the nanodroplets number density increased with decreasing the initial concentration.

(iv) The size of the spin-dewetted droplets could miniaturized further by evaporation of the LC from the droplets when they incubated at $\sim$1 mm Hg at 24 $\pm$ 1°C for different durations (up to 15 days).

(v) After the 15 days vacuum drying, the samples were analyzed by AFM. The AFM images showed that highly populated nano droplets on lyophilic zone and sparsely populated nanodroplets on lyophobic zone were placed. Importantly, on lyophilic zones two types of nanodroplets were populated. One was sparsely populated relatively 'bigger' nanodroplets and another was that highly populated smaller nanodroplets. These 'bigger' variety was rather formed either because of controlled evaporation of the relatively larger droplets or because of the coalescence of smaller droplets. Further, relatively 'bigger' droplets size was increased with increasing initial concentration of solution whereas smaller droplets size was $\sim$90 – 100 nm remained unchanged.

(vi) The spin-dewetted micro or nanodroplets showed a reversible phase transitions from NI and vice versa with the periodic exposure and removal of the solvent vapour or with the periodic increase or reduction in temperature.

(vii) When these microdroplets were confined between a pair of electrodes and an external electric field was applied, they showed pixelated light-reflecting properties under the polarization microscopy.

(viii) In addition, the digitized LC droplets, which were stationary otherwise, showed interesting dielectrophoretic locomotion restricted to the lyophilic zone under the influence of the externally applied electric field.

(ix) The study contribute significantly for futuristic miniaturized vapour and temperature sensors, display units, and self-propellers by using LC micro or nanodroplets.

5.6 Acknowledgments

The help during the experiments from Ms. Snigdha Chakraborty and Mr. Mitradip Bhattacharjee are gratefully acknowledged.

Chapter 6

Solvent Vapour Mediated Contact Line Instabilities of Liquid Crystal Droplets

6.1 Abstract

A LC microdroplet could rapidly spread upon solvent vapour annealing to form a non-uniform film on a PDMS substrate, which disintegrated into a collection of nanodroplets upon the withdrawal of the solvent exposure followed by drying. The LC droplet underwent a NI phase transition upon solvent exposure at room temperature before spreading into a non-uniform film. While the lyophobic surfaces restricted the spreading of the droplet to form thicker films upon solvent vapour exposure, the lyophilic substrates allowed the formation of thinner films. Withdrawal of the solvent exposure caused rapid evaporation of the solvent molecules near the rapidly retracting contact-line of the film to facilitate the formation of the LC droplets having size and periodicity as low as ∼100 nm and ∼200 nm. The thinner films on the lyophilic surfaces allowed the formation of the droplets having smaller size and periodicity while the use of a physicochemically patterned substrate with periodic lyophobic and lyophilic patches could direct these instabilities to impose a large-area ordering to the nanodroplets. A theoretical model of an evaporating thin film composed of an LC solution of a volatile solvent uncovered that the spacing of the droplets was decided by the interplay between the stabilizing and destabilizing components of the capillary forces for the relatively thicker films while the van der Waals interaction played a supportive role when the thickness of the LC-solvent film was less than 100 nm. Interestingly, when the miniaturized droplets were brought

under the exposure of an electric field employing a setup analogous to electrowetting, they showed an anomalous oscillatory rotational motion originating from the difference in the Laplace pressure near contact line. Application of Lorentz force to these droplets showed exciting translational and rotational motions followed by ejection of miniaturized microdroplets.

6.2 Introduction

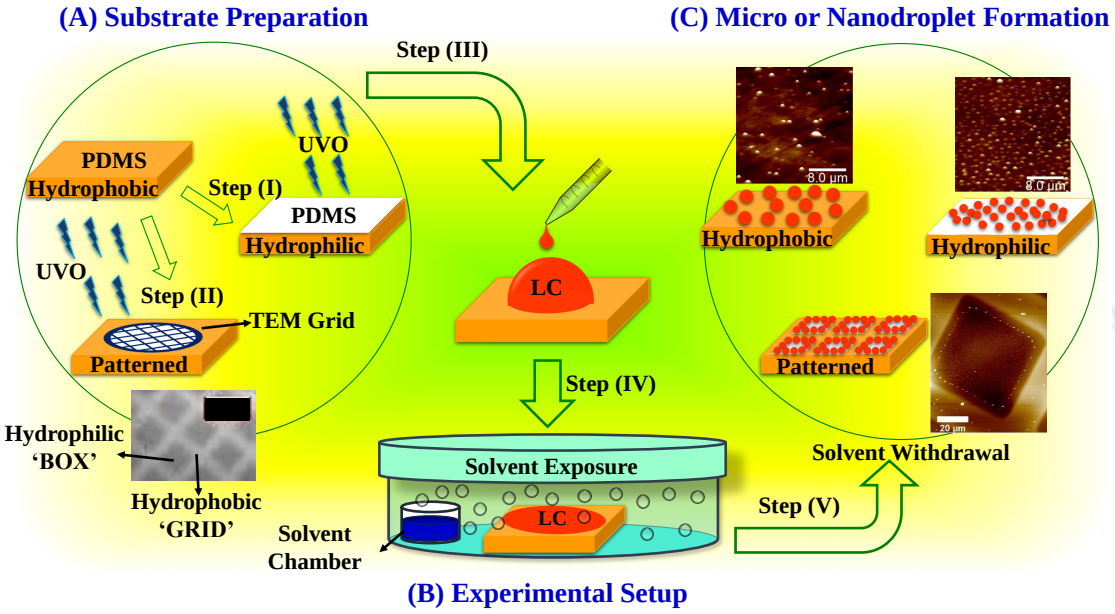

Figure 6.1: The schematic diagram shows the production of 5CB LC nanodroplets on the PDMS substrates. (A) Substrate preparation – step (I) shows the fabrication of homogenous lyophilic PDMS substrate by UVO exposure. The step (II) shows the fabrication of chemically heterogeneous PDMS substrate when it was covered with a TEM grid before the UVO exposure. The optical micrograph shows chemically heterogeneous PDMS substrate after treating with UVO for ∼2.5 h where the scale bar is 100 μm. (B) Experimental setup – step (III) shows the placement of the LC droplet on the PDMS substrate, which was then placed inside a chamber having a source of solvent vapour, as shown in the step (IV). (C) Micro or nanodroplet formation – step (V) shows the withdrawal of the solvent exposure and formation of LC micro or nanodroplets. The AFM images show the typical morphologies of LC droplets.

In the present study, a single step methodology is reported to slim down a microscopic nematic LC droplet into an array of nanoscopic droplets with sub-micron periodicity. Fig. 6.1 shows the typical steps to this fabrication process in which initially a micro-droplet of LC was placed on a PDMS substrate before exposed to a vapour of a volatile solvent of the LC material. Subsequently, the solvent penetrated into the droplet matrix through the adsorption at the LC-air interface. With more solvent absorption into the

drop led to the NI phase transition followed by a reduction in the equilibrium contact angle. This caused a progressive spreading of the droplet into a non-uniform film with a relatively thinner (thicker) zones near the contact line (central portion). At this stage, when the solvent exposure was withdrawn, the volatile solvent evaporated preferentially from the thinner peripheral zone near the contact line to engender a contact-line instability. Consequently, rapid evaporation of the solvent vapour from the film matrix enforced the contact line to rapidly retract towards the central portion of the film to leave an array of LC droplets having size and periodicity as small as ∼100 nm and ∼200 nm, respectively, after drying. The size and periodicity of the droplets were found to be tunable with the wettability of the LC-solvent solution on the PDMS substrate. Further, the use of a chemically heterogeneous PDMS surface could impose long-range order to the patterns decorated.

A theoretical model was developed for an evaporating thin film composed of a solute-solvent solution to qualitatively predict the experimentally obtained periodicity of the nanodroplets. A recent study has shown that the thermal annealing of LC droplets could form an array of daughter microdroplets near the contact line [165]. In comparison, we show that use of the present methodology could develop a very uncommon solvent vapour evaporation mediated instability near the contact line to facilitate the decoration of high-density nonpatterns employing a self-organized pathway.

The proposed methodology is very different from the previously reported self-organized instabilities [13, 64, 198] of ultrathin films composed of polymeric or LC materials. In addition, the contact-line instability is also very different from the ones reported previously for the LC droplets [146, 150, 194, 199].

Interestingly, the micro or nanodroplets of LCs fabricated could show a host of interesting rotational and translational motions alongside the ejection of satellite droplets while undergoing autonomous rotational motion under the influence of external electric field or Lorentz force. Arguably, fabrication of such large-area patterns of LC materials having micro or nanoscale size and periodicity can be very challenging through any other nanofabrication technique.

6.3 Experimental Section

6.3.1 Materials

The 5CB (99.99% pure, Sigma Aldrich, T_P = ∼33.5 ± 0.5°C) nematic LC was used for the experiments without any further processing. The SYLGARD® 184 kit of PDMS was procured from Dow Corning, India. The Si substrates (<100> Orientation, Boron doped P type, resistivity 0.01 – 0.02 Ω cm) were purchased from N. J. Int. Cop., India. The Copper (Cu) TEM grids with 300 mesh (lines/inch) were procured from SPI supplies, USA, which had hole width, pitch, and bar width of 58 μm, 83 μm, and 25 μm, respectively. The ITO coated glass was procured from Global Nanotech., India. Analytical grade solvent hexane was procured Sigma Aldrich to make solutions of 5CB and PDMS.

6.3.2 Methods

6.3.2.1 Substrate Preparation

The experiments were performed on the three different type of substrates, lyophobic-homogeneous, lyophilic-homogeneous, and chemically heterogeneous. The step (I) in Fig. 6.1 schematically shows the pathways to develop the homogeneous and chemically heterogeneous surfaces. In this regard, initially, the PDMS oligomer, cross-linker, and hexane solvent (10:1:110 - v/v/v) were mixed together before spin-coated at 2500 rpm for 120 s on the thoroughly cleaned pieces of Si wafers (∼1 cm × ∼1 cm). Following this, the liquid PDMS thin film was hard-baked in the air-oven for 24 h at ∼120°C to obtain the lyophobic and homogeneous solid substrate. The typical PDMS film thickness was maintained at ∼1.2 ± 0.1 μm, which was measured by the Imaging Ellipsometer (EP3, Nanofilm, Accurion Scientific Instruments Pvt. Ltd.). The step (I) in Fig. 6.1 shows that the lyophobic PDMS film was converted into a lyophilic one by exposing the film to the UVO for ∼1 h (PSDP-UV4, Novascan Tech. Inc., USA). The chemically heterogeneous surfaces were prepared following the step (II) in Fig. 6.1. In this case, the lyophobic PDMS was initially masked at the top by a TEM grid before exposing

the same with UVO exposure for ∼2.5 h. The optical micrograph (Leica DM 2500M) of the chemically patterned PDMS surface shows that the square (grid) openings (covers) of TEM grid created the "box" ("grid") like lyophilic (lyophobic) patches on the PDMS surface. Atomic force microscopy (AFM, Innova Iris, Bruker-Icon Analytical Equipment) images suggested that the height difference between the lyophilic "square" and lyophobic "grid" patches was ∼35 ± 2.0 nm due to the UVO etching of the PDMS surface under the exposed area.

6.3.2.2 Experimental Setup

The step (III) – (V) in Fig. 6.1 shows the experimental methodology for the generation of micro or nanoscale 5CB LC droplets. Initially, a 5CB droplet (diameter, 30 – 250 μm) was dispensed on the PDMS substrate from a micro-pipette, as shown in the step (III). The droplet with the substrate was placed inside an experimental chamber of glass petri dish, as shown in the step (IV). After the droplet reached equilibrium contact angle, the solvent hexane was introduced in 20 small solvent containers of 200 μl placed surrounding the substrate, before the top of the experimental chamber was covered with another petri dish. After 2 – 5 h exposure to solvent vapour when the LC droplet was converted into an LC film due to the contact line spreading under the solvent exposure, the petri dish cover at the top was removed and the solvent vapour source was withdrawn from the chamber. In consequence, the volatile solvent diffused out of the film matrix before while generating the micro or nanoscale droplets through contact line instability. Following this, the samples were dried under vacuum for 24 h at 24 ± 1.0°C to remove the excess solvent, as shown in the step (V). The dried samples were analyzed by AFM and CCD camera using white light in reflection mode. Periodicity, spacing, and size statistics were analyzed by ImageJ open source software.

6.3.2.3 Lorentz Force Experiment

In order to perform this experiment, in the beginning, ITO coated glass was coated with a PDMS thin film and subsequently, the 5CB micro or nanodroplets were fabricated on the PDMS surface following the methodology discussed previously. The only difference

in the protocol was the 5CB micro or nanodroplets were dried for lesser duration ∼15 min under vacuum conditions at 24 ± 1°C. Following this, another ITO glass substrate was placed on the top of the PDMS substrate decorated with 5CB micro or nanodroplets. Thereafter, the top and the bottom ITO glasses were used as electrodes to apply a direct current (DC) power source (SES Instruments Pvt. Ltd, EHT-II) to this system. Apart from the electric field, a pair bar magnet (0.398 ± 0.01 T) was placed perpendicular to the electric field, in order to develop the Lorentz force necessary for the motion. The droplets elongated to touch the top electrode when the applied voltage was ∼25 ± 1 – 30 ± 1 V, which ensured a current flow through the droplet and the electric field circuit. The current (**J**) interacted with the magnetic field (**B**) to produce the Lorentz force (**F** = **J** × **B**) necessary for the motion.

6.3.2.4 Theoretical Model

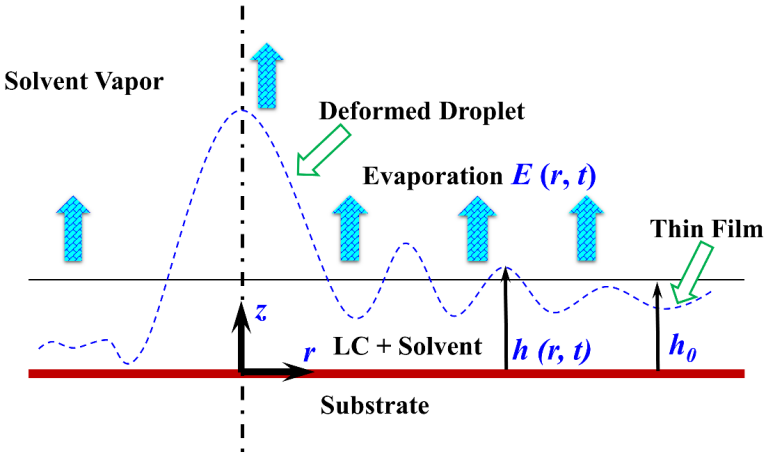

Figure 6.2: Schematic representation of an evaporating droplet connected to a non-uniform thin liquid precursor film evaporating at a rate $E(r,t)$ on a solid substrate. The image shows the typical geometry employed in the problem formulation where the local thickness of the liquid domain is $h(r,t)$ and the mean film thickness, h_0.

(A) *Problem Formulation*

The theoretical model was developed to predict the spacing between the droplets formed. For the ease of formulation, we assumed that under the exposure of the solvent vapour for a very long duration the LC droplet adsorbed and then absorbed excess solvent to form a shape of a droplet connected to a precursor thin film with a perturbed air-liquid interface, as shown in Fig. 6.2. We also assumed that the solvent evaporated out of this configuration at a rate $E(r,t)$ to form the micro or nanodroplets. An axisymmetric

polar coordinate system (r, z) was employed for the formulation with the origin fixed at the film-substrate interface. The notations r and z represent radial and axial coordinates and t represents time. The local thickness of this configuration was assumed to be $h(r,t)$ while the mean thickness was, h_0. The initial concentration (C_i) of the LC in the bulk was assumed to be less as compared to the solvent due to the long solvent vapour exposure. The concentration, $C(r,t)$ of the LC was assumed increased progressively with time as solvent evaporated out from the droplet. Thus, the constitutive relation for a Newtonian fluid, $\overline{\overline{\mathbf{T}}}_f = \mu(\nabla\mathbf{u} + \nabla\mathbf{u}^T)$, and the continuity equation for an incompressible fluid, $\nabla \cdot \mathbf{u} = 0$, could be employed alongside Navier-Stokes equations of motion, $\rho D\mathbf{u}/Dt = -\nabla P + \nabla \cdot \overline{\overline{\mathbf{T}}}_f$, to model the dynamics of this process. The bold variables with and without double overbar represent tensor and vector, respectively, the subscripts preceded by a comma signify differentiations with respect to the subscripted variable, D/Dt denote substantial derivative, and the variables with subscripts r and z denote components of the vector or tensor in the respective direction, respectively. The notations $\overline{\overline{\mathbf{T}}}_i$ and $\mathbf{u}\{v_r, v_z\}$ represent the stress tensor and velocity vector, respectively. The expressions inside the curly brackets are the vector components. The subscript i correspond to the film $(i = f)$ and the bounding fluid $(i = v)$ stress tensor while the symbols μ, ρ, γ, A_e, p_0, and P $(= p - \pi)$ denote the viscosity, density, surface tension, effective Hamaker constant, ambient pressure, and total pressure, respectively. The notation p denotes fluid pressure while the excess pressure due to intermolecular forces is, $\pi = -A_e/6\pi h^3$. The symbol $\overline{\overline{\mathbf{I}}}$ is the identity tensor, $\nabla_s (= (\overline{\overline{\mathbf{I}}} - nn) \cdot \nabla)$ is the surface gradient operator, and the unit outward normal and tangential vectors are expressed as, $\mathbf{n}\{(-h_{,r}, 1)/\sqrt{1 + h_{,r}^2}\}$ and $\tau\{(1, h_{,r})/\sqrt{1 + h_{,r}^2}\}$ [200].

No-slip and impermeability $(\mathbf{u} = 0)$ boundary conditions were enforced at the solution-solid interface $(z = 0)$. Further, normal $[\mathbf{n} \cdot \left(-p_0\overline{\overline{\mathbf{I}}} + \overline{\overline{\mathbf{T}}}_v\right) \cdot \mathbf{n} - \mathbf{n} \cdot \left(-p\overline{\overline{\mathbf{I}}} + \overline{\overline{\mathbf{T}}}_f\right) = \gamma\kappa]$ and shear $[\mathbf{n} \cdot \overline{\overline{\mathbf{T}}}_v \cdot \tau - \mathbf{n} \cdot \overline{\overline{\mathbf{T}}}_f \cdot \tau = 0]$ stress balances along with the kinematic condition $[h_{,t} + \mathbf{u} \cdot \nabla_s h = v_z - E]$ were employed at the solution-air interface $[z = h(r,t)]$. The curvature of the free deforming surface was, $\kappa = \nabla_s \cdot \mathbf{n}$. The evaporation rate was estimated as, $E = e_0(1 - C)^v$ [201, 202], where e_0 and C are the rate of evaporation of the pure solvent and the concentration of LC in the solution defined as, $C = LC/(LC + S)$, when, $h = (LC + S)$ [202]. The notations LC and S represent the quantities of LC and

solvent in the solution. The exponent v decided the kinetics of evaporation and was in the range $0 \leq v < 1$ [201]. In this formulation, we have considered only the pure solvent (S) is evaporated while the amount of LC remained constant, which eventually led to the expression, $E = -S_{,t}$ [202]. Differentiating C with respect to time we obtained the expression,

$$C_{,t} = \frac{Ce_0(1-C)^v}{h}. \tag{6.1}$$

The variations in the concentration (C) and evaporation from the solution-air interface also allowed Marangoni flow, which was modeled as, $\gamma(r) = \gamma_{ps} + mC(r,t)$ [202], where γ_{ps} is the surface tension of the pure solvent and m is the slope of the variation in surface tension with $C(r,t)$. The evolution equation of the deforming LC-solvent solution-air interface was theoretically modeled under the lubrication approximation [203–207] considering $r \gg z$ where $r \to O(1/\varepsilon)$, $(z, h, v_r) \to O(1)$, $t \to O(1/\varepsilon)$, and the parameter, $\varepsilon \ll 1$. In this limit, the incompressibility condition and the r- and z- directional equations of motion were reduced to $(rv_r)_{,r} + rv_{z,z} = 0$, $P_{,r} - \mu v_{r,zz} = 0$, and $P_{,z} = 0$, respectively. The reduced equations were solved analytically to obtain the general solutions for v_r and v_z. The integration constants of the general solutions were evaluated by enforcing no-slip ($v_r = 0$) and impermeability ($v_z = 0$) boundary conditions at the solution-solid interface ($z = 0$) along with the normal ($P - p_0 - (A_e/6\pi h^3) + (\gamma_{ps} + mC)h_{,rr} - (((\gamma_{ps} + mC)/h) = 0$)) [203, 206, 207] and tangential ($v_{r,z} = 0$) stress conditions at the solution-air interface ($z = h$). The curvature of the deforming interface consisted of both the curvature terms, $\kappa\,|_h = (z^{-1}(zn_z)_{,z} + n_{r,r})\,|_h = (1/h) - h_{,rr}$ [200]. The solutions of the velocity components (v_r, v_z) were replaced in the kinematic condition, $h_{,t} + v_r\,|_h\, h_{,r} = v_z\,|_h - e_0(1-C)^v$ [201], to obtain the following nonlinear partial differential equation (PDE) for the deforming solution-air interface undergoing evaporation [204, 205],

$$h_{,t} = \frac{(rh^3P_{,r})_{,r}}{3r\mu} - e_0(1-C)^v. \tag{6.2}$$

(B). *Linear Stability Analysis*

The normal linear modes [203, 204], $h(r,t) = h_0(t) + \tilde{h}(r)e^{\omega t + ikr}$ and $P = \bar{P} + \tilde{P}(r)e^{\omega t + ikr}$, were used to linearize the evolution equation (Equation (6.2)), where the notations ω and k signify the growth coefficient and the wave number of the perturbation, h_0 and $\bar{P}$

are the base-state thickness and pressure, respectively, while the over-tilde symbols are perturbed variables. The base-state expressions for $\bar{P}$ and h_0 were obtained as follows [203],

$$\bar{P} = p_0 + \frac{A_e}{6\pi h^3} + \frac{(\gamma_{ps} + mC)}{h_0}, \tag{6.3}$$

$$h_{0,t} = -e_0(1-C)^v. \tag{6.4}$$

Employing the expressions for the normal linear modes in the Equation 6.1 we obtained [202],

$$C_{,t} = \frac{Ce_0(1-C)^v}{h_0}. \tag{6.5}$$

The coupled ordinary differential equations (ODEs) (Equation (6.4) and Equation (6.5)) were solved simultaneously to obtain the solutions for h_0 and C. The exponent v was derived considering $Ch_0 = C_i h_i$ [201], as LC was assumed to be non-volatile. The symbols C_i and h_i signify the initial concentration and initial base-state thickness of the film. Thus, from Equation (6.4) we obtained [201],

$$C_{,t} = \frac{e_0 C^2(1-C)^v}{C_i h_i}, \tag{6.6}$$

which was integrated to find the evaporation time [201],

$$t_{evp} = \frac{C_i h_i}{e_0} \int_{C_i}^{1} \frac{dC}{C^2(1-C)^v}. \tag{6.7}$$

The exponent v was obtained for any finite t_{evp} after performing the integration numerically. It was observed that the integration converged for, $v < 1$ [201]. We considered $t_{evp} \approx 60 - 75$ s, similar to the time observed in the experiments. The perturbed pressure term was $\tilde{P} = (-(A_e/2\pi h_0^4) + k^2(\gamma_{ps} + mC) - ((\gamma_{ps} + mC)/h_0^2)))\tilde{h}$, derived from the linearized normal stress balance. Replacing $\tilde{P}$ in the linearized Equation (6.2) led to the dispersion relation for the instabilities of the evaporating liquid film disintegrating into droplets as [203],

$$\omega = \frac{h_0^3}{3\mu}\left(k^2(\gamma_{ps} + mC) - \frac{A_e}{2\pi h_0^4} - \frac{(\gamma_{ps} + mC)}{h_0^2}\right)\left(\frac{ik}{r} - k^2\right). \tag{6.8}$$

The essential and adequate condition for the instability (stability) of the liquid film was

$Re[\omega] > 0 (Re[\omega] < 0)$. The interplay between the stabilizing surface tension (first term in the right-hand side), the destabilizing intermolecular force (second term), and the destabilizing surface tension force (third term) controlled the fate of the instability. The spacing (λ_{avg}) between the droplets reported theoretically was obtained by evaluating the dominant growth coefficient (ω_m) using the condition, $\omega_{r,k} = 0$, where ω_r is the real part of ω [203],

$$\lambda_{avg} = 2\sqrt{2}\pi \left[\frac{1}{h_0^2} + \frac{A_e}{2\pi h_0^4 (\gamma_{ps} + mC)} \right]^{-1/2}. \tag{6.9}$$

The derivations, numerical solutions, integrations, and the subsequent calculations were done employing the commercial package Mathematica^{TM}.

6.4 Results and Discussion

6.4.1 The Phenomenon

The step (III) in Fig. 6.1 schematically shows that, initially, the PDMS substrate was placed in a petri dish before the 5CB LC drop was dispensed on the same. It may be noted here that the equilibrium contact angle of a 5CB droplet on a lyophobic PDMS substrate was ∼63° [203], which allowed a 5CB drop to form with a convex meniscus. Following this, the containers surrounding the substrate were filled with the solvent (e.g. hexane) before another petri dish was used to cover the experimental chamber from the top. Since hexane is a volatile solvent at room temperature, the experimental chamber was immediately filled with the solvent vapour, which started penetrating into the LC droplet.

Figs. 6.3(A – E) in the columns (I – III) show the three different pathways of film formation for the droplets having small, moderately large, and large sizes, respectively. Images in the column (I) show that when the drop was smaller (dia. 36 ± 0.5 μm), the solvent diffusion into the droplet matrix was fast to cause a NI phase transition, as shown by the cross-polarized micrographs in the insets of the images (IA) and (IB). Thereafter, as more solvent penetrated into the matrix, the droplet spread rapidly to form a film on the PDMS surface, shown by the Figs. 6.3(IC – IE). In this regard, it may be noted here that hexane is very well known for showing wetting behaviour on

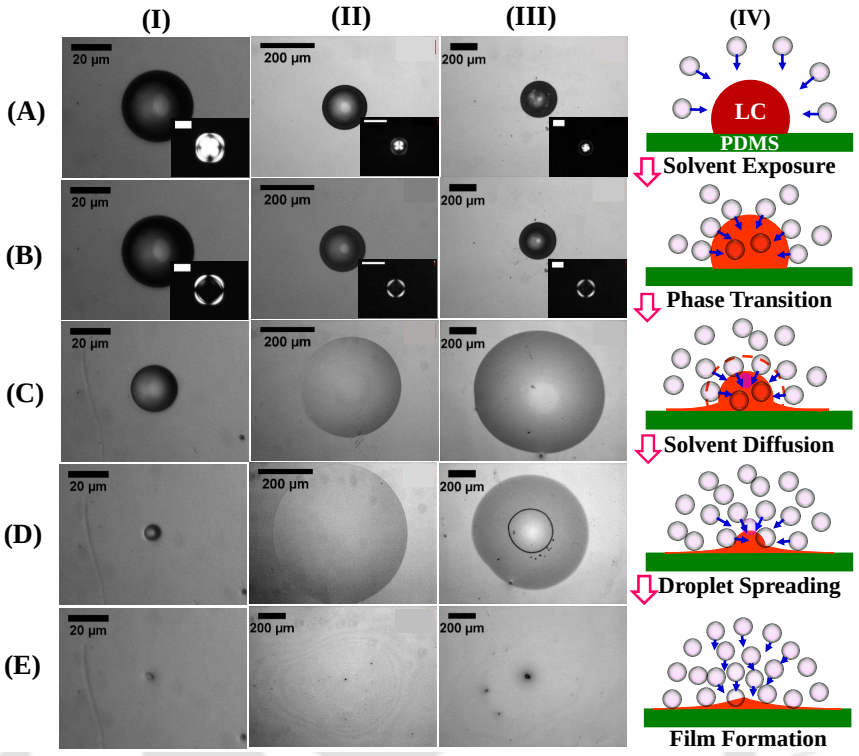

Figure 6.3: Optical micrographs in the columns (I – III) show the evolution of 5CB droplets of size 36 ± 0.5 μm, 167 ± 1 μm, and 209 ± 1 μm, respectively, under a solvent vapour exposure on a homogeneous PDMS substrate. The column (IV) schematically shows the different stages of the evolution as shown in the rows (A – E), solvent exposure, phase transition, solvent diffusion, droplet spreading, and film formation, respectively. The insets in the images of row (A) show that initially (t = 0 min) the 5CB drops were in the nematic state under the cross polarized microscopy. The insets in the images of row (B) shows the isotropic 5CB drops under the cross polarized microscopy after, t = 0.05 min, 0.2 min, and 0.3 min of solvent vapour exposure in the column (I – III), respectively. The images (IC – IE) were taken after, t = 2.36 min, 3.36 min, and 6.06 min of solvent exposure, respectively; images (IIC – IIE) were taken after, t = 10.45 min, 12.59 min, and 63.40 min of solvent exposure, respectively; and images (IIIC – IIIE) were taken after, t = 25.34 min, 29.18 min, and 120.00 min of solvent exposure, respectively.

the PDMS surfaces [208]. Thus, with progress in time, as the larger amount of solvent penetrated into the matrix, the equilibrium contact angle of the LC droplet reduced from ∼63° to form a film of solvent rich 5CB-hexane solution. The images suggest that, during the spreading stage, the solvent diffusion through the three-phase contact line was much faster than the diffusion of the solvent through the convex meniscus of the droplet. Thus, the 5CB-hexane droplet spread on the PDMS substrate through a fast spreading of the contact line while the meniscus shrunk progressively before forming a non-uniform of solvent rich 5CB film, as schematically depicted in the Figs. 6.3(IVA – IVE).

Comparing the diameters of the droplet meniscus in the Figs. 6.3(IB) and 6.3(IC), the droplet shrunk from 36 ± 0.5 μm to 23 ± 0.5 μm after t = 2.36 min, which was further

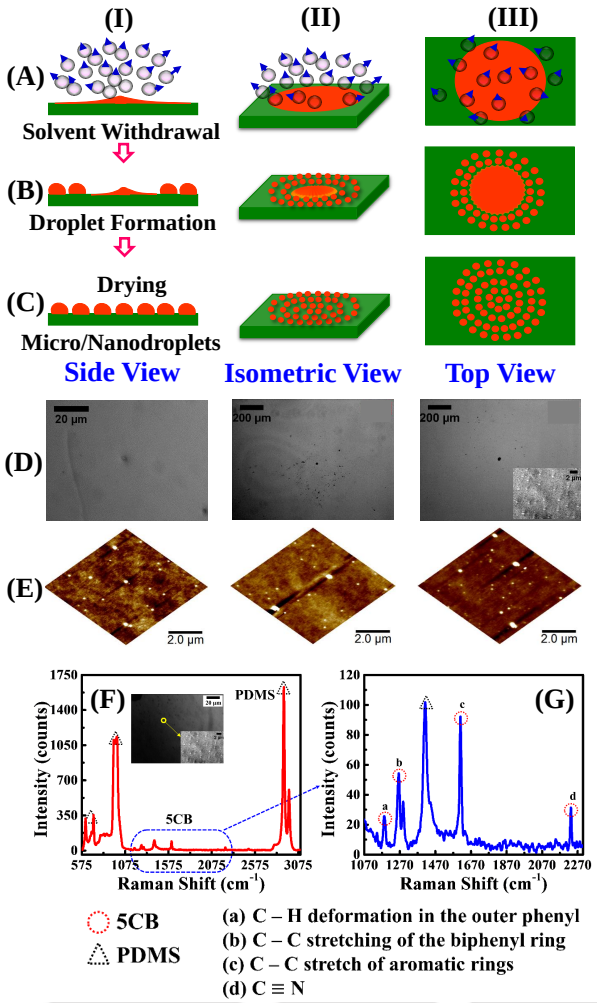

Figure 6.4: Schematic diagrams in the columns (I – III) show the side, isometric and top views of the stages of evolution of non-uniform 5CB-hexane film when the solvent vapour exposure was withdrawn. Images (A – C) schematically show solvent withdrawal, droplet and ring formation, and micro or nanodroplets formation stages after solvent evaporation, respectively. Optical micrographs (ID – IIID) and AFM images (IE – IIIE) correspond to the systems with initial droplet diameter 36 ± 0.5 μm, 167 ± 1 μm, and 209 ± 1 μm, respectively. The samples were dried under vacuum for 24 h at 24 ± 1°C. Inset of the image (IIID) shows submicron 5CB droplets under cross polarized microscopy. Image (F) shows Raman spectra of 5CB (circular symbols) and PDMS (triangular symbols) with optical micrograph on which the Raman spectra were recorded. The inset of optical micrograph in the image (F) shows sub-micron droplets on a homogeneous PDMS substrate. Image (G) shows magnified Raman spectra of corresponding to the peaks of 5CB.

reduced to about 8 ± 0.08 μm after $t = 3.36$ min (Fig. 6.3(ID)). Although the dissolution of the droplet meniscus was visible in the optical images, the spreading of the contact line and the formation of the non-uniform film were beyond the limit of optical characterization. The images suggested that the film was thicker near the central portion and thinner near the peripheries, a schematically depicted in the image (IVE).

Following this, when the solvent exposure was withdrawn from the experimental chamber, the film broke down into a collection of droplets as the solvent rapidly evaporated out from the film matrix under ambient condition. Schematic diagrams in the columns 6.4(I – III) show the side, isometric, and top views of the stages of evolution of solvent rich non-uniform 5CB-hexane film after the removal of solvent vapour exposure. Figs. 6.4(A – C) show different stages such as the solvent withdrawal, the contact line instabilities, and the formation of micro or nanodroplets, respectively. The images schematically show that the solvent evaporation was rapid from the thinner peripheral part of the 5CB-hexane film than the thicker central part. Subsequently, a rapid retraction of the contact line towards the centre of the droplet led to the instabilities near the retracting contact line to form a collection of microdroplets of the 5CB-hexane solution. Upon evaporation of solvent from matrix through 24 h drying at 24 ± 1.0°C, the microdroplets converted into a collection of 5CB nanodroplets, as shown in the optical micrograph 6.4(ID) and AFM Figs. 6.4(IE). Figs. 6.4(F) and 6.4(G) shows typical phenyl C-H, biphenyl C-C, and CN peaks of 5CB from Raman spectroscopy, which confirmed that the nanodroplets were indeed composed of LC materials [209].

The images in the column (II) of Fig. 6.3 show the stages of evolution of a moderately large droplet (dia. 167 ± 1 μm). In this case, initially, the solvent diffusion into the droplet matrix led to the NI transition (Figs. 6.3(IIA) and 6.3(IIB)) and understandably, the time taken for this process was larger than the smaller droplet in the column (I) due to the larger initial size. Importantly, as compared to the smaller droplet case where the spreading of the contact line was much faster than the solvent vapour diffusion through the droplet meniscus, in this case, both the phenomenon happened at a similar rate. In consequence, the droplet retained its lens like convex meniscus while expanding to form a non-uniform film, with the progressive expansion of contact-line and reduction of the contact angle with time, as shown by the Figs. 6.3(IIB – IIE). The spreading of the droplet with the convex meniscus had a diameter of 372 ± 0.54 μm after t = 10.45 min and 697 ± 0.36 μm after t = 13 min, as shown in the Figs. 6.3(IIC) and 6.3(IID). Again, as observed in the previous case, after the film formation was complete, the removal of the solvent broke the non-uniform film into a collection of randomly placed isotropic liquid droplets, as schematically shown in the Figs. 6.4(A – C) in the columns (I) –

(III). The droplets underwent IN phase transition upon further drying and the optical micrograph 6.4(IID) and AFM Figs. 6.4(IIE) confirmed the formation of the nanoscale droplets when the samples were dried for 24 h drying at 24 ± 1.0°C.

The images in the column (III) of Fig. 6.3 show the stages of evolution of a larger droplet (dia. 209 ± 1 μm), which was found to be even more sluggish than the previous cases. In this case, as observed for the previous cases, initially, the solvent diffusion into the droplet matrix led to the NI transition (Figs. 6.3(IIIA) and 6.3(IIIB)). The typical time taken for the NI transition of the 5CB droplets of the different size shown in the column 6.3(I – III) were found to be, t = 0.05 min, 0.2 min, and 0.3 min, respectively, which suggests that the kinetics of solvent absorption into bigger droplets were much slower. The Figs. 6.3(IIIB) and 6.3(IIIC) show that after the NI phase transition the drop initially spread following the pathway of the moderately large drop (column 6.3(II)) maintaining a broad convex meniscus. However, at the later stages, images (IIIC – IIIE) show that the meniscus progressively shrunk with time, as it was observed for the smaller droplets (column 6.3(I)). The spreading meniscus was found to be about 641.5 ± 1.5 μm after t = 25 min and 625 ± 0.5 μm after t = 29 min as shown in the Figs. 6.3(IIIC) and 6.3(IIID) whereas the shrinking meniscus was about 616.2 ± 2.2 μm and 460 ± 4.5 μm. Thus, at the initial stages, the spreading of the contact line and the solvent vapour diffusion to the droplet matrix were happening at almost similar rates. At the later stages of evolution, when the top part of the droplet was almost saturated with the solvent vapour, the contact line spread at a much faster rate to shrink the meniscus before forming the non-uniform film. The removal of the solvent source after the film formation again disintegrated the non-uniform film into a collection of randomly placed isotropic liquid droplets, which underwent IN phase transition upon further drying before forming micro or nanodroplets after 24 h drying at 24 ± 1.0°C, as shown in the optical micrograph 6.4(IIID) and AFM Figs. 6.4(IIIE).

We also performed control experiments where a dilute solution of LC was dispensed on the PDMS surface and allowed to rapidly evaporate, as shown Fig. 6.5. In such a scenario, the solvent evaporated from the droplet matrix to leave an array of micro-droplets of LC on the surface. Interestingly, upon drying the size and periodicity of these droplets were found to be much larger than the ones we obtained following the

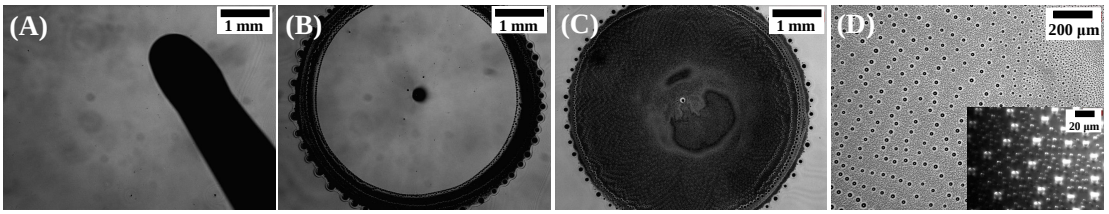

Figure 6.5: Optical images (A – D) show the generation of LC droplets by dispensing the 0.7% (w/v) of 5CB solution in hexane on PDMS substrate. Image (A) shows 2 μl drop dispensing by micro-pipette at $t = 0$ s. Image (B) shows generation LC droplets generation at $t = 5$ s. Images (C) shows film completely broke down into droplets at $t = 7$ s. Image (D) show magnified image of (C). Inset cross polarized images is magnified image of (D) with LC texture.

procedure described in Figs. 6.1, 6.3, and 6.4. The controlled exposure of the solvent vapour to convert the droplet into a film led to the formation of a much thinner film of LC-solvent solution than when a drop of the LC-solvent solution was dispensed on the PDMS surface. Subsequently, the rapid evaporation of the solvent from the thinner film matrix lad to the formation of much smaller LC droplets upon drying.

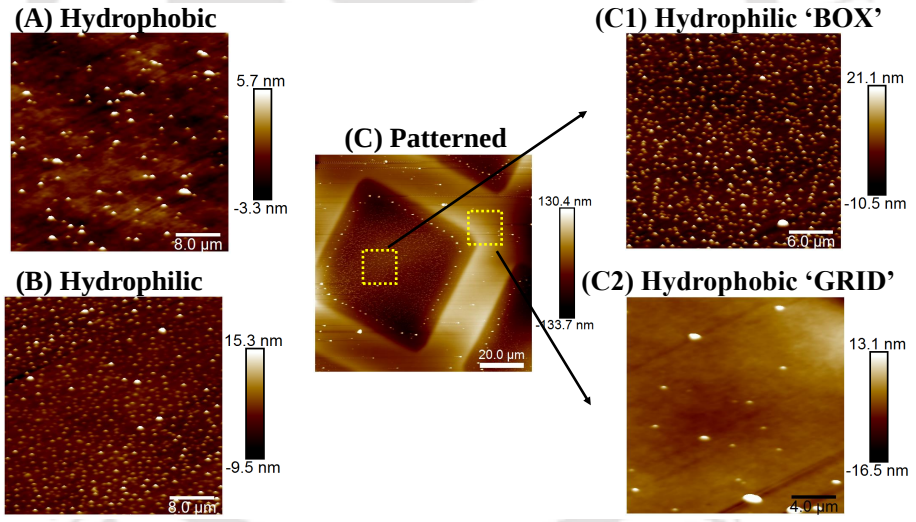

Figure 6.6: AFM images of (A – C) show 5CB droplets produced on the lyophobic, lyophilic, and physicochemically heterogeneous PDMS substrates, respectively, after 24 h drying at 24 ± 1.0°C. Image (A) shows that on the lyophobic PDMS substrate the average drop size was ∼209 ± 20 nm and average drop spacing was 1.18 ± 0.05 μm when the initial diameter of the drop size was, 60 ± 0.5 μm. Image (B) shows that on the lyophilic PDMS substrate the average drop size was 115 ± 10 nm and average drop spacing 600 ± 30 nm when the initial drop size was 72 ± 0.5 μm. Image (C) shows ordering of these nanostructures on a chemically patterned PDMS substrate when the initial drop diameter was, 180 ± 1 μm. Image (C1) and (C2) show magnified images of the marked zones of the image (C) at the lyophilic and lyophobic patches, respectively. In the image (C1) the average size and spacing of the droplets were 203 ± 25 nm and 332 ± 31 nm, respectively, while the same in the image (C2) were 373 ± 50 nm and 951 ± 50 nm, respectively.

Fig. 6.6 summarizes the typical size and spacing of the LC droplets formed on the lyophobic, lyophilic, and physicochemically heterogeneous PDMS substrates. The AFM

images were obtained after the experiments were complete and the samples were dried for 24 h in vacuum at 24 ± 1.0°C. Fig. 6.6A shows when a 60 ± 0.5 μm 5CB droplet was converted into a film through solvent exposure before disintegrating the film into droplets on a lyophobic PDMS substrate (contact angle ∼63°) the average diameter and spacing of the droplets were 209.67 ± 20 nm and 1.18 ± 0.05 μm, respectively. Importantly the average size and spacing of the droplets were brought down to 115 ± 10 nm and 600 ± 30 nm, when a 5CB droplet of initial diameter 72 ± 0.5 μm was converted into a film through solvent exposure on a lyophilic PDMS substrate before disintegrated into droplets through the withdrawal of the solvent exposure, as shown in the Fig. 6.6(B). It may be noted here that the contact angle of the 5CB decreased from ∼63° to ∼50° when the lyophobic PDMS surface was made more lyophilic through UVO exposure [203]. Thus, a thinner wetting film was formed on the more lyophilic surface than the lyophobic one, which upon disintegration could lead to closely spaced and smaller sized droplets.

Interestingly, a large area ordering could be imposed on these droplets when a physico-chemically heterogeneous PDMS surface with periodic patches of lyophobic "grid" and lyophilic "box" patterns was employed. Fig. 6.6(C) along with the magnified images (C1) and (C2) show that, when a droplet of diameter 180 ± 1 μm was disintegrated by synchronized solvent vapour exposure and its withdrawal, the lyophilic patch was populated with the droplets of average diameter and spacing of 203 ± 25 nm and spacing 332 ± 31 nm, respectively. In this situation, the 5CB droplets on the lyophobic grid zone had an average spacing of 951 ± 50 nm and an average diameter of 373 ± 50 nm. Notably, near the junction of the lyophobic and lyophilic patches, excellent ordering and pinning of the 5CB droplets were also observed in the Fig. 6.6(C). The AFM images in Fig. 6.6 shows that the proposed methodology could fabricate high density nanostructures of size as low as ∼100 nm and periodicity ∼600 nm. The experimental results shown so far suggested that the final size and the spacing of the droplets were dependent on the wettability of 5CB-solvent solution on the PDMS substrate and the initial diameter (D_I) of the 5CB droplet. Thus, we identified the influence of these parameters on the final average diameter (D_F), the number density (N_d), and the average spacing (λ_{avg}) between the droplets, as shown in the Fig. 6.7.

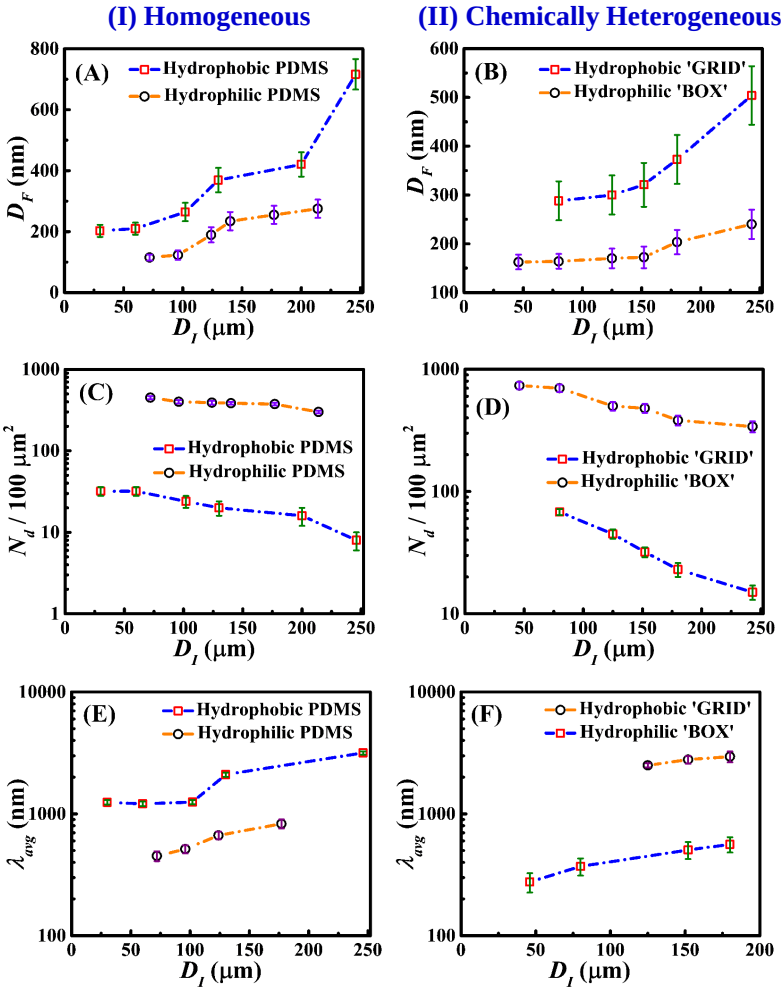

Figure 6.7: The plots (A) and (B) show the variations in average final diameter of droplets (D_F), plots (C) and (D) show the variations in the number of droplets per 100 μm^2 (N_d), and the plots (E) and (F) show the average spacing (λ_{avg}) between the droplets with the variation in the initial drop size (D_I) of 5CB. The plots on the left column (A, C and E) show the results for the homogeneous lyophobic and lyophilic substrates. The plots on the right column (B, D, and F) show the results on the chemically heterogeneous substrate.

Fig. 6.7(A) shows that the D_F was progressively reduced towards the nanoscale with the reduction in D_I. This is because, during the solvent exposure stage, a smaller 5CB droplet supplied lesser amount of 5CB materials to the 5CB-solvent solution, which eventually formed the non-uniform thin film of solvent rich 5CB-solvent solution. Thus, when the vapour source was withdrawn and the film was broken into microdroplets, they contained less amount of 5CB. Upon further drying of these microdroplets led to the formation of nanodroplets of size nearing 100 nm. The plot suggests that on the lyophobic PDMS substrate the D_F varied from 200 – 700 nm, however, on the lyophilic PDMS substrate D_F varied from 100 – 300 nm. Again, the smaller diameter on the lyophilic substrate could be attributed to the more spreading of the 5CB droplet on

lyophilic PDMS surface during the solvent vapour exposure, which eventually led to the formation of a thinner film than the lyophobic surface under identical experimental conditions. Consequently, when the solvent exposure was withdrawn, the thinner films on the lyophilic patches led to the formation of smaller drops of 5CB-solvent solution. The droplets shrunk further to the level of 100 nm diameter upon prolonged drying to remove solvent under vacuum. Figs. 6.7(C) and 6.7(E) suggest that the aforementioned reasons also led to the increase in the number of droplets per 100 μm^2 (N_d) and reduction in λ_{avg} on the lyophilic patches. The Figs. 6.7(B), 6.7(D) and 6.7(F) together show that similar degree of miniaturization and packing density of the 5CB droplets with ordering could achieve with the reduction in the D_I even on the chemically patterned PDMS substrate. For example, D_F was found to be in the range of 150 – 240 nm on the lyophilic surfaces while the same on the lyophobic was in the range of 288 – 504 nm. Concisely, the figure highlights the significance of the proposed methodology in generating a wide range of closely spaced nanoscale LC lenses with ordering.

6.4.2 Theoretical Explanation

The experimental results could be explained by the proposed theoretical model because (i) under prolonged exposure to the solvent vapour the 5CB droplet was converted into a Newtonian and incompressible film of dilute 5CB-solvent solution before the solvent source was withdrawn; and (ii) the breakup of the non-uniform thin film into droplet of the dilute LC solution could be envisaged as the dewetting of a thin film due to the rapid evaporation of solvent from the film.

We assumed that in the solvent rich state the film was of nearly microscale thickness while the stabilizing and destabilizing components of the curvature forces promoted the Plateau-Rayleigh instability near the retracting contact line. The effects of the intermolecular force and solutal Marangoni flow was also included as the other possible sources of this instability. The dispersion relation obtained from the linear stability analysis of the governing equations in the Equation (6.8) in the section 6.3.2.4 of the methods segment shows the components of the stabilizing and destabilizing components of the surface tension force (first and third terms on the right-hand side) and the

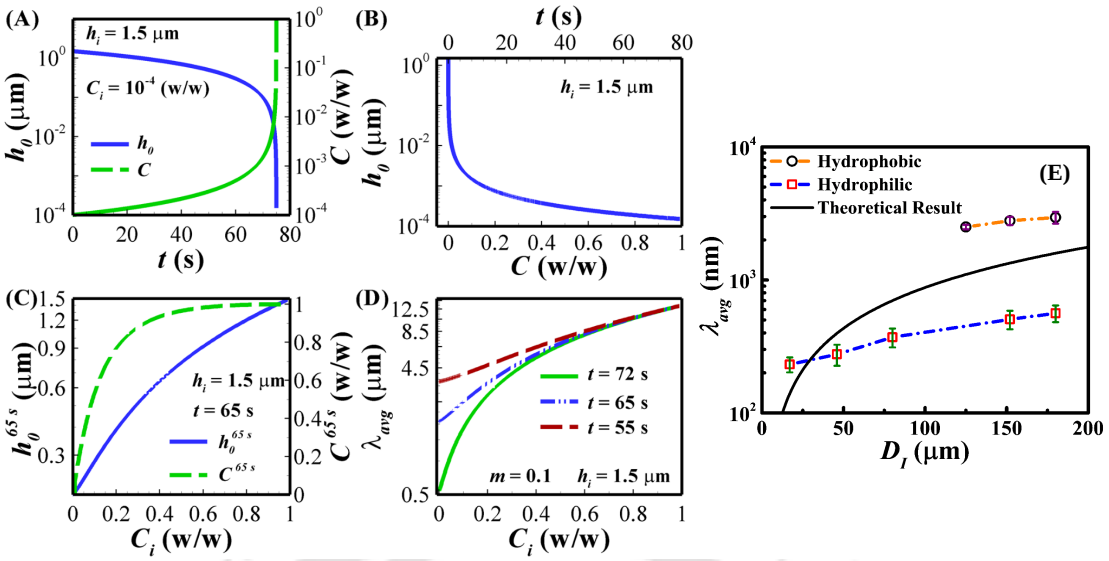

Figure 6.8: Plots (A – D) show the results obtained theoretically while plots (E) shows the comparison between the experimental and theoretical results. Plot (A) shows the variation of base state film thickness (h_0) and the LC loading in the solution (C in % w/w) with t and plot (B) shows the variation of h_0 with C at different t. Plot (C) shows the variation of $h_0 = h_0^{65s}$ and $C = C^{65s}$ after $t = 65$ s with the variation in the initial solute concentration, C_i. Plot (D) shows the variation of λ_{avg} with C_i. Plot (E) shows the comparison of λ_{avg} with h_i (experimentally defined as, D_I) from the experiments and theory when $C_i = 0.01$. The typical parameters employed for the calculations in the plots were, $e_0 = 2.0 \times 10^{-8}$ m/s, $\gamma = 26$ mN/m, $A_e = 1.82 \times 10^{-20}$ J, $m = 0.1$, $t = 65$ s.

destabilizing intermolecular force (second term). While making the qualitative comparison, we assumed that the interplay between these forces decided the spacing between the formation of the solvent rich isotropic 5CB droplets. We also assumed that although the droplets shrunk upon drying to obtain the nanoscale size, their periodicity did not change. The coupled ODEs in the Equations (6.4) and (6.5) in section 6.3.2.4 of the methods segment were solved simultaneously to obtain the variation in the average height of the film, h_0, and the concentration of the solute C, with time t, as shown in the plots 6.8(A) and 6.8(B). The theoretical parameters for these plots are optimized in such a manner that they were close to the experiments.

The plots 6.8(A) and 6.8(B) suggest that the solvent evaporated out from the films in two different phases. In the initial 'thinning' phase, a film of an initial average thickness of ∼1.5 μm steadily thinned to an average thickness of 100 nm at about 65 s due to rapid evaporation of the solvent with the marginal increase in the solute concentration. In the subsequent 'drop formation' phase, the 100 nm film thinned rapidly to ∼0.15 nm with an abrupt increase in the solute concentration, which could also be termed as

the dewetting phase. The parameters in the theoretical analysis were tuned in such a manner that the time required for the end (onset) of the thinning (dewetting) phase was ∼65 – 75 s, which was obtained from the experiments. Plot 6.8(C) depicts the variation of the average height of the film, $h_0 = h_0^{65}$ s, and concentration $C = C^{65}$ s, after $t = 65$ s with the variation in the initial solute concentration, C_i. The plot suggested that the film thickness reduced before dewetting with the reduction in the initial loading of the LC molecules as reduced with the reduction in C_i. The plot (D) suggests the variation in the theoretically predicted spacing between the droplets (λ_{avg}) with C_i at the different time intervals of the end (onset) of the thinning (dewetting) phase. The plot shows that the theoretical periodicity of the droplets reduced with the reduction in C_i as well as with the increase in the time intervals for the end (onset) of the thinning (dewetting) phase. In the plot 6.8(E), a comparison between the theoretical (solid line) and experimental (hollow symbols joined with a broken line) droplet spacing (λ_{avg}) was carried out with the initial diameter of the droplet, D_I, which was assumed to be the theoretical equivalent of, h_i. Again, in this case, the end (onset) of the thinning (dewetting) phase was maintained ∼65 s. The plot shows that with the increase in D_I, λ_{avg} increased as observed in the experiments for both the lyophilic and lyophobic zones.

6.4.3 Application

Fig. 6.9(A) shows the schematic diagram of experimental setup for the Lorentz force ($\mathbf{F} = \mathbf{J} \times \mathbf{B}$) induced self-propulsion of micro or nanoscale droplets. The configuration shown in these images emulate the typical electrowetting EWOD setup [210] with the exception of the presence of the magnetic field in the present study. In these experiments, initially, the 5CB micro or nanodroplets were generated on the lyophobic PDMS substrate through solvent exposure on a droplet of diameter 246 ± 1 μm followed by the removal of the solvent source. Following this, the magnetic field ($\mathbf{B}$) was generated across the system through a pair of bar magnets of strength 0.398 ± 0.01 T, as shown in the Fig. 6.9(A). Under the electric field exposure the droplets initially elongated to touch the top electrode due to the electrohydrodynamic stress generated at the LC-air interface, as schematically shown in the Fig. 6.9(A). This enabled a weak leakage current ($\mathbf{J}$) to pass through the elongated droplet, which touched the pair of bounding

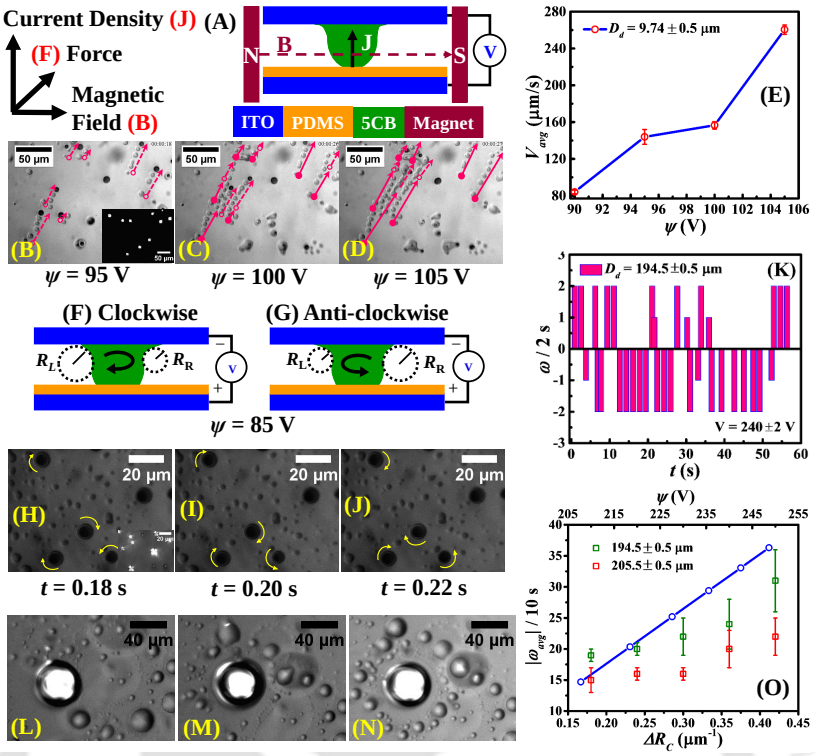

Figure 6.9: The schematic diagram (A) shows the experimental setup for the Lorentz force ($\mathbf{F} = \mathbf{J} \times \mathbf{B}$) induced locomotion of microdroplets on a PDMS substrate confined between a pair of ITO electrodes. The image (B) shows the motions of a droplets of average size, 9.45 ± 0.95 m at 95 ± 1 V; image (C) shows the motions of a droplets of average size, 9.305 ± 0.44 m at 100 ± 1 V; and image (D) shows the motions of a droplets of average size, 9.195 ± 0.32 m at 105 ± 1 V. In these experiments the magnetic field strength was 0.398 ± 0.01 T. The arrowhead and tail show the final and initial points while plot (E) shows the variation in the average velocity (V_{avg}) with the applied voltage (ψ) of the Lorentz force induced translational motion. Images (F) and (G) schematically show the electric field induced elongation and rotation (clockwise and anti-clockwise) of the LC droplets of diameter under the sole influence of the electric current (**J**). Images (H – J) show the top view of the experimental images when the droplet of diameter was diameter 8.96 ± 1.6 μm at 85 ± 2 V. Inset show the cross polarized microscope images of the rotating droplets. Plot (K) shows clock wise and anti-clock rotational speed of the droplet (ω / 2 s) with time (t) for a drop of diameter 194.5 ± 0.5 μm. Cross polarized optical images (L – N) show the satellite drop ejection of a 49 ± 0.2 μm droplet when the applied voltage was 150 ± 3 V and the magnetic field strength was 0.398 ± 0.01 T. Plot (O) shows variation in ω with difference in the theoretical (solid line) and experimental (symbols) radius of curvature $\Delta R_C = |1/R_R - 1/R_L|$ across the droplet when R_L or R_R was assumed to be, 0.5 μm, 1 μm, and 2 μm. The results are compared for different ψ for two different droplets, 194.5 ± 0.5 μm and 205.5 ± 0.5 μm. The typical thickness of the PDMS film was 1.2 ± 0.1 μm while the spacing between the top ITO electrode and PDMS was managed using dust particles.

PDMS and ITO electrodes upon expansion. Subsequently, the presence of the magnetic field generated adequate thrust for the droplet motion suppressing the friction on the bounding PDMS and ITO substrates.

The Figs. 6.9(B – D) show the motions of droplets of average size ∼9 – 9.5 μm when the applied voltages were 95 V, 100 V, and 105 V, respectively. The tails and the head of the arrows define the initial and the final position of the droplet. Plot (E) suggests

that the average speed (V_{avg}) of these droplets could be modulated from ∼8 to ∼24 body lengths per second with increasing strength of the Lorentz force due to increasing voltage (ψ). During the translation we also observed the droplet left some 'footprint' on the PDMS surface, as shown in the Figs. 6.9(B – D). A detailed analysis of this phenomenon uncovered that the droplet underwent random clock and anticlockwise motions while the translation took place. In a way, the translational motion was more of a "spiraling" motion wherein the droplet rotated randomly due to the electric field while translating due to the Lorentz force.

In order to uncover the origin of the rotational motion, we performed another set of experiments in which the magnetic influence was turned-off. The schematic diagrams in the Figs. 6.9(F) and 6.9(G), the experimental Figs. 6.9(H – J) show random rotational clock and anticlockwise motions of the microdroplets under the sole influence of the electric field field when the applied voltage was 85 ± 2 V. The clock and anti-clockwise rotational motions of the droplet could be explained by the asymmetric Laplace pressure gradient near the three phase contact line of the droplet confined between the lyophobic PDMS and lyophilic ITO surfaces, as schematically shown in the Figs. 6.9(F) and 6.9(G). It may be noted here that the equilibrium contact angle was acute on the ITO substrate while the same was obtuse on the PDMS substrate. The cross-polarized microscopy images as insets with the Figs. 6.9(H – J) confirmed that the droplets were indeed in the LC phase. The plot (K) shows the typical magnitudes of the rotational speed (ω) with time, t, under the sole influence of electric field.

The Figs. 6.9(F) and 6.9(G) suggest that, when the 5CB droplet was elongated to touch the top electrode under the exposure of a strong electric field, a difference in the radius of curvatures was generated towards the sides, R_L and R_R. Here the subscripts 'L' denotes left and 'R' denotes right side of the contact line, in a two-dimensional framework. The difference in the pressure across the interfaces could be obtained from the Young-Laplace equation as, $\Delta P_R = P_R - P_O = \gamma\left(\frac{1}{R} + \frac{1}{R_R}\right)$ and $\Delta P_R = P_L - P_O = \gamma\left(\frac{1}{R} + \frac{1}{R_L}\right)$ and, respectively, where γ is the surface tension, R is the transverse radius of curvature of the droplet, P_R is the pressure inside the droplet at the right side, P_L is the pressure inside the droplet at the left side and P_O is the atmospheric pressure. Thus, the net pressure difference ΔP_T between the left and right side of the droplet is, $\Delta P_T = |\Delta P_R - \Delta P_L| =$

$\gamma\left|\frac{1}{R_R}-\frac{1}{R_L}\right|$. We assumed that the pressure difference across the droplet created a torque, $\tau = R_D \times \Delta P_T \times A$, which helped in the droplet rotation. Here R_D was the radius of the droplet and A was the curved surface area of the droplet, which was assumed to be the curved surface area of a cylinder for the sake of simplicity. The angular acceleration of the droplet rotation was, $\alpha = \frac{d\omega}{dt} = \frac{\tau}{\rho \times v} = \left(\frac{R_D \gamma A}{\rho v}\right)\left|\frac{1}{R_R}-\frac{1}{R_L}\right|$, where ρ and v the density and volume of the droplet. Integrating the expression for the angular velocity we obtained the theoretical expression, $\omega = \left(\frac{R_D \gamma A}{\rho v}\right)\left|\frac{1}{R_R}-\frac{1}{R_L}\right| t$, which was plotted against the experimentally obtained rotational speed in the plot (O). The plots confirmed that a typical variation of the parameter, $\Delta R_C = \left|\frac{1}{R_R}-\frac{1}{R_L}\right|$, in the range of 0.1 – 0.4 μm could cause the rotational speed to vary ∼1 – 4 rps when the ψ varied from 200 – 250 V for the droplets of size 190 – 250 μm.

Importantly, under this condition when the magnetic field was re-introduced, at a much higher applied voltage, continuous ejection of satellite microdroplets surrounding the central microdroplet was observed, as shown in the cross polarized Figs. 6.9(L – N). In this situation, while the electric field induced the rotational motion to the LC droplet the Lorentz force helped in amplifying the same, which led to the ejection of the satellite droplets from the primary one when the centripetal force was larger than the cohesive force of the LC materials. The Lorentz force induced ejection of the droplets could be optically followed when the droplet size was ∼30 μm or higher and the applied voltage larger than ∼150 V wherein the rotational speed was found to be ∼350 rpm. Understandably, this speed was much higher than the sole influence of electric field, which led to the ejection of the droplets by the amplification of the centripetal force.

6.5 Summary

In this study, a single-step methodology was showed for fabrication of micro or nanoscale LC droplets by contact line instability of evaporating thin films. The summary of the study is,

(i) Initially, LC drop (30 – 250 μm) was placed on three different substrates chemically homogeneous lyophobic, chemically homogeneous lyophilic, and chemically

heterogeneous substrates. Later, they were exposed to solvent vapour before the LC drop spread on a substrate and form a non-uniform solvent rich LC film by solvent diffusion into the drop matrix.

(ii) A non-uniform film formation from a drop was varied on the initial LC drop size.

(iii) After a prolonged solvent exposure (2 – 5 h), when the solvent source was withdrawn from the experimental chamber then the solvent evaporates from film matrix. It engendered rapid retraction of the contact line towards the centre of the droplet led to the instabilities the retracting contact line to form a collection of microdroplets of the 5CB-hexane solution. Upon evaporation of solvent from matrix through 24 h drying, the microdroplets converted into a collection of 5CB nanodroplets.

(iv) The experiments where the dilute LC solution dispensing on the PDMS surface were found the drop size, spacing, and periodicity much larger than ones we obtained from controlled exposure and withdrawal of the solvent vapour.

(v) The experiments were done on the three different type of substrates, lyophobic-homogeneous, lyophilic-homogeneous, and chemically heterogeneous.

(vi) The LC nanodroplets size (D_d), average spacing (λ_{avg}) on lyophilic substrates found to be much smaller than the lyophobic substrates. Interestingly, a large area ordering could be imposed on these droplets when a physicochemically heterogeneous PDMS surface with periodic patches of lyophobic "grid" and lyophilic "box" patterns was employed.

(vii) The linear stability analysis of a theoretical model representing an evaporating thin film composed of a solution of an LC solute and a volatile solvent qualitatively showed that the spacing of the droplets was decided by the interplay between the stabilizing and destabilizing components of the capillary forces for relatively thicker films. The van der Waals interaction was found to play a supportive role when the thickness of the LC-solvent film was less than 100 nm.

(viii) When the miniaturized droplets were brought under the exposure of an external electric field, an anomalous oscillatory rotational motion was observed originating from the difference in the Laplace pressure around the contact line.

(ix) Interestingly, application of Lorentz force to these droplets showed exciting translational and rotations motions followed by ejection of miniaturized droplets.

(x) The proposed pathways can be employed to fabricate an array of nanoscale lenses of LC under ambient conditions, which can be of lead to futuristic nanoscale locomotives, display, oscillators, rotors, optical, electronic, and energy harvesting devices.

6.6 Acknowledgements

The help during the experiments from Mr. Mitradip Bhattacharjee and the support during the theoretical modeling from Mr. Abir Ghosh are gratefully acknowledged.

Chapter 7

Conclusions and Scope for the Future Work

7.1 Conclusions

In this thesis, we were able to generate micro or nanodroplets in a new, simple, and cost-effective way by exploiting the self-organized instabilities of ultrathin polymer films and liquid crystal droplets. We also showed few simple applications by using this generated micro or nanodroplets. Finally, some important conclusions were drawn from this study, those are,

7.1.1 Pattern Directed Dewetting of Ultrathin Polymer Films to Fabricate Ordered Nanostructures

- First time we show that, instead of using a physical or chemical patterns on a substrate, the use of physicochemical patterns could guide the formation of sub-micron patterns employing the self-organized dewetting of thin polymeric films.
- The dewetting on the PDMS substrates loaded with discrete and closely packed AuNPs led to the hole formation near the physicochemical defects, which eventually controlled the size and the spacing of the droplets formed.
- The size and spacing of the holes and the droplets could be tuned by varying the nanoparticle loading on the PDMS substrate.
- Interestingly, as compared to the dewetting of PS films on the homogeneous PDMS surfaces, the AuNP guided patterns show a tenfold miniaturization.

- Further, use of pre-patterned physicochemical substrate could impose a long-range order to the dewetted patterns to develop a gradient surface.

- The results shown here can be of significance in the fabrication of high-density nanostructures exploiting the self-organized instabilities of thin polymers films on the physicochemically patterned surfaces.

7.1.2 Solvent Vapour Mediated Spontaneous Healing of Self-Organized Defects of Liquid Crystal Films

- The phase transition of ultrathin nematic film can also be done by solvent annealing at room temperature.

- The transitions were accompanied by the appearance and fading of surface patterns as the solvent destroyed (restored) the orientational order while diffusing into (out of) the film. The experiments confirmed that solvent exposure could act as an analogue to thermal annealing in ambient conditions.

- A prolonged solvent vapour annealing led to the dewetting of the nematic film following the NI transition.

- During this stage, removing the solvent exposure led to an exciting fingering instability at the contact line, surrounding the dewetted zones. The change in contact angle due to phase transition coupled with the imbalance of osmotic pressure due to the differential rate of solvent evaporation across the contact line helped the fingers to grow towards the centre of the hole.

- The fingers grew with time to attain structures with significantly high aspect-ratio and branching patterns, which nearly self-healed the dewetted zones.

- Interestingly, even at this stage, the growth of the fingers could be arrested and dewetting could be resumed by introducing solvent vapour exposure.

- The formation of the nematic fingers upon withdrawal of the solvent exposure and the removal of the fingers through the dewetting of the films upon solvent vapour annealing were found to be a quasi-reversible process.

- The characteristics of the fingering instability observed for the nematic ultrathin films in the present study were very different from the same originated due to the osmotic pressure imbalance during the spreading of a droplet loaded with surfactants [199, 211].

- The results reported here show the potential for future developments of futuristic vapour sensors and self-healing coatings using LC thin films.

7.1.3 Pattern Directed Phase Transition of the Nematic, Smectic, and Crystal State Ultrathin Films

- The solvent vapour mediated phase transitions from the crystalline or semctic phases to the nematic phases as well as the nematic phases to the isotropic phase have been shown at room temperature. The reverse phase transitions from isotropic to nematic phase and from nematic to the crystalline or smectic phases have also been shown upon the withdrawal of the solvent vapour source. The transitions were found to be repeatable with the periodic exposure and the withdrawal of the solvent and found to be very similar to the thermal annealing with the exception that the entire processes could be performed under ambient conditions.

- Emulating the LC thermometers, we showed that a thin film resting on a solid substrate could be employed to measure the vapour pressure and volatility of different aromatic and non-aromatic solvents. For this purpose, a linear correlation was identified between the time for nematic to isotropic phase transition during the exposure of the different solvent vapours with the vapour pressure and volatility of the solvents.

- The solvent annealed phase transition behaviours of a LC-DAuNP composite droplet was converted into an electrical signal with the help of an external circuit. The electrical resistance was found to reduce (increase) upon the destruction (restoration) of the orientational order of the droplet. The setup could be employed to sense the presence and absence of different volatile organic vapours, phase transition of LC materials, evaluation of the order parameter of an LC material during

phase transition, rate of diffusion and absorption of a solvent into a LC matrix, and the rate of evaporation of a solvent from a LC matrix.

- In addition, the solvent annealed phase transition of the LC materials on the physically and chemically heterogeneous surfaces show a pattern directed phase transition. While in the physically heterogeneous surface the variations in the thicknesses ensured that the nematic to isotropic phase transition was faster at the thinner regimes, in the chemically heterogeneous surfaces the weaker anchoring of the LC molecules on the lyophobic patches ensured a faster nematic to isotropic transition during the solvent vapour exposure. These observations could easily be exploited to develop LC based devices to identify the physical or chemical defects on the surfaces alongside the measurement of the lyophobicity or lyophilicity.

- We have identified a rate parameter ϕ, which is the ratio of the rate of destruction and restoration of the orientational order of LC molecule, is substantiated as the ratio of the rate absorption to desorption of solvent molecule. For a uniform LC film this rate parameter ϕ has different values for different solvents. In case of a LC film on a chemically patterned substrate undergoing solvent annealing, $\phi > 1$ for lyophobic patch whereas $\phi < 1$ for lyophilic region.

- The study shows a host of interesting scientific phenomenon, which could be employed in future to develop prototypes to identify volatile organic matters, vapour pressure or volatility of solvents, and surface properties such as the defects or the lyophobicity, among others.

7.1.4 Pattern Directed Ordering of Spin-Dewetted Liquid Crystal Micro or Nanodroplets

- Here we showed a simple and economic top-down methodology to fabricate an array of ordered and high-density micro or nanodroplets of LC materials, which can stage a paradigm shift in the development of futuristic display devices.

- Spin-dewetting of a droplet of a dilute 5CB-organic solution on a chemically patterned PDMS substrate formed an ordered array of microdoplets. Evaporation of

the solvent and 5CB from these microdroplets could miniaturize the size to the sub-100-nm regime to form well-organized nanoscale digitized 5CB droplets.

- The size, periodicity, and spacing of these mesoscale droplets could be tuned with the variations in the initial LC loading in the organic solution and the strength of the centripetal force with the change in rotational speed of the spin-coater.
- The miniaturized 5CB droplets showed reversible phase transitions from nematic to isotropic and vice versa with the periodic exposure and removal of the solvent vapour or with the periodic increase or reduction in temperature, suggesting the usefulness of these miniaturized droplets as vapour or temperature sensor.
- When these microdroplets were confined between a pair of electrodes and an external electric field was applied, they showed pixelated light-reflecting properties under the polarization microscopy, highlighting their importance in the development of micro or nanoscale LC displays.
- In addition, the digitized LC droplets, which were stationary otherwise, showed interesting dielectrophoretic locomotion restricted to the lyophilic zone under the influence of the externally applied electric field.
- The findings could significantly contribute in the development of futuristic vapour or temperature sensors, miniaturized light reflectors, masks for lithographic methodologies, and self-propellers employing the micro or nanoscale digitized LC droplets. The spin-dewetted droplets on a chemically patterned surface could also be employed for large-area patterning of surfaces in a roll-to-roll format, which may usher in novel ways for soft lithographic printing.

7.1.5 Solvent Vapour Mediated Contact Line Instabilities of Liquid Crystal Droplets

- The proposed pathway could easily destroy the orientational order of an LC microdroplet placed on a PDMS substrate to form a film at room temperature upon solvent vapour annealing before rapidly disintegrating into a collection of LC microdroplets upon the withdrawal of the solvent exposure. Rapid evaporation of

the solvent from the film matrix followed by drying not only restricted the coalescence of the mesoscale structures formed but also helped to obtain LC droplets of nanoscale size and periodicity.

- The solvent exposure to the droplet allowed rapid spreading due to the reduction in the equilibrium contact angle with the solvent absorption in the drop matrix. Further, evaporation of the solvent after the withdrawal of the solvent exposure engendered rapid retraction of the contact-line owing to the increase in the equilibrium contact angle. Subsequently, an uncommon contact-line instability near the contact line engendered the formation of the droplets of LC-solvent solution. The microdroplets further shrunk to the nanoscale size and periodicity upon drying.

- The droplet size and periodicity was found to be lesser (higher) on the lyophilic (lyophobic) surfaces because the average thickness of the non-uniform film of the LC-solvent solution was much thinner (thicker) during the prolonged solvent exposure phase. Further, a smaller LC microdroplet led to the formation of nanodroplets owing to the less loading of the LC materials into the film during the solvent exposure and droplet spreading phase. A large area order to these patterns could be imposed when the droplets were simultaneous spread and dewetted a physicochemically patterned PDMS substrate.

- The linear stability analysis of a theoretical model representing an evaporating thin film composed of a solution of an LC solute and a volatile solvent qualitatively showed that the spacing of the droplets was decided by the interplay between the stabilizing and destabilizing components of the capillary forces for relatively thicker films. The van der Waals interaction was found to play a supportive role when the thickness of the LC-solvent film was less than 100 nm.

- When the miniaturized droplets were brought under the exposure of an external electric field, an anomalous oscillatory rotational motion was observed originating from the difference in the Laplace pressure around the contact line. Interestingly, application of Lorentz force to these droplets showed exciting translational and rotations motions followed by ejection of miniaturized droplets.

- The proposed pathways can be employed to fabricate an array of nanoscale lenses of LC under ambient conditions, which can be of lead to futuristic nanoscale locomotives, display, oscillators, rotors, optical, electronic, and energy harvesting devices.

7.2 Scope for the Future Work

- Enhancing the self-organized instabilites by placing physicochemical defects underneath the film can be carried further by using, superlyophilic substrates. Also the dewetting of simple polymers can be further extended to conductive polymers, liquid crystal polymers, and functional polymers.
- The studies on the self-healing of the LC materials under solvent vapour annealing can be extended to different other LC materials such as the discotic or smectic or polymeric LCs.
- The response of the nematic LC materials under various solvent exposure can be extended to develop vapour sensors.
- The studies on the spin-dewetting can be extended to different other LC materials such as the discotic or smectic or polymeric LCs.
- The micro and nanaoscale lenses fabricated employing the spin-dewetting and the LC droplet breakup can be extended for the commercial production of micro or nanolenses compose of LCs.
- The studies on the breakup of the droplets under solvent vapour annealing can be extended to different other LC materials such as the discotic or smectic or polymeric LCs.
- Behaviour of the micro or nanoscale LC droplets under electric and magnetic fileds study can be further extended to different other LC materials such as discotic or smectic or polymeric LCs.

- The theoretical modeling of evaporating liquid crystal contact line instability can be extended further to different other LC materials such as discotic or smectic or polymeric LCs.

References

[1] W. Knoll and R. C. Advincula, *Functional Polymer Films, Volume 2*. John Wiley & Sons, 2013.

[2] A. Sharma and E. Ruckenstein, "An analytical nonlinear theory of thin film rupture and its application to wetting films," *Journal of Colloid and Interface Science*, vol. 113, no. 2, pp. 456–479, 1986.

[3] H. A. Macleod, "Thin film optical coatings," in *Technology of Stratified Media*, vol. 387. International Society for Optics and Photonics, 1983, pp. 28–36.

[4] W.-L. Min, B. Jiang, and P. Jiang, "Bioinspired self-cleaning antireflection coatings," *Advanced Materials*, vol. 20, no. 20, pp. 3914–3918, 2008.

[5] C.-F. Zheng, Z.-F. Yang, C.-C. Lv, X.-P. Zhou, and X.-L. Xie, "Thermal stability and abrasion resistance of polyacrylate/nano-silica hybrid coatings," *Iranian Polymer Journal*, vol. 22, no. 7, pp. 465–471, 2013.

[6] S. Stavroyiannis, I. Panagiotopoulos, D. Niarchos, J. A. Christodoulides, Y. Zhang, and G. C. Hadjipanayis, "Copt/ag nanocomposites for high density recording media," *Applied Physics Letters*, vol. 73, no. 23, pp. 3453–3455, 1998.

[7] W. M. Gibbons, P. J. Shannon, S.-T. Sun, and B. J. Swetlin, "Surface-mediated alignment of nematic liquid crystals with polarized laser light," *Nature*, vol. 351, no. 6321, pp. 49–50, 1991.

[8] P. Fu, Q. Shan, Y. Shang, J. Song, H. Zeng, Z. Ning, and J. Gong, "Perovskite nanocrystals: Synthesis, properties and applications," *Science Bulletin*, 2017.

[9] J.-P. Correa-Baena, M. Saliba, T. Buonassisi, M. Grätzel, A. Abate, W. Tress, and A. Hagfeldt, "Promises and challenges of perovskite solar cells," *Science*, vol. 358, no. 6364, pp. 739–744, 2017.

[10] A. Patil, V. Patil, J.-W. Choi, J.-S. Kim, and S.-J. Yoon, "Solid electrolytes for rechargeable thin film lithium batteries: A review," *Journal of Nanoscience and Nanotechnology*, vol. 17, no. 1, pp. 29–71, 2017.

[11] V. L. Patil, S. A. Vanalakar, P. S. Patil, and J. H. Kim, "Fabrication of nanostructured zno thin films based no2 gas sensor via silar technique," *Sensors and Actuators B: Chemical*, vol. 239, pp. 1185–1193, 2017.

[12] P. A. Nistor and P. W. May, "Diamond thin films: Giving biomedical applications a new shine," *Journal of the Royal Society Interface*, vol. 14, no. 134, p. 20170382, 2017.

[13] P. G. de Gennes, "Wetting: Statics and dynamics," *Reviews of Modern Physics*, vol. 57, no. 3, p. 827, 1985.

[14] A. Scheludko, "Advances in colloid and interf," *Science*, vol. 1, p. 391, 1967.

[15] A. Vrij, "Possible mechanism for the spontaneous rupture of thin, free liquid films," *Discussions of the Faraday Society*, vol. 42, pp. 23–33, 1966.

[16] L. L. Schramm and F. Wassmuth, "Foams: Basic principles." ACS Publications, 1994.

[17] T. P. Russell, "X-ray and neutron reflectivity for the investigation of polymers," *Materials Science Reports*, vol. 5, no. 4, pp. 171–271, 1990.

[18] R. A. L. Jones, L. J. Norton, E. J. Kramer, R. J. Composto, R. S. Stein, T. P. Russell, A. Mansour, A. Karim, G. P. Felcher, and M. H. Rafailovich, "The form of the enriched surface layer in polymer blends," *Europhysics Letters*, vol. 12, no. 1, p. 41, 1990.

[19] A. Ghatak, R. Khanna, and A. Sharma, "Dynamics and morphology of holes in dewetting of thin films," *Journal of Colloid and Interface Science*, vol. 212, no. 2, pp. 483–494, 1999.

[20] R. C. Jaeger, "Film deposition," *Introduction to Microelectronic Fabrication*, 2002.

[21] R. Behrisch and K. Wittmaack, *Sputtering by Particle Bombardment.* Springer Berlin, 1981, vol. 1.

[22] R. L. Grimm, "Fundamental studies of the mechanisms and applications of field-induced droplet ionization mass spectrometry and electrospray mass spectrometry," Ph.D. dissertation, California Institute of Technology, 2006.

[23] A. Cho and J. Arthur, "Molecular beam epitaxy," *Progress in Solid State Chemistry*, vol. 10, pp. 157–191, 1975.

[24] N. Kanani, *Electroplating: Basic Principles, Processes and Practice.* Elsevier, 2004.

[25] K. Ariga, Y. Yamauchi, T. Mori, and J. P. Hill, "25th anniversary article: What can be done with the langmuir-blodgett method? recent developments and its critical role in materials science," *Advanced Materials*, vol. 25, no. 45, pp. 6477–6512, 2013.

[26] D. A. H. Hanaor, G. Triani, and C. C. Sorrell, "Morphology and photocatalytic activity of highly oriented mixed phase titanium dioxide thin films," *Surface and Coatings Technology*, vol. 205, no. 12, pp. 3658–3664, 2011.

[27] M. Faustini, G. L. Drisko, C. Boissiere, and D. Grosso, "Liquid deposition approaches to self-assembled periodic nanomasks," *Scripta Materialia*, vol. 74, pp. 13–18, 2014.

[28] K. F. Jensen, "Chemical vapor deposition." ACS Publications, 1989.

[29] R. L. Puurunen, "Surface chemistry of atomic layer deposition: A case study for the trimethylaluminum/water process," *Journal of Applied Physics*, vol. 97, no. 12, p. 9, 2005.

[30] R. K. Jain, I. B. Ivanov, C. Maldarelli, and E. Ruckenstein, "Instability and rupture of thin liquid films," in *Dynamics and Instability of Fluid Interfaces*. Springer, 1979, pp. 140–167.

[31] G. Reiter, "Dewetting of thin polymer films," *Physical Review Letters*, vol. 68, no. 1, p. 75, 1992.

[32] R. Xie, A. Karim, J. F. Douglas, C. C. Han, and R. A. Weiss, "Spinodal dewetting of thin polymer films," *Physical Review Letters*, vol. 81, no. 6, p. 1251, 1998.

[33] M. D. Morariu, E. Schäffer, and U. Steiner, "Molecular forces caused by the confinement of thermal noise," *Physical Review Letters*, vol. 92, no. 15, p. 156102, 2004.

[34] J. K. Bal, T. Beuvier, A. B. Unni, E. A. Chavez Panduro, G. Vignaud, N. Delorme, M. S. Chebil, Y. Grohens, and A. Gibaud, "Stability of polymer ultrathin films (< 7 nm) made by a top-down approach," *ACS Nano*, vol. 9, no. 8, pp. 8184–8193, 2015.

[35] G. Reiter, "Unstable thin polymer films: Rupture and dewetting processes," *Langmuir*, vol. 9, no. 5, pp. 1344–1351, 1993.

[36] A. Sharma and E. Ruckenstein, "Energetic criteria for the breakup of liquid films on nonwetting solid surfaces," *Journal of Colloid and Interface Science*, vol. 137, no. 2, pp. 433–445, 1990.

[37] A. Sharma and R. Khanna, "Pattern formation in unstable thin liquid films under the influence of antagonistic short-and long-range forces," *The Journal of Chemical Physics*, vol. 110, no. 10, pp. 4929–4936, 1999.

[38] J. Becker, G. Grün, R. Seemann, H. Mantz, K. Jacobs, K. R. Mecke, and R. Blossey, "Complex dewetting scenarios captured by thin-film models," *Nature Materials*, vol. 2, no. 1, pp. 59–63, 2003.

[39] A. Vrij and J. T. G. Overbeek, "Rupture of thin liquid films due to spontaneous fluctuations in thickness," *Journal of the American Chemical Society*, vol. 90, no. 12, pp. 3074–3078, 1968.

[40] R. K. Jain and E. Ruckenstein, "Stability of stagnant viscous films on a solid surface," *Journal of Colloid and Interface Science*, vol. 54, no. 1, pp. 108–116, 1976.

[41] M. B. Williams and S. H. Davis, "Nonlinear theory of film rupture," *Journal of Colloid and Interface Science*, vol. 90, no. 1, pp. 220–228, 1982.

[42] A. Sharma and E. Ruckenstein, "Mechanism of tear film rupture and formation of dry spots on cornea," *Journal of Colloid and Interface Science*, vol. 106, no. 1, pp. 12–27, 1985.

[43] C. J. Van Oss, M. K. Chaudhury, and R. J. Good, "Interfacial lifshitz-van der waals and polar interactions in macroscopic systems," *Chemical Reviews*, vol. 88, no. 6, pp. 927–941, 1988.

[44] A. Sharma, "Relationship of thin film stability and morphology to macroscopic parameters of wetting in the apolar and polar systems," *Langmuir*, vol. 9, no. 3, pp. 861–869, 1993.

[45] A. Sharma and G. Reiter, "Instability of thin polymer films on coated substrates: Rupture, dewetting, and drop formation," *Journal of Colloid and Interface Science*, vol. 178, no. 2, pp. 383–399, 1996.

[46] L. Rayleigh, "On the instability of jets," *Proceedings of the London Mathematical Society*, vol. 1, no. 1, pp. 4–13, 1878.

[47] T. G. Stange, D. F. Evans, and W. A. Hendrickson, "Nucleation and growth of defects leading to dewetting of thin polymer films," *Langmuir*, vol. 13, no. 16, pp. 4459–4465, 1997.

[48] U. Thiele, M. G. Velarde, and K. Neuffer, "Dewetting: Film rupture by nucleation in the spinodal regime," *Physical Review Letters*, vol. 87, no. 1, p. 016104, 2001.

[49] U. Thiele, L. Brusch, M. Bestehorn, and M. Bär, "Modelling thin-film dewetting on structured substrates and templates: Bifurcation analysis and numerical simulations," *The European Physical Journal E: Soft Matter and Biological Physics*, vol. 11, no. 3, pp. 255–271, 2003.

[50] A. Sehgal, D. Bandyopadhyay, K. Kargupta, A. Sharma, and A. Karim, "From finite-amplitude equilibrium structures to dewetting in thin polymer films on chemically patterned substrates," *Soft Matter*, vol. 8, no. 40, pp. 10 394–10 402, 2012.

[51] M. Asgari and A. Moosavi, "Interaction of 3d dewetting nanodroplets on homogeneous and chemically heterogeneous substrates," *Journal of Physics: Condensed Matter*, vol. 26, no. 22, p. 225001, 2014.

[52] R. Seemann, S. Herminghaus, and K. Jacobs, "Dewetting patterns and molecular forces: A reconciliation," *Physical Review Letters*, vol. 86, no. 24, p. 5534, 2001.

[53] C. Neto, K. Jacobs, R. Seemann, R. Blossey, J. Becker, and G. Grün, "Satellite hole formation during dewetting: Experiment and simulation," *Journal of Physics: Condensed Matter*, vol. 15, no. 19, p. 3355, 2003.

[54] R. Mukherjee, D. Bandyopadhyay, and A. Sharma, "Control of morphology in pattern directed dewetting of thin polymer films," *Soft Matter*, vol. 4, no. 10, pp. 2086–2097, 2008.

[55] B. Yoon, H. Acharya, G. Lee, H.-C. Kim, J. Huh, and C. Park, "Nanopatterning of thin polymer films by controlled dewetting on a topographic pre-pattern," *Soft Matter*, vol. 4, no. 7, pp. 1467–1472, 2008.

[56] S. Roy, D. Biswas, N. Salunke, A. Das, P. Vutukuri, R. Singh, and R. Mukherjee, "Control of morphology in pattern directed dewetting of a thin polymer bilayer," *Macromolecules*, vol. 46, no. 3, pp. 935–948, 2013.

[57] F. Ruffino and M. G. Grimaldi, "Self-organized patterned arrays of au and ag nanoparticles by thickness-dependent dewetting of template-confined films," *Journal of Materials Science*, vol. 49, no. 16, pp. 5714–5729, 2014.

[58] N. Bhandaru, A. Das, and R. Mukherjee, "Confinement induced ordering in dewetting of ultra-thin polymer bilayers on nanopatterned substrates," *Nanoscale*, vol. 8, no. 2, pp. 1073–1087, 2016.

[59] A. Sehgal, V. Ferreiro, J. F. Douglas, E. J. Amis, and A. Karim, "Pattern-directed dewetting of ultrathin polymer films," *Langmuir*, vol. 18, no. 18, pp. 7041–7048, 2002.

[60] J. H. Wei, D. C. Coffey, and D. S. Ginger, "Nucleating pattern formation in spin-coated polymer blend films with nanoscale surface templates," *Journal of Physical Chemistry B*, vol. 110, no. 48, pp. 24 324–24 330, 2006.

[61] G. G. Baralia, C. Filiâtre, B. Nysten, and A. M. Jonas, "Nanodecoding by dewetting," *Advanced Materials*, vol. 19, no. 24, pp. 4453–4459, 2007.

[62] D. Julthongpiput, W. Zhang, J. F. Douglas, A. Karim, and M. J. Fasolka, "Pattern-directed to isotropic dewetting transition in polymer films on micropatterned surfaces with differential surface energy contrast," *Soft Matter*, vol. 3, no. 5, pp. 613–618, 2007.

[63] M. Ghezzi, S. C. Thickett, and C. Neto, "Early and intermediate stages of guided dewetting in polystyrene thin films," *Langmuir*, vol. 28, no. 27, pp. 10 147–10 151, 2012.

[64] R. Mukherjee and A. Sharma, "Instability, self-organization and pattern formation in thin soft films," *Soft Matter*, vol. 11, no. 45, pp. 8717–8740, 2015.

[65] Z. Li, M. Tolan, T. Höhr, D. Kharas, S. Qu, J. Sokolov, M. H. Rafailovich, H. Lorenz, J. P. Kotthaus, and J. Wang, "Polymer thin films on patterned si surfaces," *Macromolecules*, vol. 31, no. 6, pp. 1915–1920, 1998.

[66] S. Roy, K. J. Ansari, S. S. K. Jampa, P. Vutukuri, and R. Mukherjee, "Influence of substrate wettability on the morphology of thin polymer films spin-coated on topographically patterned substrates," *ACS Applied Materials & Interfaces*, vol. 4, no. 4, pp. 1887–1896, 2012.

[67] N. Bhandaru, A. Das, N. Salunke, and R. Mukherjee, "Ordered alternating binary polymer nanodroplet array by sequential spin dewetting," *Nano Letters*, vol. 14, no. 12, pp. 7009–7016, 2014.

[68] M. Geoghegan, C. Wang, N. Rehse, R. Magerle, and G. Krausch, "Thin polymer films on chemically patterned, corrugated substrates," *Journal of Physics: Condensed Matter*, vol. 17, no. 9, p. S389, 2005.

[69] K. Kargupta and A. Sharma, "Templating of thin films induced by dewetting on patterned surfaces," *Physical Review Letters*, vol. 86, no. 20, p. 4536, 2001.

[70] F. Brochard-Wyart and C. Redon, "Dynamics of liquid rim instabilities," *Langmuir*, vol. 8, no. 9, pp. 2324–2329, 1992.

[71] B. M. Besancon and P. F. Green, "Moving fronts in entangled polymeric films," *Physical Review E*, vol. 70, no. 5, p. 051808, 2004.

[72] S.-H. Choi and B.-m. Zhang Newby, "Dynamic contact angle in rim instability of dewetting holes," *The Journal of Chemical Physics*, vol. 124, no. 5, p. 054702, 2006.

[73] M. Oron, T. Kerle, R. Yerushalmi-Rozen, and J. Klein, "Persistent droplet motion in liquid-liquid dewetting," *Physical Review Letters*, vol. 92, no. 23, p. 236104, 2004.

[74] S. Gabriele, S. Sclavons, G. Reiter, and P. Damman, "Disentanglement time of polymers determines the onset of rim instabilities in dewetting," *Physical Review Letters*, vol. 96, no. 15, p. 156105, 2006.

[75] N. Ferrell, A. Bross, and D. Hansford, "Micro/nanofabrication by spin dewetting on a poly(dimethyl siloxane) mold," *MRS Online Proceedings Library Archive*, vol. 1002, 2007.

[76] V. S. Mitlin and M. M. Sharma, "A local gradient theory for structural forces in thin fluid films," *Journal of Colloid and Interface Science*, vol. 157, no. 2, pp. 447–464, 1993.

[77] A. Sharma and A. T. Jameel, "Nonlinear stability, rupture, and morphological phase separation of thin fluid films on apolar and polar substrates," *Journal of Colloid and Interface Science*, vol. 161, no. 1, pp. 190–208, 1993.

[78] K. Jacobs, S. Herminghaus, and K. R. Mecke, "Thin liquid polymer films rupture via defects," *Langmuir*, vol. 14, no. 4, pp. 965–969, 1998.

[79] M. Sferrazza, M. Heppenstall-Butler, R. Cubitt, D. Bucknall, J. Webster, and R. A. L. Jones, "Interfacial instability driven by dispersive forces: The early stages of spinodal dewetting of a thin polymer film on a polymer substrate," *Physical Review Letters*, vol. 81, no. 23, p. 5173, 1998.

[80] A. Oron, "Three-dimensional nonlinear dynamics of thin liquid films," *Physical Review Letters*, vol. 85, no. 10, p. 2108, 2000.

[81] R. Konnur, K. Kargupta, and A. Sharma, "Instability and morphology of thin liquid films on chemically heterogeneous substrates," *Physical Review Letters*, vol. 84, no. 5, p. 931, 2000.

[82] K. Kargupta, R. Konnur, and A. Sharma, "Spontaneous dewetting and ordered patterns in evaporating thin liquid films on homogeneous and heterogeneous substrates," *Langmuir*, vol. 17, no. 4, pp. 1294–1305, 2001.

[83] D. Bandyopadhyay, R. Gulabani, and A. Sharma, "Instability and dynamics of thin liquid bilayers," *Industrial & Engineering Chemistry Research*, vol. 44, no. 5, pp. 1259–1272, 2005.

[84] R. D. Lenz and S. Kumar, "Competitive displacement of thin liquid films on chemically patterned substrates," *Journal of Fluid Mechanics*, vol. 571, pp. 33–57, 2007.

[85] Q. Pan, K. I. Winey, H. H. Hu, and R. J. Composto, "Unstable polymer bilayers. 2. the effect of film thickness," *Langmuir*, vol. 13, no. 6, pp. 1758–1766, 1997.

[86] G. Reiter, R. Khanna, and A. Sharma, "Self-destruction and dewetting of thin polymer films: The role of interfacial tensions," *Journal of Physics: Condensed Matter*, vol. 15, no. 1, p. S331, 2002.

[87] T. Ohzono, T. Nishikawa, and M. Shimomura, "One-step fabrication of polymer thin films with lithographic bas-relief micro-pattern and self-organized microporous structure," *Journal of Materials Science*, vol. 39, no. 6, pp. 2243–2247, 2004.

[88] R. Mukherjee, M. Gonuguntla, and A. Sharma, "Meso-patterning of thin polymer films by controlled dewetting: From nano-droplet arrays to membranes," *Journal of Nanoscience and Nanotechnology*, vol. 7, no. 6, pp. 2069–2075, 2007.

[89] A. Verma, A. Sharma, and G. U. Kulkarni, "Micropatterning: Ultrafast large-area micropattern generation in nonabsorbing polymer thin films by pulsed laser diffraction," *Small*, vol. 7, no. 6, pp. 757–757, 2011.

[90] A. Verma and A. Sharma, "Taming of self-organization in highly confined soft matter to sub-100 nm scales: Nanolens-arrays by spinodal instability of thin polymer films for high-resolution optical imaging," *Current Science*, pp. 1037–1045, 2013.

[91] A. Modi, S. M. Bhaway, B. D. Vogt, J. F. Douglas, A. Al-Enizi, A. Elzatahry, A. Sharma, and A. Karim, "Direct immersion annealing of thin block copolymer films," *ACS Applied Materials & Interfaces*, vol. 7, no. 39, pp. 21 639–21 645, 2015.

[92] N. Bhandaru, P. S. Goohpattader, D. Faruqui, R. Mukherjee, and A. Sharma, "Solvent-vapor-assisted dewetting of prepatterned thin polymer films: Control of morphology, order, and pattern miniaturization," *Langmuir*, vol. 31, no. 10, pp. 3203–3214, 2015.

[93] C. Redon, J. B. Brzoska, and F. Brochard-Wyart, "Dewetting and slippage of microscopic polymer films," *Macromolecules*, vol. 27, no. 2, pp. 468–471, 1994.

[94] C. J. Lawrence, "The mechanics of spin coating of polymer films," *The Physics of Fluids*, vol. 31, no. 10, pp. 2786–2795, 1988.

[95] S. H. Lee, P. J. Yoo, S. J. Kwon, and H. H. Lee, "Solvent-driven dewetting and rim instability," *The Journal of Chemical Physics*, vol. 121, no. 9, pp. 4346–4351, 2004.

[96] C. Tan, Z. Liu, W. Huang, and H. Zhang, "Non-volatile resistive memory devices based on solution-processed ultrathin two-dimensional nanomaterials," *Chemical Society Reviews*, vol. 44, no. 9, pp. 2615–2628, 2015.

[97] C. Clavero, "Plasmon-induced hot-electron generation at nanoparticle/metal-oxide interfaces for photovoltaic and photocatalytic devices," *Nature Photonics*, vol. 8, no. 2, pp. 95–103, 2014.

[98] N. R. Elezovic, V. R. Radmilovic, and N. V. Krstajic, "Platinum nanocatalysts on metal oxide based supports for low temperature fuel cell applications," *RSC Advances*, vol. 6, no. 8, pp. 6788–6801, 2016.

[99] S. Nishimoto and B. Bhushan, "Bioinspired self-cleaning surfaces with superhydrophobicity, superoleophobicity, and superhydrophilicity," *RSC Advances*, vol. 3, no. 3, pp. 671–690, 2013.

[100] N. Choudhary and D. Kaur, "Shape memory alloy thin films and heterostructures for mems applications: A review," *Sensors and Actuators A: Physical*, vol. 242, pp. 162–181, 2016.

[101] B. Janjua, H. Sun, C. Zhao, D. H. Anjum, F. Wu, A. A. Alhamoud, X. Li, A. M. Albadri, A. Y. Alyamani, and M. M. El-Desouki, "Self-planarized quantum-disks-in-nanowires ultraviolet-b emitters utilizing pendeo-epitaxy," *Nanoscale*, 2017.

[102] S. Dutta, N. Mandal, and D. Bandyopadhyay, "Paper-based α-amylase detector for point-of-care diagnostics," *Biosensors and Bioelectronics*, vol. 78, pp. 447–453, 2016.

[103] A. Eatemadi, H. Daraee, N. Zarghami, H. Melat Yar, and A. Akbarzadeh, "Nanofiber: Synthesis and biomedical applications," *Artificial Cells, Nanomedicine, and Biotechnology*, vol. 44, no. 1, pp. 111–121, 2016.

[104] M. Gonidec, M. M. Hamedi, A. Nemiroski, L. M. Rubio, C. Torres, and G. M. Whitesides, "Fabrication of nonperiodic metasurfaces by microlens projection lithography," *Nano Letters*, vol. 16, no. 7, pp. 4125–4132, 2016.

[105] S. A. Ruiz and C. S. Chen, "Microcontact printing: A tool to pattern," *Soft Matter*, vol. 3, no. 2, pp. 168–177, 2007.

[106] M. Singh, H. M. Haverinen, P. Dhagat, and G. E. Jabbour, "Inkjet printing-process and its applications," *Advanced Materials*, vol. 22, no. 6, pp. 673–685, 2010.

[107] A. Revzin, R. J. Russell, V. K. Yadavalli, W.-G. Koh, C. Deister, D. D. Hile, M. B. Mellott, and M. V. Pishko, "Fabrication of poly(ethylene glycol) hydrogel microstructures using photolithography," *Langmuir*, vol. 17, no. 18, pp. 5440–5447, 2001.

[108] F. Wang, P. Li, D. Wang, L. Li, S. Xie, L. Liu, Y. Wang, and W. J. Li, "Mechanically modulated dewetting by atomic force microscope for micro-and nano-droplet array fabrication," *Scientific Reports*, vol. 4, p. 6524, 2014.

[109] A. Verma and A. Sharma, "Sub-40 nm polymer dot arrays by self-organized dewetting of electron beam treated ultrathin polymer films," *RSC Advances*, vol. 2, no. 6, pp. 2247–2249, 2012.

[110] H. Schift, "Nanoimprint lithography: 2d or not 2d? a review," *Applied Physics A*, vol. 121, no. 2, pp. 415–435, 2015.

[111] Z. Zhang, F. Dong, T. Cheng, K. Qiu, Q. Zhang, W. Chu, and X. Wu, "Nanofabricated pixelated micropolarizer array for visible imaging polarimetry," *Review of Scientific Instruments*, vol. 85, no. 10, p. 105002, 2014.

[112] S. F. Oliveira, G. Bisker, N. A. Bakh, S. L. Gibbs, M. P. Landry, and M. S. Strano, "Protein functionalized carbon nanomaterials for biomedical applications," *Carbon*, vol. 95, pp. 767–779, 2015.

[113] T. P. Burg, M. Godin, S. M. Knudsen, W. Shen, G. Carlson, J. S. Foster, K. Babcock, and S. R. Manalis, "Weighing of biomolecules, single cells and single nanoparticles in fluid," *Nature*, vol. 446, no. 7139, pp. 1066–1069, 2007.

[114] T. Nakanishi, Y. Hirai, H. Yabu, and M. Shimomura, "Flexible, optically transparent, and conductive line-and-space-patterned films prepared by using a simple dewetting process of gold nanoparticle dispersions," *Applied Physics Express*, vol. 4, no. 11, p. 117301, 2011.

[115] A. Lal Das, R. Mukherjee, V. Katiyer, M. Kulkarni, A. Ghatak, and A. Sharma, "Generation of sub-micrometer-scale patterns by successive miniaturization using hydrogels," *Advanced Materials*, vol. 19, no. 15, pp. 1943–1946, 2007.

[116] P. G. de Gennes and J. Prost, "The physics of liquid crystals," 1993.

[117] P. Raynes, "Liquid crystals - 2nd edition, by s chandrasekhar, cambridge university press," *Liquid Crystals Today*, vol. 3, no. 3, 1993.

[118] D. Gentili, G. Foschi, F. Valle, M. Cavallini, and F. Biscarini, "Applications of dewetting in micro and nanotechnology," *Chemical Society Reviews*, vol. 41, no. 12, pp. 4430–4443, 2012.

[119] M. P. Valignat, S. Villette, J. Li, R. Barberi, R. Bartolino, E. Dubois-Violette, and A. M. Cazabat, "Wetting and anchoring of a nematic liquid crystal on a rough surface," *Physical Review Letters*, vol. 77, no. 10, p. 1994, 1996.

[120] S. K. Ghosh, "A model for the orientational order in liquid crystals," *II Nuovo Cimento D*, vol. 4, no. 3, pp. 229–244, 1984.

[121] D. van Effenterre, R. Ober, M. P. Valignat, and A. M. Cazabat, "Binary separation in very thin nematic films: Thickness and phase coexistence," *Physical Review Letters*, vol. 87, no. 12, p. 125701, 2001.

[122] E. I. Rjumtse, M. A. Osipov, T. A. Rotinyan, and N. P. Yevlampieva, "Electric field effect on the nematic-isotropic phase transition," *Liquid Crystals*, vol. 18, no. 1, pp. 87–95, 1995.

[123] T. Ostapenko, D. B. Wiant, S. N. Sprunt, A. Jákli, and J. T. Gleeson, "Magnetic-field induced isotropic to nematic liquid crystal phase transition," *Physical Review Letters*, vol. 101, no. 24, p. 247801, 2008.

[124] S. G. Hahm, Y.-G. Ko, Y. Rho, B. Ahn, and M. Ree, "Liquid crystal alignment in advanced flat-panel liquid crystal displays," *Current Opinion in Chemical Engineering*, vol. 2, no. 1, pp. 71–78, 2013.

[125] R. MacKenzie and A. J. Asbury, "Clinical evaluation of liquid crystal skin thermometers," *British Journal of Anaesthesia*, vol. 72, no. 2, pp. 246–249, 1994.

[126] S. Relaix, C. Bourgerette, and M. Mitov, "Broadband reflective liquid crystalline gels due to the ultraviolet light screening made by the liquid crystal," *Applied Physics Letters*, vol. 89, no. 25, p. 251907, 2006.

[127] H. R. Morris, C. C. Hoyt, and P. J. Treado, "Imaging spectrometers for fluorescence and raman microscopy: Acousto-optic and liquid crystal tunable filters," *Applied Spectroscopy*, vol. 48, no. 7, pp. 857–866, 1994.

[128] A. Agrawal, A. C. Chipara, Y. Shamoo, P. K. Patra, B. J. Carey, P. M. Ajayan, W. G. Chapman, and R. Verduzco, "Dynamic self-stiffening in liquid crystal elastomers," *Nature Communications*, vol. 4, p. 1739, 2013.

[129] P. Deo, D. Mirshekar-Syahkal, L. Seddon, S. E. Day, and F. A. Fernández, "Microstrip device for broadband (15–65 ghz) measurement of dielectric properties of nematic liquid crystals," *IEEE Transactions on Microwave Theory and Techniques*, vol. 63, no. 4, pp. 1388–1398, 2015.

[130] K. Sun, Z. Xiao, S. Lu, W. Zajaczkowski, W. Pisula, E. Hanssen, J. M. White, R. M. Williamson, J. Subbiah, and J. Ouyang, "A molecular nematic liquid crystalline material for high-performance organic photovoltaics," *Nature Communications*, vol. 6, 2015.

[131] S. J. Woltman, G. D. Jay, and G. P. Crawford, "Liquid-crystal materials find a new order in biomedical applications," *Nature Materials*, vol. 6, no. 12, pp. 929–938, 2007.

[132] S. Sergeyev, W. Pisula, and Y. H. Geerts, "Discotic liquid crystals: A new generation of organic semiconductors," *Chemical Society Reviews*, vol. 36, no. 12, pp. 1902–1929, 2007.

[133] G. W. Gray, *Thermotropic Liquid Crystals*. John Wiley & Sons Inc, 1987.

[134] H. Coles, D. Demus, J. Goodby, G. Gray, H.-W. Spiess, and V. Vill, "Chiral nematic liquid crystals: Chiral nematics: Physical properties and applications," *Handbook of Liquid Crystals: Low Molecular Weight Liquid Crystals I, Volume 2 A*, pp. 335–409, 1998.

[135] S. H. Ryu and D. K. Yoon, "Liquid crystal phases in confined geometries," *Liquid Crystals*, vol. 43, no. 13-15, pp. 1951–1972, 2016.

[136] H. Seki, Y. Masuda, Y. Itoh, and T. Uchida, "Tilted homeotropic alignment of liquid-crystal molecules using the rubbing method," *Molecular Crystals and Liquid Crystals*, vol. 199, no. 1, pp. 151–158, 1991.

[137] S. Faetti, M. Gatti, V. Palleschi, and T. J. Sluckin, "Almost critical behavior of the anchoring energy at the interface between a nematic liquid crystal and a sio substrate," *Physical Review Letters*, vol. 55, no. 16, p. 1681, 1985.

[138] T. Uchida, M. Ohgawara, and M. Wada, "Liquid crystal orientation on the surface of obliquely-evaporated silicon monoxide with homeotropic surface treatment," *Japanese Journal of Applied Physics*, vol. 19, no. 11, p. 2127, 1980.

[139] G. P. Crawford, R. J. Ondris-Crawford, J. W. Doane, and S. Žumer, "Systematic study of orientational wetting and anchoring at a liquid-crystal-surfactant interface," *Physical Review E*, vol. 53, no. 4, p. 3647, 1996.

[140] R. Pratibha, S. I. Torgova, N. V. Madhusudana, and A. Strigazzi, "Alignment transition driven by adsorption in a nematic liquid crystal forming h-bonds," *Physics Letters A*, vol. 239, no. 1, pp. 115–120, 1998.

[141] J. E. Proust, L. Ter-Minassian-Saraga, and E. Guyon, "Orientation of a nematic liquid crystal by suitable boundary surfaces," *Solid State Communications*, vol. 11, no. 9, pp. 1227–1230, 1972.

[142] R. Barberi and G. Durand, "Order parameter of a nematic liquid crystal on a rough surface," *Physical Review A*, vol. 41, no. 4, p. 2207, 1990.

[143] G. P. Crawford, R. Stannarius, and J. W. Doane, "Surface-induced orientational order in the isotropic phase of a liquid-crystal material," *Physical Review A*, vol. 44, no. 4, p. 2558, 1991.

[144] V. Mocella, C. Ferrero, M. Iovane, and R. Barberi, "Numerical investigation of surface distortion and order parameter variation in nematics," *Liquid Crystals*, vol. 26, no. 9, pp. 1345–1350, 1999.

[145] F. Vandenbrouck, S. Bardon, M. P. Valignat, and A. M. Cazabat, "Wetting transition and divergence of the extrapolation length near the nematic-isotropic transition," *Physical Review Letters*, vol. 81, no. 3, p. 610, 1998.

[146] C. Poulard and A. M. Cazabat, "Spontaneous spreading of nematic liquid crystals," *Langmuir*, vol. 21, no. 14, pp. 6270–6276, 2005.

[147] F. Vandenbrouck, M. P. Valignat, and A. M. Cazabat, "Thin nematic films: Metastability and spinodal dewetting," *Physical Review Letters*, vol. 82, no. 13, p. 2693, 1999.

[148] A. J. Leadbetter, R. M. Richardson, and C. N. Colling, "The structure of a number of nematogens," *Le Journal de Physique Colloques*, vol. 36, no. C1, pp. C1–37, 1975.

[149] H. Kasten and G. Strobl, "Nematic wetting at the free surface of 4-cyano-4-n-alkylbiphenyls," *The Journal of Chemical Physics*, vol. 103, no. 15, pp. 6768–6774, 1995.

[150] A. M. Cazabat, U. Delabre, C. Richard, and Y. Y. C. Sang, "Experimental study of hybrid nematic wetting films," *Advances in Colloid and Interface Science*, vol. 168, no. 1, pp. 29–39, 2011.

[151] P. Sheng, "Phase transition in surface-aligned nematic films," *Physical Review Letters*, vol. 37, no. 16, p. 1059, 1976.

[152] A. Golemme, S. Zumer, D. W. Allender, and J. W. Doane, "Continuous nematic-isotropic transition in submicron-size liquid-crystal droplets," *Physical Review Letters*, vol. 61, no. 26, p. 2937, 1988.

[153] P. Ziherl, R. Podgornik, and S. Žumer, "Casimir force in liquid crystals close to the nematic–isotropic phase transition," *Chemical Physics Letters*, vol. 295, no. 1, pp. 99–104, 1998.

[154] P. Ziherl, R. Podgornik, and S. Žumer, "Pseudo-casimir structural force drives spinodal dewetting in nematic liquid crystals," *Physical Review Letters*, vol. 84, no. 6, p. 1228, 2000.

[155] D. van Effenterre, M. P. Valignat, and D. Roux, "Coupling between the nematic/isotropic transition and a thickness transition: A theoretical approach," *Europhysics Letters*, vol. 62, no. 4, p. 526, 2003.

[156] P. Ziherl and S. Žumer, "Morphology and structure of thin liquid-crystalline films at nematic-isotropic transition," *The European Physical Journal E: Soft Matter and Biological Physics*, vol. 12, no. 3, pp. 361–365, 2003.

[157] H. Yokoyama, "Nematic–isotropic transition in bounded thin films," *Journal of the Chemical Society, Faraday Transactions 2: Molecular and Chemical Physics*, vol. 84, no. 8, pp. 1023–1040, 1988.

[158] M. M. Wittebrood, D. H. Luijendijk, S. Stallinga, T. Rasing, and I. Muševič, "Thickness-dependent phase transition in thin nematic films," *Physical Review E*, vol. 54, no. 5, p. 5232, 1996.

[159] S. Herminghaus, K. Jacobs, K. Mecke, J. Bischof, A. Fery, M. Ibn-Elhaj, and S. Schlagowski, "Spinodal dewetting in liquid crystal and liquid metal films," *Science*, vol. 282, no. 5390, pp. 916–919, 1998.

[160] S. Schlagowski, K. Jacobs, and S. Herminghaus, "Nucleation-induced undulative instability in thin films of ncb liquid crystals," *Europhysics Letters*, vol. 57, no. 4, p. 519, 2002.

[161] G. Barbero, P. Jägemalm, and A. K. Zvezdin, "Temperature-induced surface transition in nematic liquid crystals oriented by evaporated siox," *Physical Review E*, vol. 64, no. 2, p. 021703, 2001.

[162] D. van Effenterre and M. P. Valignat, "Stability of thin nematic films," *The European Physical Journal E*, vol. 12, no. 3, pp. 367–372, 2003.

[163] S. Sankararaman and S. Ramaswamy, "Instabilities and waves in thin films of living fluids," *Physical Review Letters*, vol. 102, no. 11, p. 118107, 2009.

[164] A. Ajdari, L. Peliti, and J. Prost, "Fluctuation-induced long-range forces in liquid crystals," *Physical Review Letters*, vol. 66, no. 11, p. 1481, 1991.

[165] F. Merola, S. Grilli, S. Coppola, V. Vespini, S. De Nicola, P. Maddalena, C. Carfagna, and P. Ferraro, "Reversible fragmentation and self-assembling of nematic liquid crystal droplets on functionalized pyroelectric substrates," *Advanced Functional Materials*, vol. 22, no. 15, pp. 3267–3272, 2012.

[166] M. Humar, M. Ravnik, S. Pajk, and I. Muševič, "Electrically tunable liquid crystal optical microresonators," *Nature Photonics*, vol. 3, no. 10, pp. 595–600, 2009.

[167] E. Nagali, L. Sansoni, F. Sciarrino, F. De Martini, L. Marrucci, B. Piccirillo, E. Karimi, and E. Santamato, "Optimal quantum cloning of orbital angular momentum photon qubits through hong–ou–mandel coalescence," *Nature Photonics*, vol. 3, no. 12, pp. 720–723, 2009.

[168] H. Zhang, P. Guo, P. Chen, S. Chang, and J. Yuan, "Liquid-crystal-filled photonic crystal for terahertz switch and filter," *Journal of the Optical Society of America B-Optical Physics*, vol. 26, no. 1, pp. 101–106, 2009.

[169] H. Li, X.-Y. Zhang, T.-X. Zhang, and X.-B. Sheb, "Optical imaging characteristics of a new liquid crystal lens," *Journal of Infrared and Millimeter Waves*, vol. 6, p. 007, 2009.

[170] M. Gonuguntla, A. Sharma, R. Mukherjee, and S. A. Subramanian, "Control of self-organized contact instability and patterning in soft elastic films," *Langmuir*, vol. 22, no. 16, pp. 7066–7071, 2006.

[171] K. Efimenko, W. E. Wallace, and J. Genzer, "Surface modification of sylgard-184 poly(dimethyl siloxane) networks by ultraviolet and ultraviolet/ozone treatment," *Journal of Colloid and Interface Science*, vol. 254, no. 2, pp. 306–315, 2002.

[172] Z. Zhang and Y. Wu, "Nabh4-induced assembly of immobilized au nanoparticles into chainlike structures on a chemically modified glass surface," *Langmuir*, vol. 27, no. 16, pp. 9834–9842, 2011.

[173] N. B. Trung, H. Yoshikawa, E. Tamiya, P. H. Viet, Y. Takamura, and T. Ashahi, "Propitious immobilization of gold nanoparticles on poly(dimethyl siloxane) substrate for local surface plasmon resonance based biosensor," *Japanese Journal of Applied Physics*, vol. 51, no. 3R, p. 037001, 2012.

[174] M. N. Martin, J. I. Basham, P. Chando, and S.-K. Eah, "Charged gold nanoparticles in non-polar solvents: 10-min synthesis and 2d self-assembly," *Langmuir*, vol. 26, no. 10, pp. 7410–7417, 2010.

[175] L. Brusch, H. Kühne, U. Thiele, and M. Bär, "Dewetting of thin films on heterogeneous substrates: Pinning versus coarsening," *Physical Review E*, vol. 66, no. 1, p. 011602, 2002.

[176] Z. Ban, Y. A. Barnakov, F. Li, V. O. Golub, and C. J. O'Connor, "The synthesis of core–shell iron@gold nanoparticles and their characterization," *Journal of Materials Chemistry*, vol. 15, no. 43, pp. 4660–4662, 2005.

[177] M. Ruths and B. Zappone, "Direct nanomechanical measurement of an anchoring transition in a nematic liquid crystal subject to hybrid anchoring conditions," *Langmuir*, vol. 28, no. 22, pp. 8371–8383, 2012.

[178] S. Javadian, N. Dalir, A. G. Gilani, J. Kakemam, and A. Yousefi, "A new approach to study interaction parameters in cyanobiphenyl liquid crystal binary systems," *The Journal of Chemical Thermodynamics*, vol. 80, pp. 22–29, 2015.

[179] U. Delabre, C. Richard, and A. M. Cazabat, "Some specificities of wetting by cyanobiphenyl liquid crystals," *Journal of Physics: Condensed Matter*, vol. 21, no. 46, p. 464129, 2009.

[180] R. Mukherjee, A. Sharma, M. Gonuguntla, and G. K. Patil, "Adhesive force assisted imprinting of soft solid polymer films by flexible foils," *Journal of Nanoscience and Nanotechnology*, vol. 8, no. 7, pp. 3406–3415, 2008.

[181] K. Y. Suh, Y. S. Kim, and H. H. Lee, "Capillary force lithography," *Advanced Materials*, vol. 13, no. 18, pp. 1386–1389, 2001.

[182] N. Herzer, M. M. Wienk, P. Schmit, A. B. Spoelstra, C. E. Hendriks, S. D. Oosterhout, S. Hoeppener, and U. S. Schubert, "Fabrication of pedot–ots-patterned ito substrates," *Journal of Materials Chemistry*, vol. 20, no. 32, pp. 6618–6621, 2010.

[183] M. Brust, M. Walker, D. Bethell, D. J. Schiffrin, and R. Whyman, "Synthesis of thiol-derivatised gold nanoparticles in a two-phase liquid–liquid system," *Journal of the Chemical Society, Chemical Communications*, no. 7, pp. 801–802, 1994.

[184] M. J. Stephen and J. P. Straley, "Physics of liquid crystals," *Reviews of Modern Physics*, vol. 46, no. 4, p. 617, 1974.

[185] A. Saupe, "Textures, deformations, and structural order of liquid crystals," *Journal of Colloid and Interface Science*, vol. 58, no. 3, pp. 549–558, 1977.

[186] P. Sheng, "Boundary-layer phase transition in nematic liquid crystals," *Physical Review A*, vol. 26, no. 3, p. 1610, 1982.

[187] E. F. Gramsbergen, L. Longa, and W. H. de Jeu, "Landau theory of the nematic-isotropic phase transition," *Physics Reports*, vol. 135, no. 4, pp. 195–257, 1986.

[188] E. I. Kats and T. V. Abalyan, "Ordering and phase transitions in liquid crystals," *Phase Transitions: A Multinational Journal*, vol. 29, no. 4, pp. 237–268, 1991.

[189] A. J. Jin, M. Veum, C. F. Chou, J. T. Ho, V. Surendranath, T. Stoebe, S. W. Hui, and C. C. Huang, "Characterization several novel phase transitions in a unique lower dimension system of free-standing liquid-crystal films," *Modern Physics Letters B*, vol. 10, no. 07, pp. 269–277, 1996.

[190] J. B. Fournier and P. Galatola, "Coarse-grained surface energies and temperature-induced anchoring transitions in nematic liquid crystals," *Physical Review Letters*, vol. 82, no. 24, p. 4859, 1999.

[191] A. Lebar, G. Cordoyiannis, Z. Kutnjak, and B. Zalar, *The Isotropic-to-Nematic Conversion in Liquid Crystalline Elastomers*. Springer, 2010.

[192] S. Singh, H. Singh, T. Karthick, P. Tandon, and V. Prasad, "Phase transition analysis of v-shaped liquid crystal: Combined temperature-dependent ftir and density functional theory approach," *Spectrochimica Acta Part A: Molecular Spectroscopy*, vol. 188, pp. 561–570, 2018.

[193] S. Kim, P. A. Thiessen, E. E. Bolton, J. Chen, G. Fu, A. Gindulyte, L. Han, J. He, S. He, and B. A. Shoemaker, "Pubchem substance and compound databases," *Nucleic Acids Research*, vol. 44, no. D1, pp. D1202–D1213, 2015.

[194] B. Ravi, R. Mukherjee, and D. Bandyopadhyay, "Solvent vapour mediated spontaneous healing of self-organized defects of liquid crystal films," *Soft Matter*, vol. 11, no. 1, pp. 139–146, 2015.

[195] *4-n-pentyl-4′-cyanobiphenyl*, (accessed September 21, 2016), http ://www.sigmaaldrich.com /catalog/product/aldrich/328510?lang=en&region=IN.

[196] P. K. Rai, M. M. Denn, and C. Maldarelli, "Interfacial tension of liquid crystalline droplets," *Langmuir*, vol. 19, no. 18, pp. 7370–7373, 2003.

[197] S. Xu, H. Ren, and S.-T. Wu, "Dielectrophoretically tunable optofluidic devices," *Journal of Physics D: Applied Physics*, vol. 46, no. 48, p. 483001, 2013.

[198] A. Oron, S. H. Davis, and S. G. Bankoff, "Long-scale evolution of thin liquid films," *Reviews of Modern Physics*, vol. 69, no. 3, p. 931, 1997.

[199] S. M. Troian, X. L. Wu, and S. A. Safran, "Fingering instability in thin wetting films," *Physical Review Letters*, vol. 62, no. 13, p. 1496, 1989.

[200] R. L. Speth and E. Lauga, "Capillary instability on a hydrophilic stripe," *New Journal of Physics*, vol. 11, no. 7, p. 075024, 2009.

[201] L. W. Schwartz, R. V. Roy, R. R. Eley, and S. Petrash, "Dewetting patterns in a drying liquid film," *Journal of Colloid and Interface Science*, vol. 234, no. 2, pp. 363–374, 2001.

[202] D. P. Birnie III, "A model for drying control cosolvent selection for spin-coating uniformity: The thin film limit," *Langmuir*, vol. 29, no. 29, pp. 9072–9078, 2013.

[203] B. Ravi, S. Chakraborty, M. Bhattacharjee, S. Mitra, A. Ghosh, P. S. Gooh Pattader, and D. Bandyopadhyay, "Pattern-directed ordering of spin-dewetted liquid crystal micro-or nanodroplets as pixelated light reflectors and locomotives," *ACS Applied Materials & Interfaces*, vol. 9, no. 1, pp. 1066–1076, 2016.

[204] A. S. Padmakar, K. Kargupta, and A. Sharma, "Instability and dewetting of evaporating thin water films on partially and completely wettable substrates," *The Journal of Chemical Physics*, vol. 110, no. 3, pp. 1735–1744, 1999.

[205] A. Sharma, "Equilibrium and dynamics of evaporating or condensing thin fluid domains: Thin film stability and heterogeneous nucleation," *Langmuir*, vol. 14, no. 17, pp. 4915–4928, 1998.

[206] J. A. Schonberg, S. DasGupta, and P. C. Wayner, "An augmented young-laplace model of an evaporating meniscus in a microchannel with high heat flux," *Experimental Thermal and Fluid Science*, vol. 10, no. 2, pp. 163–170, 1995.

[207] S. DasGupta, J. A. Schonberg, and P. C. Wayner, "Investigation of an evaporating extended meniscus based on the augmented young-laplace equation," *Transactions-American Society of Mechanical Engineers Journal of Heat Transfer*, vol. 115, pp. 201–201, 1993.

[208] J. N. Lee, C. Park, and G. M. Whitesides, "Solvent compatibility of poly(dimethyl siloxane)-based microfluidic devices," *Analytical Chemistry*, vol. 75, no. 23, pp. 6544–6554, 2003.

[209] Z. Zhang, V. P. Panov, M. Nagaraj, R. J. Mandle, J. W. Goodby, G. R. Luckhurst, J. C. Jones, and H. F. Gleeson, "Raman scattering studies of order parameters in liquid crystalline dimers exhibiting the nematic and twist-bend nematic phases," *Journal of Materials Chemistry C*, vol. 3, no. 38, pp. 10 007–10 016, 2015.

[210] S.-K. Fan and F.-M. Wang, "Multiphase optofluidics on an electro-microfluidic platform powered by electrowetting and dielectrophoresis," *Lab on a Chip*, vol. 14, no. 15, pp. 2728–2738, 2014.

[211] S. M. Troian, E. Herbolzheimer, and S. A. Safran, "Model for the fingering instability of spreading surfactant drops," *Physical Review Letters*, vol. 65, no. 3, p. 333, 1990.

List of Publications

National and International Conferences

- Abhijna, D.; **Ravi, B.**; Amit, K. S.; Bandyopadhyay, D. Effect of Gold Nanoparticles on the Self-Organization of Ultrathin Polymer Film. *ICANN*, **2013**, IIT Guwahati. (**Best Poster Award**)
- **Ravi, B.**; Bandyopadhyay, D. Self-organized Hierarchical Submicron Liquid Crystal Droplets by Solvent Induced Meniscus Dewetting. *ICANN*, **2015**, IIT Guwahati.
- **Ravi, B.**; Bandyopadhyay, D. Liquid crystal vapour sensor for aromatic and non-aromatic compounds. *CHEMCON*, **2015**, IIT Guwahati.

International Journals

- Mamidi, N.; Gorai, S.; **Ravi, B.**; Manna, D. Physicochemical Characterization of Diacyltetrol-based Lipids Consisting of both Diacylglycerol and Phospholipid Headgroups. *RSC Adv.* **2014**, *4*, 21971–21978.
- **Ravi, B.**; Mukherjee, R.; Bandyopadhyay, D. Solvent Vapour Mediated Spontaneous Healing of Self-Organized Defects of Liquid Crystal Films. *Soft Matter* 2015, *11*, 139–146.
- **Ravi, B.**; Chakraborty, S.; Bhattacharjee, M.; Mitra, S.; Ghosh, A.; Gooh Pattader, P. S.; Bandyopadhyay, D. Pattern-Directed Ordering of Spin-Dewetted Liquid Crystal Micro- or Nanodroplets as Pixelated Light Reflectors and Locomotives. *ACS Appl. Mater. Interf.* 2017, *9*, 1066–1076.

Manuscript Submitted

- **Ravi, B.**; Bhattacharjee, M.; Ghosh, A.; Bandyopadhyay, D. Fabrication of Liquid Crystal Nanolenses Employing the Contact Line Instabilities of Evaporating Films.

- **Ravi, B.**; Chakraborty, S.; Bhandaru, N.; Mukherjee, R.; Gooh Pattader, P. S.; Bandyopadhyay, D. Pattern Directed Phase Transition and Dewetting of the Nematic and Smectic Liquid Crystal Films for Detection of Chemical Vapour Compounds.

Manuscript Under Preparation

- Das, A.; **Ravi. B.**; Singh, K. A.; Bandyopadhyay, D. Physicochemical Pattern Induced Dewetting of Ultrathin Polymer Film to Form Dense and Ordered Nanostructures.

Appendix A

5CB Contact Angle

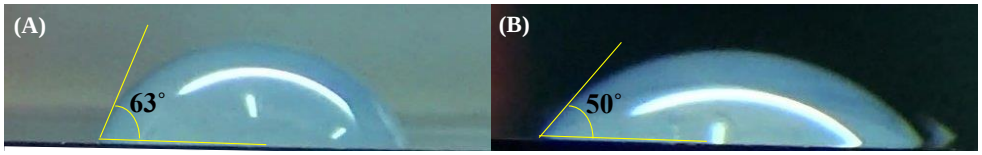

Hydrophobic PDMS **Hydrophilic PDMS**

Figure A.1: Images (A) and (B) show equilibrium contact angle of 5CB liquid crystal on lyophobic and lyophilic PDMS substrates, respectively.

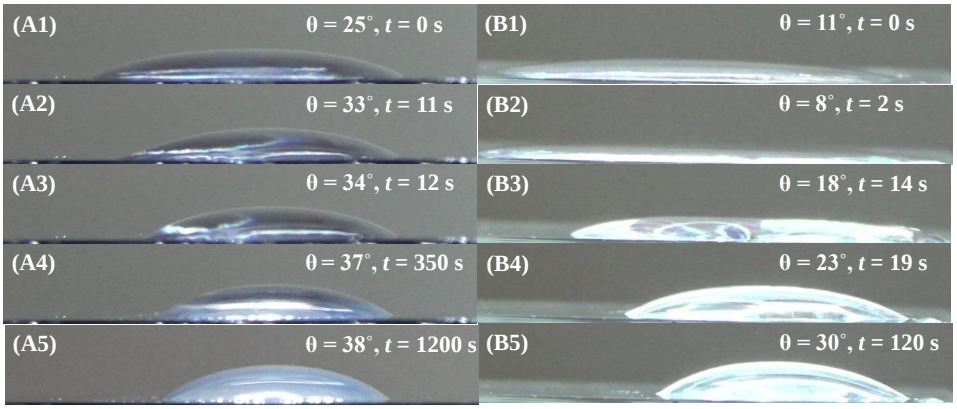

Hydrophobic PDMS **Hydrophilic PDMS**

Figure A.2: Images (A) and (B) show dynamic contact angle of 90% (w/v) 5CB liquid crystal in hexane solvent on lyophobic and lyophilic PDMS substrates, respectively.